**UNIVERSITÀ DEGLI STUDI DI PADOVA**

Sede Amministrativa: Università degli Studi di Padova
Dipartimento di Ingegneria dell'Informazione

SCUOLA DI DOTTORATO DI RICERCA IN INGEGNERIA DELL'INFORMAZIONE
INDIRIZZO: INGENERIA ELETTRONICA E DELLE TELECOMUNICAZIONI
CICLO XXI

# Analysis of the Temperature impact on Reliability of GaN-based Light Emitting Diodes

**Coordinatore:** Ch.mo Prof. Matteo Bertocco
**Supervisore:** Ch.mo Prof. Enrico Zanoni

**Dottorando:** Lorenzo-Roberto Trevisanello

12 gennaio 2008

# Abstract

This thesis reports the results of the three-year research activity on Light Emitting Diodes (LEDs) for Solid State Lighting. In particular, the research project was focused on the study of thermal characterization of Gallium Nitride (GaN) based LEDs, and the impact of the temperature on the reliability of devices.

The work starts from an overview of the State of the art of III-V optoelectronic devices and on reliability aspects of such devices. Afterwards, different characterization methods for thermal characterization of LEDs are presented and discussed with the description of some experimental implementations designed. In the remaining chapters three reliability approaches on different LED structures are presented: (i) an Accelerated Lifetime Testing (ALT) on low-flux Phosphors Converted LEDs, (ii) an ALT on High Brightness LEDs with Chip-on-Board technology, and (iii) a reliability analysis on Deep UV AlGaN-LEDs. In all case studies, the thermal aspects have been stressed in the analysis of the results.

The different activities started from an in-depth knowledge of the device structure and the related issues, and aimed at (i) extrapolating the degradation model that can provide an accurate lifetime estimation, (ii) investigating on physical mechanisms responsible for degradation, (iii) finding a correlation between thermal behaviour and reliability.

The present work permitted to collect new results concerning the mechanisms that still limit the reliability of LEDs, and will provide the experimental and analytical tools suitable for ALT design and implementation.

# Sommario

Con il presente lavoro di tesi vengono riportati i risultati dell'attività di ricerca triennale su Light Emitting Diode (LED) per illuminazione allo stato solido. In particolare, il progetto di ricerca è stato incentrato sullo studio della caratterizzazione termica di LED in nitruro di gallio (GaN) e sull'impatto della temperatura sull'affidabilità dei dispositivi.

Il lavoro comincia da una panoramica sullo stato dell'arte di dispositivi optoelettronici a semiconduttore composito di tipo III-V e sugli aspetti affidabilistici ad essi legati. In seguito vengono presentati diversi metodi per la caratterizzazione termica dei LED, insieme alla descrizione dettagliata delle diverse implementazioni sperimentali per ottenere tali misure. Nei capitoli restanti vengono presentati e discussi tre diversi approcci di analisi affidabilistica: (i) un test di vita accelerato su LED bianchi a basso flusso luminoso, (ii) un test di vita accelerato su LED ad alto flusso con tecnologia Chip On Board, e (iii) un'analisi affidabilistica di LED in AlGaN con emissione nel profondo ultravioletto. In tutti questi studi, sono stati sottolineati gli aspetti termici nell'analisi dei risultati.

Queste analisi partono da un'approfondita conoscenza della struttura dei dispositivi e delle problematiche relative, con l'obiettivo di (i) trovare un modello di degrado in grado di fornire una corretta stima del tempo di vita, (ii) indagare i meccanismi fisici alla base del degrado, e (iii) individuate una correlazione tra le proprietà termiche e l'affidabilità del dispositivo.

Il lavoro presentato ha permesso di mettere insieme nuovi risultati relativi ai meccanismi che attualmente limitano l'affidabilità dei LED, e ha reso disponibile diversi strumenti sperimentali e analitici utili per la progettazione e l'implementazione di test di vita accelerati futuri.

*”Sebbene tu ricercatore sia in erba*
*Inverti il segno, e gliela fai in barba“*

*Lorenzo Rigutti*

# Contents

# Acronyms

| | |
|---|---|
| ALT | Accelerated Life Testing |
| CCT | Correlated Color Temperature |
| CDF | Cumulative Distribution Function |
| COB | Chip-On-Board |
| CRI | Color Rendering Index |
| DUV | Deep Ultra-Violet |
| EL | Electro Luminescence |
| FEA | Finite Element Analysis |
| FEM | Finite Element Method |
| HB-LED | High Brightness LED |
| PC-LED | Phosphors Converted LED |
| LED | Light Emitting Diode |
| MQW | Multi Quantum Well |
| MTTF | Mean Time To Failure |
| SSL | Solid State Lighting |
| TEC | Thermo-Electric Cooler |
| TIP | Truncated Inverted Pyramid |
| TIR | Total Internal Reflections |

# Chapter 1

# Introduction

## 1.1 Background

In the last years, the development of GaN-based optoelectronic devices covering a wide spectral region from green to ultra-violet has determined a revolution in the lighting industry: thanks to the introduction of high performance device structures (efficiency above 130 lm/W, [1]), the GaN LED technology is targeted to replace ordinary white light bulbs for general lighting, with enormous energy savings and environmental benefits (see Fig. 1.1 for a comparison between the efficiency of LEDs and other light sources).

The environmental advantages of adopting LEDs for general illumination can be easily understood: assuming 100% market penetration of LED lighting and a 50% conversion efficiency, in the year 2025 the projected electric savings in the U.S. would be roughly 525 TW-h/year (or 35 B$/year), and the savings in carbon dioxide equivalent emissions would be approximately 87 Mtons.

Furthermore, LED illumination technology eliminates the hazardous-waste issues associated with mercury-containing light fluorescent tubes. For this reason, GaN-based LED market is expected to see a rapid growth in the next three years, due to the possibility of adopting these devices for the realization of high-efficiency light sources.

Despite the excellent properties of GaN-based optoelectronic devices, there is still a set of critical issues that must be addressed before efficient and reliable illumination systems based on LEDs can be realized. Roughly speaking, mass application of solid-state lighting is limited by various factors, such as:

- Cost of the LED chips
- Cost of ownership (efficiency, lumen per watt of electric power, lifetime, etc.)
- Quality of white light
- Cost, efficiency and effectiveness of control circuit; ease of connection to the AC power grid.

More quantitatively, the research gaps that slow down the adoption of power LEDs concern all the levels of technology development, i.e. (i) material and technology growth and characterization of GaN LEDs, (ii) performance and reliability optimization of the devices, (iii)

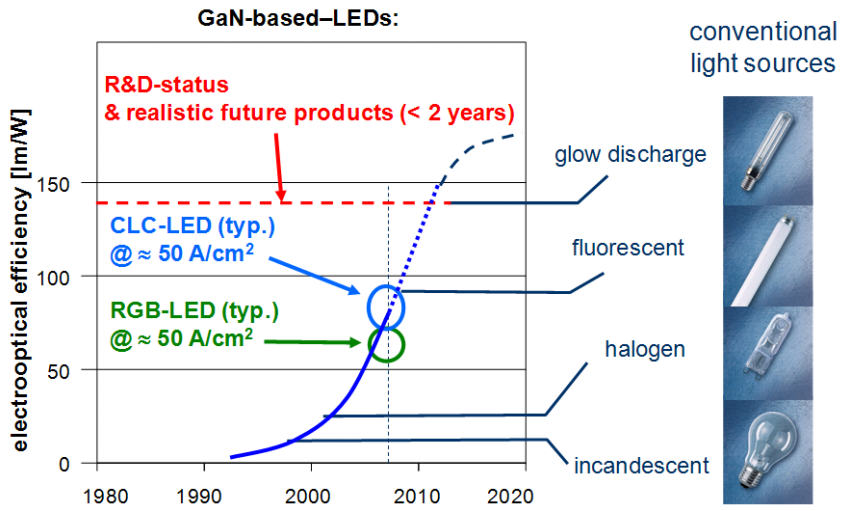


*Figure 1.1: GaN-based LEDs have already reached Electro-Optical efficiencies (lm/W) greater than incandescent, halogen and fluorescent light sources. In the next two years significant improvement of devices material and technology are expected.*

development of driving circuit and control systems, and (iv) assessment of characterization, standardization and regulation tools.

The work reported in the present Ph.D. thesis is focused on the first two aspects of research gaps (material and device characterization and reliability). Concerning the other two fields of research, the driving circuits issue will be overcome by companies working on LED based application, and the scientific community of Power Electronics. On the other hand, the U.S. Dept. Of Energy is facing the issue concerning the standardization of LED systems, by means of the Commercially Available LED Product Evaluation and Reporting (CALiPER) program. This latter program, started in 2007 and still in run, is making a benchmark work on different SSL applications based on LED technology, and compared to traditional light sources.

In the following we summarize the main issues that are relevant for the present research project.

## 1.2 Issues at material and chip level

The issues that still affects the performances and reliability are related to the different LED technologies analyzed. Since the technology for GaN eterostructures growth is mature, there's not still room for great improvements in terms of quantum internal efficiency. However, the scientific community is focusing its attention on resolving several issues related to GaN based structures:

- the interaction between Mg-dopant and hydrogen limits the density of hole in the active region, thus limiting the internal quantum efficiency of devices [2, 3];

- in three primary color LEDs, the efficiency of the green device is still insufficient, and high-efficiency green LEDs have not been realized by III group nitrides yet, due to (i)

the large internal electrical field and (ii) the defects generation caused by large lattice mismatch between GaN and InGaN layer [4];

- the metal electro-migration along threading dislocations or tube defects [5];
- the degradation of the ohmic contacts of the devices [6, 7], with subsequent increase of the operating voltage;
- the generation/propagation of non-radiative defects towards the active layer of the devices [8, 9, 10], enhanced at dislocation sites [11].

While the InGaN/GaN based technology is affected by the previous issues, that at the time of writing does not heavily affect the reliability of devices, more efforts on AlGaN based devices must be spent in order to improve the quantum efficiency. Since the technology for industrial AlGaN growth is still in an early stage, the issues affecting LEDs emitting in the deep UV are several:

- It is difficult to obtain high-quality AlGaN materials due to the low diffusion length of Al atom or the Al-containing molecules on the surface;
- The growth of AlN-AlGaN buffer layers on sapphire substrates results in dislocations densities that are larger than the dislocation densities of GaN buffer layers on sapphire. The relatively high dislocation densities in AlGaN based deep-UV LEDs may be a limiting factor in the internal quantum efficiency of the devices (currently around 1%);
- AlGaN multi-quantum well structures employed in deep-UV LEDs suffer from large internal piezoelectric and spontaneous polarization induced fields when grown along the c-plane. These electric fields, which are on the order of 1 MV/cm, can reduce the radiative efficiency of the LEDs.
- Room-temperature LED performance is limited mostly by poor electron confinement in the QW region as well as large deep level assisted recombination in p-AlGaN layers [12];
- Lack of transparent contact layer and indium segregation is another reason to cause the reduction of light emission [13];
- Sapphire, that is usually adopted as substrate for these devices, is a relatively poor thermal conductor. The poor electrical conductivity of AlGaN materials was found to exacerbate the current crowding and localized heating problems [12].

## 1.3 Issues at device level

The substitution of traditional light sources with LED base lamps is in act since the last years. The need for high performances, high efficiency and high reliability devices must front several open issues at device level. In particular, the factors that still limit the efficiency and reliability of High Brightness LEDs used in SSL are (i) the thermal management and (ii) the chromatic performances and stability over time.

**Thermal management** In the Fig. 1.2 the (a) current and (b) predicted thermal management of one representative HB LEDs is provided. As can be noticed, the thermal management at chip and lamp level and the identification of the technological weaknesses that limit the high-temperature and high/current reliability of the devices are critical. These information are the starting point for the design of high power/high reliability solid-state based light sources. The high temperature reached by the junction during operation can afflicts the performances of devices [14] and activate several degradation processes:

- the browning of the encapsulation and the package that implies a lumen decay [15, 16, 17] or a spectral degradation [18];
- the modification of electrical and thermal properties due to partial detachment of the chip from the copper frame of the package [19, 20];
- the total failure due to the thermally activated generation of parasitic low-impedance paths that short the junction [21];

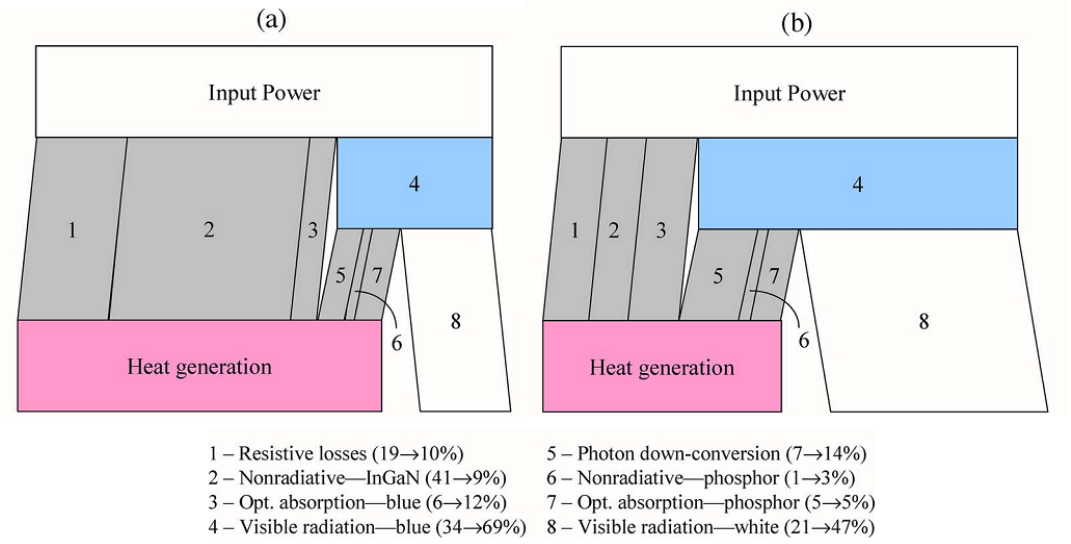


*Figure 1.2: Schematic of heat distribution in (a) present and (b) predicted LED systems. The development of new materials and structures will permit an efficiency increase from 21% to 47% [22].*

**Chromatic performances** Several parameters used to describe the chromatic qualities of white LEDs are available: the Correlated Color Temperature (CCT), the X and Y CIE values in the chromatic space, the Chromatic Rendering Index CRI). Depending on which properties is taken into account, and the final cost of the application, the solutions for LED based SSL are different.

Concerning the phosphor converted approach, new phosphors concepts are continuously emerging: however, little is known of the long-term stability of these materials, thus requiring further characterization studies. Major drawbacks of phosphor-converted white LEDs are:

- limited efficiency due to waste of energy in the down-conversion process;

- limited possibility of designing a high quality light spectrum;
- impossibility of compensating ageing drifts of the LED and phosphors, resulting in changes in the white light spectral properties with time.

A in-depth analysis on present solution adopted for phosphor converted LEDs has been reported in 2.2.3.

## 1.4 Specific goals

The Ph.D project presented in this thesis aimed at contributing to the investigation on degradation mechanisms related to GaN based LEDs, and the development of model which can provide a lifetime prediction. In particular, the work aimed at:

1. finding a correlation between thermal properties and lumen maintenance of GaN based LEDs;
2. improving the knowledge on thermal properties of LEDs, and finding the best solution for heat removal in terms of structures and materials;
3. identifying the failure modes responsible for luminous decay of white LEDs, isolating the different physical mechanisms;
4. obtaining the analytical models for degradation that makes possible the lifetime estimation;
5. developing several measurement setup for optical, electrical and thermal characterization on wide set of devices, and the analytical methods to interpret the results;
6. developing experimental setup for Accelerated Lifetime Testing under different environmental conditions on wide set of devices;
7. giving a feedback on product quality and reliability to LEDs manufacturers;
8. applying statistical methods to ALT design and reliability analysis.

These goals have been achieved working in the Microelectronic Group of the Dept. of Information Engineering , University of Padova. Thanks to the long expertise on characterization of microelectronic and optoelectronic devices and the related reliability analysis skills, the work has been carried out in close collaboration with the experienced scientific staff of the laboratory. During the project several national and international companies working on LED manufacturing have been involved for devices supply and the information exchange. In addition, the facilities and the knowledge of several academic partners (University of Parma, Cagliari, Bologna) contributed to the realization of this work.

## 1.5 Thesis overview

The thesis is organized in several chapters:

1. **Introduction**

2. **State of the Art** A brief overview of LED technology and characteristics, a list of degradation mechanisms found in the literature, the analysis of three case studies on LED reliability

3. **Thermal Issue** The thermal properties of GaN based LEDs, the different techniques for characterization, a description of experimental approaches of electrical characterization of thermal properties, the comparison of experimental results with simulation analysis

4. **ALT of low-flux LEDs** The characterization and accelerated electro-thermal ageing of low-flux white GaN based LEDs with different structure and package composition, the identification of failure modes and the degradation model

5. **ALT on HB-LEDs** Thermal characterization of Chip-On-Board technology GaN LEDs, an accelerated thermal and thermo-electric stress on wide number of samples, the lifetime estimation and identification of failure modes

6. **Reliability of UV LEDs** A reliability analysis on several AlGaN based LEDs emitting in Deep UV region, the analysis on optical and spectral characteristics related to recombination mechanisms, the identification of degradation mechanisms and failure modes

7. **Conclusions**

# Chapter 2

# Light Emitting Diode and Reliability

*The chapter provides an introduction on LED technology and reliability. In particular, the characteristics of devices are presented, focusing on GaN based structure. An overview of the LED structure design and the white generation techniques is provided, with a perspective on Solid State Lighting applications. The attention is focused on the performances of the state of the art device. Finally, three case studies on LED reliability are presented, focusing on the degradation mechanisms identification and the experimental approach, in order to provide the scientific substrate needed for the following chapters.*

## 2.1 LED in brief

In the following chapters the description of different reliability test on LEDs will be provided. Since the lifetime analysis is based on measurements of the properties of LEDs, it's important to know the characteristics of a LED, from the operating principle to the optical behaviour. Thus, this section will provide a brief overview of LEDs optical, electrical and thermal characteristics. For an in-depth description of LED properties, we recommend to go to specific literature [23, 24, 25].

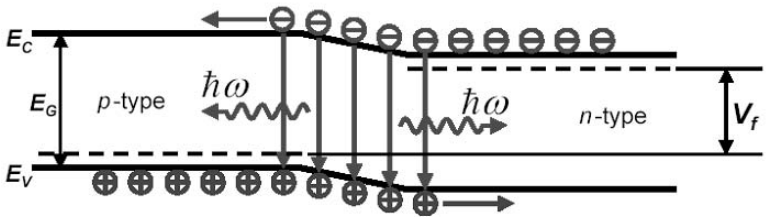


*Figure 2.1: Schematic of a $p-n$ junction under bias: the electron-hole pairs recombine and generate photons with frequency related to the energy gap of the semiconductor.*

### 2.1.1 Operating Principle

In first approximation, a Light Emitting Diode is a $p-n$ junction where the generation and recombination process of electron-hole pairs is strongly localized. If an electric field is applied to the junction, the electron-hole pairs are generated. Then, the carriers can recombine directly

(band-to-band transition), generating a photon, or recombine through a deep level, thus generating a phonon. The wavelength of the emission is dependent on the energy transition of the electron. A schematic of the operating principle of a $p-n$ junction has been reported in Fig. 2.1.

**Energy band gap and compound semiconductors** As was mentioned before, the band gap of the semiconductor used for the emitting device influence the frequency (wavelength) of the radiation. In Fig. 2.2 the energy band gap vs. lattice constant of different compound semiconductors used for optoelectronic devices is reported [22]. As can be noticed, two families of semiconductors are available: the III-Nitride and the III-Phosphide. The first group is based on GaN, together with its alloys of AlGaN and InGaN for tuning of the emission wavelength. Nowadays, the emission wavelength of GaN based semiconductors ranges from $265\ \mathrm{nm}$ (UV-C) to $550\ \mathrm{nm}$ (green), with the efficiency peak placed in the blue emission. Since the first GaN-based optoelectronic devices appeared in the 1995 [26], the main efforts of the scientific community are being spent on these semiconductors, especially in the emission range with the poorest efficiency (i.e. green and UV emission). In addition, the characterization and reliability works reported in this thesis are based on GaN LEDs.

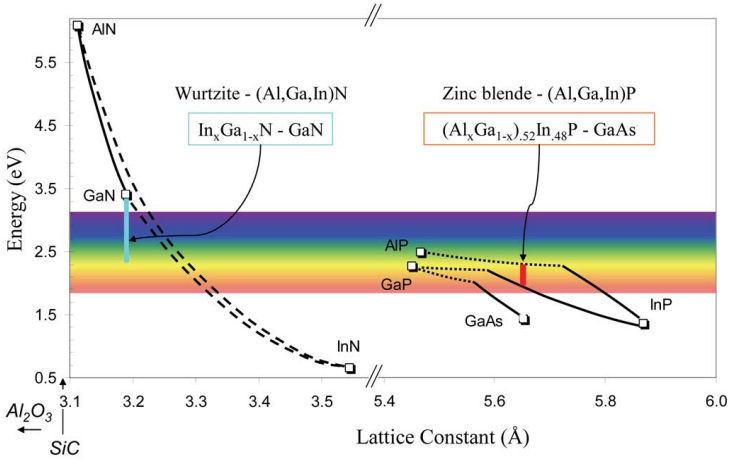


*Figure 2.2: Energy-emission vs. lattice constant for III-Nitride and III-Phosphide compound semiconductors. Solid lines indicate direct-bandgap alloys, dotted lines indicate indirect-bandgap alloys, and dashed lines are estimates (due to relative uncertainty in bowing parameters for high InN-fraction alloys) [22].*

On the other hand, the optoelectronic devices based on III-Phosphide semiconductor have been the first working and commercialized devices. The compound semiconductors based on phosphorus permit an emission wavelength ranging from $580\ \mathrm{nm}$ (green) to $650\ \mathrm{nm}$ (yellow). Also in this case there is an efficiency peak in the red emission. Since the optoelectronic devices based on phosphide have a long history, there is no room for improvement in terms of performances and reliability and they have not taken into account in this work.

**Recombination rate and carrier lifetime** There are two different recombination processes inside a semiconductor:

- **radiative recombination:** it happens when a band-to-band transition induces emission around the main wavelength; it represents the useful component of the emission;
- **non radiative recombination:** it is mainly related to the presence of defects in the lattice and generate (i) an emission with lower wavelength than the main peak and/or (ii) phonon scattering, that induces the heat generation; this is the radiation to avoid. It includes the trap-assisted recombination, the surface recombination and the Auger recombination.

Since both recombination processes are present in a semiconductor, it's important to define some properties related to these recombinations. Considering a p-type semiconductor under high-injection conditions ($n \simeq n' \gg n_0$ e $p \simeq p' \gg p_0$), we can define the carrier recombination rate as

$$R(n) = \sigma_e v_{th} N_t n + S_e A_s n + C n^3 + B_{sp} n^2 \tag{2.1}$$

where $C$ and $B_{sp}$ (Auger and radiative recombination) depend on material characteristics and $N_t$ and $S_e$ (trap-assisted and superficial recombination) are related to the crystal quality. The definition of recombination rate is close to the electrons lifetime

$$\tau_n = \frac{n}{R(n)} = \frac{1}{\sigma_e v_{th} N_t + S_e A_s + C n^2 + B_{sp} n} \tag{2.2}$$

where lifetime indicates the time needed for a population reduction of 1/e. Carrier lifetime can be subdivided in radiative and non-radiative recombination components:

$$\frac{1}{\tau_n} = \frac{1}{\tau_{nr}} + \frac{1}{\tau_r} \tag{2.3}$$

where $\tau_r$ is equal to

$$\tau_r = \frac{n'}{R_r} = \frac{1}{B_{sp}(p_0 + n_0 + n')}. \tag{2.4}$$

In low injection conditions the excited electrons recombine with the holes provided by the dopant, $p_0 \gg n_0$, $p_0 > n'$, and the equation turns in

$$\tau_r \simeq \frac{1}{B_{sp} p_0} \tag{2.5}$$

while in high injection we have $n' \gg p_0$, providing

$$\tau_r \simeq \frac{1}{B_{sp} n'}. \tag{2.6}$$

All these parameters are useful for the definition of internal quantum efficiency, that is the ratio between radiative lifetime of carriers and the total lifetime:

$$\eta_i = \left(\frac{1}{\tau_r}\right) / \left(\frac{1}{\tau_n}\right) = \frac{1}{1 + \frac{\tau_r}{\tau_{nr}}} \tag{2.7}$$

that combined with eq. 2.4 provides

$$\eta_i = B_{sp}\tau_n(p_0 + n_0 + n'). \tag{2.8}$$

### 2.1.2 Optical characteristics

In order to understand the optical measurements that will be analyzed in this work, an brief explanation of the physical mechanism below the optical emission will be provided.

In first approximation, the optical power is the number of emitted photons times the photon energies, that is $h\nu$. The photons number will be related to the injected electrons times the internal quantum efficiency:

$$P_{att} = h\nu\left(\frac{\eta_i J}{qd}\right). \tag{2.9}$$

If one substitutes the internal efficiency from 2.8, it obtains

$$P_{att} = h\nu B_{sp}\left(p_0 + n_0 + \frac{\tau_n J}{qd}\right) \tag{2.10}$$

where $\tau_n$ indicates the lifetime of the injected carriers. Under low injection conditions ($p_0,\ n_0 \gg \tau_n J/qd$), in a p-type active region ($p_0 > n_0$), one obtains:

$$P_{att-p} = h\nu B_{sp} p_0 \frac{\tau_e J}{qd} \tag{2.11}$$

while for a n type

$$P_{att-n} = h\nu B_{sp} n_0 \frac{\tau_h J}{qd} \tag{2.12}$$

On the other hand, under high injection conditions one has $\tau_n J/qd \gg p_0, n_0$ and thus

$$P_{att} = h\nu B_{sp}\left(\frac{\tau_n J}{qd}\right)^2. \tag{2.13}$$

As can be noticed, the optical power behaviour vs. injected current will be linear for low injection and parabolic for high current levels. However, we also must take into account that the carriers lifetime is dependent on their density, and at high current levels some thermal issues arise.

**Efficiency** The internal quantum efficiency previously defined cannot provide a qualitative information on efficiency. For the application design one needs the efficiency expressed as the ratio between emitted optical power and input electrical power, called conversion efficiency:

$$\eta_{cv} = \frac{P_{out}}{P_{e-in}} \times 100. \tag{2.14}$$

An other useful definition is the external quantum efficiency that is the ratio between the amount of emitted photons and the injected electrons:

$$\eta_{ext} = \left(\frac{P_{out}}{h\nu}\right) / \left(\frac{I_F}{q}\right) = \frac{P_{out}}{I_F E_g} \times 100 \tag{2.15}$$

where $I_F$ represents the injected current and $E_g$ the energy bandgap. Thus the conversion efficiency can be rewritten as

$$\eta_{cv} = \eta_{ext} \frac{E_g}{V_j} \tag{2.16}$$

where $V_j$ represents the voltage applied to the junction. Generally, $V_j > E_g$ due to the series resistance; thus one may infer that the conversion efficiency is lower than the external efficiency. The external efficiency can be rewritten as the product between external quantum efficiency and the extraction efficiency, that is defined as:

$$\eta_{out} = \frac{P_{out}}{(S_{att} d_{att}) P_{att}} \tag{2.17}$$

where the product $S_{att} d_{att}$ represents the volume of the active region.

In a LED, the internal quantum efficiency is influenced by the recombination rate in the active region: a high crystal quality and a high and uniform activation of the dopant can allow high internal efficiency values. On the other hand, the external quantum efficiency is influenced by the chip size and geometry, the location of the electrical contacts, the interface with the ambient, and so on.

*Table 2.1: State of the art and possible scenario of efficiency values in* $1\mathrm{X}1\ \mathrm{mm}^2$ *white LEDs biased at* $2\ \mathrm{A}$ *[27].*

| Parameter | | Today | Future |
|---|---|---|---|
| Extraction efficiency | $\eta_{out}(\%)$ | 80 | 90 |
| Internal Quantum efficiency | $\eta_i(\%)$ | 45 | 90 |
| Forward Voltage | $V_f(V)$ | 4 | 3.6 |
| External Quantum efficiency | $\eta_{ext}(\%)$ | 36 | 82 |
| Power conversion efficiency | $\eta_{cv}(\%)$ | 25 | 63 |
| Phosphor conversion | $(\mathrm{lm}/W_{opt})$ | 200 | 240 |
| Luminous efficacy | $LE(\mathrm{lm/W})$ | 50 | 150 |

In Tab. 2.1 some efficiency values for the state of the art LEDs for general lighting has been reported. In addition, the previsions on the performances of future devices have been included. As can be noticed, these is still room for great improvements in terms of internal and external quantum efficiency.

**The behaviour of light output vs. current plot (L-I)** In the Fig. 2.3 an explicative plot of Light output vs. injected current (L-I) has been reported. One may notice three different behaviour at increasing current: quadratic, linear and sub-linear.

A brief explanation can be provided[28]. One has to consider the continuity equation for

the electrons:

$$\frac{dn}{dt} = \frac{J}{qd} - An - Bn^2 \tag{2.18}$$

where $J$ represents the current density, $d$ the layer thickness and $A(B)$ the non-radiative (radiative) recombination coefficient. Under the hypothesis of steady-state conditions, one has $dn/dt = 0$ and under low injection conditions $An \gg Bn^2$. This holds $n = \frac{1}{A}\left(\frac{J}{qd}\right)$ and then:

$$L = Bn^2 \simeq \frac{B}{A^2}\left(\frac{J}{qd}\right)^2, \tag{2.19}$$

where L represents the optical power. Thus at low current levels, L is proportional to the square of $J$. On the other hand, as the current increases, the term $Bn^2$ predominates and the emission starts to be linear with the $J$, until the self heating limits the emission (the sub-linear behaviour).

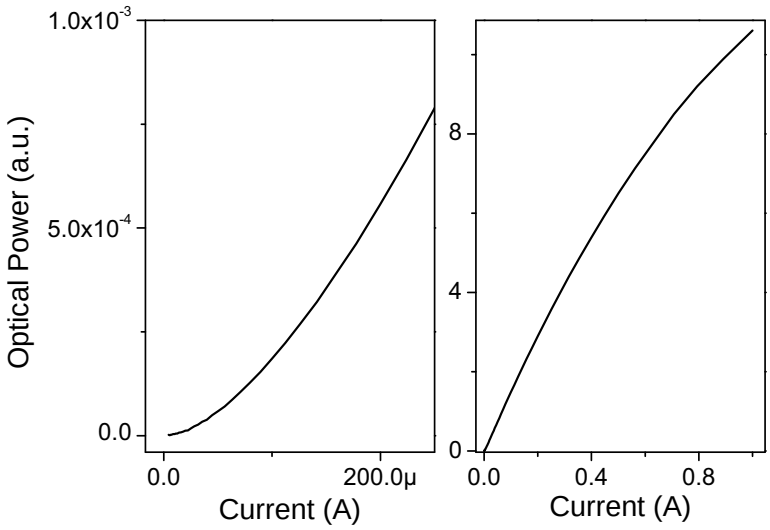


*Figure 2.3: Light output vs. current in a power LED. On the left the magnification of the plot in the low current region has been reported, in order to show the quadratic behaviour of the plot.*

### 2.1.3 Electrical characteristics

**I-V behaviour: forward voltage** In first approximation, the current of a $pn$ junction can be expressed as:

$$I_F = A_{pn}(J_{diff} + J_{NR}) + A_{sur}J_{sur} \;\propto\; \exp\left(\frac{q\,V_F}{a_i k_B T}\right), \tag{2.20}$$

where $a_i$ represents the ideality factor, $V_F$ the voltage applied, $A_{pn}$ the active area and $A_{sur}$ the whole surface area. The components $J_{NR}$, $J_{diff}$ and $J_{sur}$ have different origins.

The diffusion current $J_{diff}$ can be expressed as:

$$J_{diff} = J_{s0}\left[\exp\left(\frac{q\,V}{2k_B T}\right)\right], \tag{2.21}$$

where $J_{s0}$ indicates the saturation current, that depends on the energy band gap and on dopant density. This component is related to the radiative recombination. The generation-recombination current ($J_{NR}$) and surface current ($J_{sur}$) are related to non-radiative recombination caused by the presence of defects in the bandgap and on the surface. They can be expressed as:

$$J_{NR} = \left(\frac{q\,W}{2}\right) n_i \sigma_r v_{th} N_t \exp\left(\frac{q\,V}{2k_B T}\right) J_{sur} = A_{const} \exp\left(\frac{q\,V}{2k_B T}\right) \tag{2.22}$$

In this case the ideality factor is 2.

In Fig. 2.4 the behaviour of I-V in the forward region has been represented. Three conduction kinetics can be detected.

The first is below the μA and it is called low injection region. Here the generation-recombination current predominates. In the second, beyond 2 V, the diffusion current predominates, with a lower ideality factor. In the third region the ideality factor is still higher: this is the high injection region, dominated by the series resistance of the neutral regions.

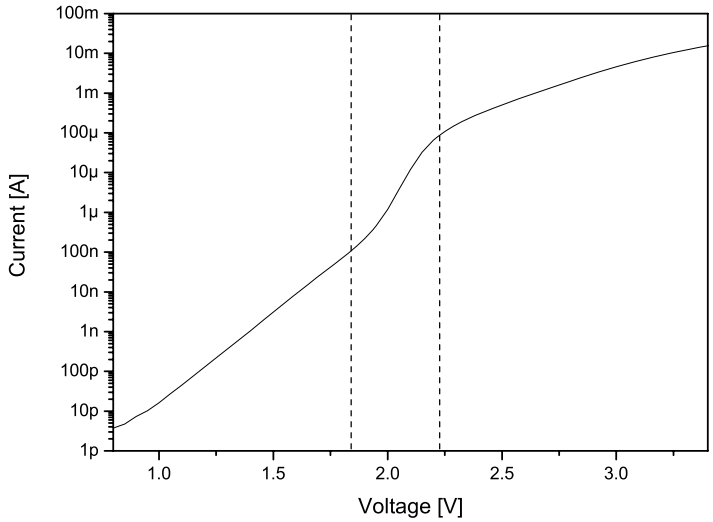


*Figure 2.4: Current vs. forward Voltage characteristics of one representative LED. The three conduction mechanism are clearly visible.*

**I-V behaviour: reverse voltage** The equation that governs the current in reverse bias region is:

$$I_R = A_{pn}(J_{s0} + J_{NR}) + A_{sur} J_{sur} \tag{2.23}$$

with the same parameters used in 2.20. In this case, the carriers do not diffuse and there is not the diffusion current component. In the low current region the saturation current $J_{s0}$ predominates. With increasing current, the effects of generation-recombination current start to prevail.

### 2.1.4 Thermal properties

The aspect of the thermal management is the core of this thesis, since the reliability of new generation LEDs is strongly related to the heat removal capability. Thus, the chapter 3 will be entirely dedicated to the analysis of the thermal properties of the LEDs.

## 2.2 LED structure

The reliability of a GaN-based LED is of course closely related to the structure of the device. In this section we will provide several examples of LED structures, distinguishing between chip and package structure. In addition, some details on white generation will be provided, since are related to the package structure of a LED and the presence of structures for white generation are involved in the degradation of the devices.

### 2.2.1 Chip design

Since the implementation of the first blue emitting device [26], the chip structure design has been involved in a continue evolution. The aim of this evolution is the improvement of the internal and, above all, the external quantum efficiency. The main technological steps are reported in Fig. 2.5. Here the radiant power reached for different chip structure on the last decade is reported [29]. As can be noticed, three structures design have been proposed.

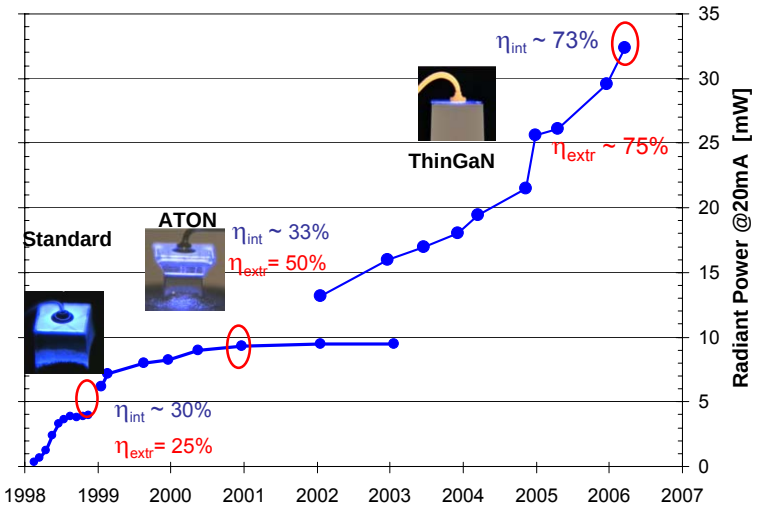


*Figure 2.5: The road map of the InGaN LED efficiency. In the plot are reported the achievements in the chip structure design and the internal and external quantum efficiency reached at each technological step [29].*

**Standard structure** The first GaN LEDs have been designed as cubic dies. Two different approaches have been followed, according to the substrate properties. The vertical structure is based on SiC substrate (the example of a biased vertical chip is reported in Fig. 2.5). The active area is basically composed by an undoped InGaN-GaN Single or Multi Quantum Well,

sliced between doped AlGaN layers that act as carrier blocking layers. The electrical contacts are placed on the two ends of the chip.

On the other hand, the structure based on sapphire is more planar: the p side is grown on the substrate and the n side cover a partial area, since the conduction is lateral. The two contacts are placed on the top. A visual distinction of these two structures is reported in Fig. 4.2.

The standard structure permitted low values for internal and external efficiency, respectively 30% and 25%. The main issue of this structure are the optical loss inside the substrate, due to the Total Internal Reflections (TIR). In addition, the technology used for GaN deposition was early and the crystal quality was low, inducing a grat amount of non-radiative processes.

**Truncated Inverted Pyramid** The Truncated Inverted Pyramid (TIP) or ATON in Fig. 2.5 structure has been designed with the aim of limit the TIR. This goal was achieved shaping the die with oblique wall. The angle of the walls was necessary to eliminate the TIR caused by the optical interface between GaN and air. This solution permitted to increase the external efficiency, but the internal was still limited by the growing process that remained did not observed any improvement.

**ThinGaN** The issues of internal and external quantum efficiency were overcome with the implementation of the ThinGaN approach, by OSRAM O.S. [30]. In this case, the emission is strongly localized in the active area, due to the inclusion of a reflection layer below the active area. In addition, there have been several improvements on the grow process, giving straightforward results in terms of internal and external quantum efficiency (73% and 75% respectively).

### 2.2.2 Package design

The package design is very important for a good thermal management and constitutes a proper interface between the chip and the world. Also in this case the improvements in these last years were straightforward. The package optimization was performed mainly for power LEDs for general lighting, due to the issues of heat removal and high luminous flux. In Fig. 3.3 (described in the following chapter) a visual road map of the package optimization in terms of heat removal is reported.

### 2.2.3 White generation

Since the GaN based technology has been available for blue LED manufacturing [26], several solutions for inorganic LED-based generation of white light have been designed. The white light generation is fundamental to obtain light sources for general lighting, back-lighting, automotive, etc. The choice of the suitable solution depends on the final application performances, costs and reliability. In the following the different approaches are described in details.

**Blue InGaN LEDs with Yellow conversion Phosphors** The coupling of blue light generated by LED source and phosphors for yellow conversion has been the first solution developed for white generation [31, 32, 33]. The motivation of the rapid development and distribution must

be addressed to the low costs of such structures: the availability of high efficiency blue LEDs, a consolidated experience in YAG phosphors and application, the ease of driving. On the other hand, compared to other solutions the Phosphor Converted LEDs (PC-LEDs) exhibit the worst profile in terms of optical properties.

The operating principle of PC-LEDs is based on the matching of the emission wavelength of InGaN LEDs (ranging in $470 - 450$ nm) and the excitation spectra of $Y_3Al_5O_{12} : Ce^{3+}$ (YAG) phosphors, already employed in discharge-lamps technology. In addition, the yellow emission of phosphors added to the blue component permits a white point with a Correlated Color Temperature (CCT) of $4000 - 8000$ K. Furthermore, by modifying the quantity of phosphors one can modulate the CCT of the white [22].

However, the Color Rendering Index (CRI) of such solution hardly goes beyond 80-85, corresponding to a less warm light. This would be a negative aspects in such applications where the chromatic rendering is crucial, i.e. for works of art illumination or display back-lighting. The problem of cold white is relevant when comparing PC-LEDs spectra with traditional lighting source as incandescence bulbs and fluorescent based lamps. In Fig. 2.6 the comparison between different desk lights have been reported (the figure was taken from the report of SSL benchmark performed by the US Department Of Energy [34]). In the figure the spectra of PC/LEDs with different phosphors composition have been compared with the incandescence (CRI=100), halogen and fluorescent spectra. The lack of red component and the predominance of blue emission give the cold white feeling, typical of fluorescent lamps that use phosphors.

Several design attempts have been performed in order to guarantee a higher CRI. The viable solution adopted instead of using different pumping wavelength (reported afterward) is the inclusion of phosphors for green and red conversion in the LED. An interesting solution is given by nitride-based $Eu^{2+}$ phosphors [22] that exhibits good quantum efficiency and good thermal quenching behaviour. The spectra of LED equipped with these phosphors is reported in Fig. 2.7(a). The substitution of more efficient phosphors alloy permits to obtain higher CRI values. On the other hand, the use of such phosphors has a drawback: due to a lower conversion efficiency with respect to YAG phosphors, the new generation PC-LEDs exhibit a lumen efficacy loss (Fig. 2.7(a)).

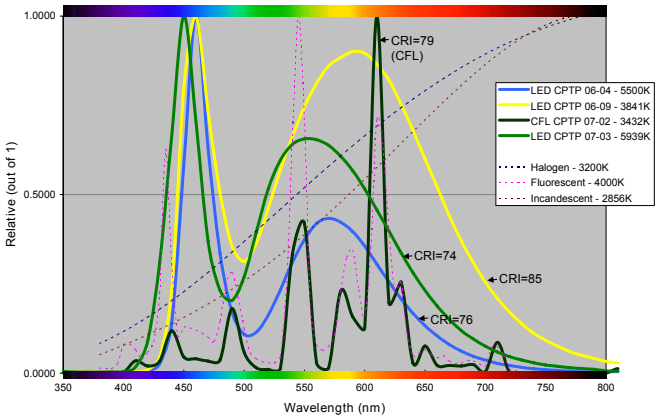


*Figure 2.6: Comparison between GaN-based PC-LEDs and other traditional light sources for desk-lighting applications.*

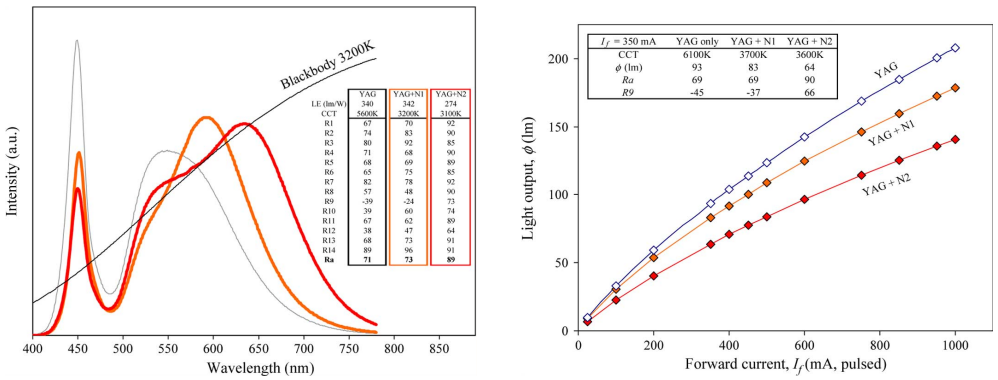


*Figure 2.7: Comparison between different phosphors composition: the impact on (a) CRI reported in the table, and (b) on the luminous efficacy.*

The structure of PC-LEDs is based on a blue InGaN LED attached on the reflector cup of the package and YAG phosphors are placed on the top. There are different approaches to couple the phosphors: some manufacturers distribute the phosphors on the LED surface, others place the epoxy lens including the phosphors, with different impact on the emission profile [35].

**Red-Green-Blue multi-chip approach** As suggested by the name, the multi-chip approach is based on color mixing of three different color sources. In the case of white light generation, the three colors adopted are red (AlInGaP), green (InGaN) and blue (GaN). Since these three colors are placed in the three vertices of the CIE color map, every tone can be obtained by single color modulation. In particular, this solution can provide white light with different color temperatures, from a cold white to a warmer white comparable to black body radiation. Since the LEDs are driven separately, a complete driving circuitry equipped with sensor for feedback and capable to modulate the color and compensate the degradation can be implemented [36].

However, all these features are not for free. Several drawbacks must be addressed:

- the three LEDs have to be driven separately,
- the optical coupling of different sources is not-trivial,
- the high power green LEDs issue must be solved (reported afterward)
- the degradation rate of each chip is not the same and the chromatic properties of the output tend to vary during operation.

In conclusion, R-G-B multi-chip approach represents the more complete and quality solutions for SSL, but the high production and life costs make it suitable for high-end applications.

**UV AlGaN LEDs with Phosphors** This approach is similar to the standard PC-LEDs configuration, but it's based on Ultra Violet LEDs source and different phosphors composition. Since the energy of the pumping UV source is higher than the visible emission, the radiation

could be converted in several colors, as fluorescence lamps do. The UV source is based on InGaN material for near UV emission, and AlGaN for deep UV (see section 6.2 for an overview of latter structures).

Concerning the conversion, Silicate phosphors doped with Eu have shown higher efficiencies than YAG, and improved resistance against UV radiation [37, 38]. Eu-doped tri-color phosphors stimulated by near-UV LEDs have been also presented with CRI up to 92 [39]. Highly stable phosphors based on nitride ceramics have recently been presented: green, yellow and red phosphors based on Eu-doped oxynitrides have been demonstrated [40].

Also in this case different issues limit the product penetration in the lighting market. In particular, the UV source is under development and is afflicted by reliability issues. In addition, there are several restriction in EC regulation on UV emission for lighting.

**Phosphor-free white emitting diode** Since the technology for GaN-based LED growth is recent, only in last years we attended at the possibility of obtaining devices able to emit at different wavelengths from the same substrate. These solutions aim at obtaining white light from a single chip, without phosphors for wavelength conversion, reducing the costs of package processing.

The first approach used was the growth of InGaN/GaN Multi Quantum Well with different indium content [41]. The chip obtained emits in the blue and yellow region. In order to reduce the dislocation density, the quantum well are pre-strained. While the stacked QW approach is being investigated by several research teams, the solution of the laterally distributed QW was experimented [42], in which the blue and green MQWs are adjacent.

Despite the development of these novel techniques is just at the beginning and the efficiency level reached are still low compared to other commercial solutions, the first encouraging results make possible an enhancement in terms of devices performances and a consequent insertion in the SSL market.

## 2.3 Lifetime estimation: case studies

During the last decade, the reliability of GaN-based LEDs was investigated by several authors. The literature can provide a long list of degradation mechanisms and failure modes related to these devices. Instead of providing a fruitless enumeration of such mechanisms, the author will propose several case studies on LED reliability analysis, focusing on the experimental approach and the results analysis.

### 2.3.1 Low-Flux white LEDs

In their work, Narendran et al. [43] analyzed the reliability of low flux while LED. The device analyzed are 5-mm packaged blue LEDs with YAG phosphors for yellow conversion. The main goals of the work are:

- the investigation on the degradation mechanism responsible for lumen decay
- the impact of the phosphor location in the package on the reliability

In order to achieve these goals, they carried out two different experiments

**Experiment I: degradation mechanism** With this experiment, the authors wanted to discriminate the degradation mechanism responsible for lumen decay. The two starting hypothesis are the heat generated and the blue emission: both can induce the yellowing of the encapsulation. In order to prove these hypothesis, two different groups of LEDs have been individuated. The first group has been stressed ad different ambient and current conditions, maintaining the same junction temperature of 95 °C. On the other hand, the stress conditions for the second group have been chosen in order to guarantee the same short-wavelength emission (and thus varying the junction temperature).

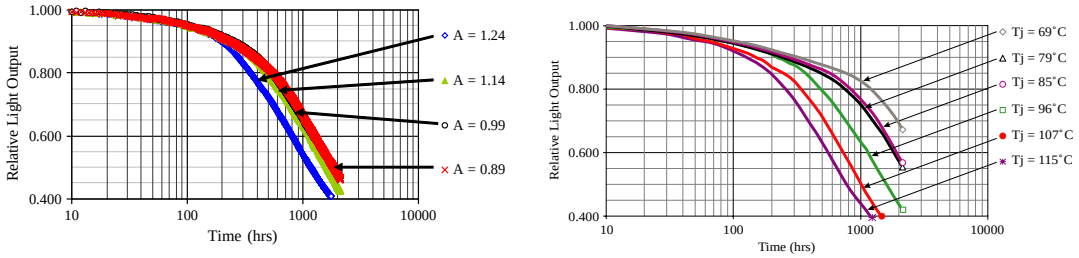


*Figure 2.8: The relative light output degradation for electro-thermally stressed LEDs, maintaining (a) the same junction temperature, and (b) the same short wave emission.*

In Fig. 2.8 the luminous decay kinetics of the two ageing groups have been reported. The decay was induced by the browning of the encapsulation: such process was found to be more thermally activated than emission activated. The reliability analysis used a statistical approach, using 6 LEDs per stress condition. In addition, the two causes of the degradation process have been detected. However, the analysis of the parametric degradation, together with the extrapolation of a degradation model could make the experiment more attractive.

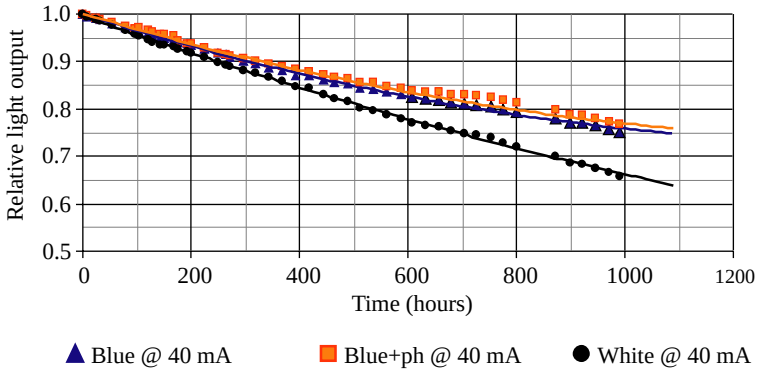


*Figure 2.9: The relative light output degradation for blue LEDs, Blue LEDs with far-located phospors, and white LEDs.*

**Experiment II: phosphors location** The second experiment has been carried out aiming at finding the impact of the phosphors on degradation of white LEDs. It was observed that the

degradation was enhanced for white LEDs instead of blue devices. The hypothesis provided for this behaviour was the isotropic emission of the phosphors, that impacts on the optical properties of the encapsulation. This happens because the radiant emission travel more often on the epoxy than in blue LEDs does.

In order to prove this statement, several blue LEDs, white LEDs with the same blue emission and blue LEDs with phosphors far from the light source have been submitted to ageing at $40\ \mathrm{mA}$. The results of the stress have been reported in Fig. 2.9. The authors noticed that the white LEDs showed the higher degradation rate, while the blue and blue+phosphors LEDs showed the same degradation. The experiment proved the statement that the phosphors inside the encapsulation are responsible for degradation, but not the phosphors themselves.

### 2.3.2 High Brighness LEDs

A similar work on degradation mechanism identification on white LEDs has been carried out by Ishigazi et al. [44]. However, in this case the devices used for experiments were power LEDs. The work aimed at finding the degradation mechanism that limits the lifetime of such devices. In order to obtain results on failure mechanism, the accelerated electro-thermal stress has been used.

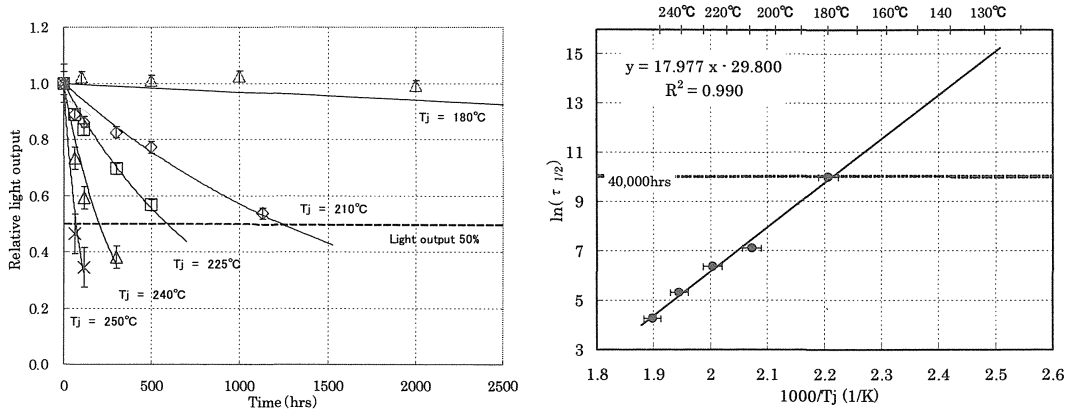


(a) (b)

*Figure 2.10: In (a) the relative light output degradation for electro-thermally stressed LEDs at different junction temperature levels has been reported. The Times To Failure at 50% have been reported in the (b) Arrhenious plot.*

Two different experiment have been carried out: one varying the junction temperature ($185\ ^\circ\mathrm{C} < T_j < 250\ ^\circ\mathrm{C}$), and the other at different current conditions ($0 < I < 190\ \mathrm{mA}$), in order to discriminate the impact of the heat and the current density on the degradation process. Also in this case a statistical approach was used, since 5 LEDs per ageing conditions have been stressed. In Fig. 2.10 the results of the stress performed at various junction temperatures have been reported. The authors noticed that the temperature had a great impact on the degradation, detecting degradation kinetics with exponential behaviour. The Times To Failure for a 50% decay have been reported in the Arrhenious plot (Fig. 2.10(b)), hypothesing an exponential failure mode. The hypothesis was suppoerted by the results, detecting a thermally activated degrada-

tion with an activaion energy of $1.55\ \mathrm{eV}$. Althought the activation energy was higher with respect with other reliability works on LEDs [45], an explanation of the degradation process was not provided.

The second experiment (with increasing current but equal junction temperature) showed that there is not a correlation between current density and degradation rate. The authors proposed an electric field dependence of the degradation, but this hypothesis was not supported by experimental results.

### 2.3.3 60,000 hours-long ageing of AlInGaP LEDs

Despite this work analyzes the reliability of AlInGaP LEDs, while all the other works cited are based on GaN LEDs, it proposes a straightforward analysis approach that represents a good example of reliability study. The most impressive fact of this work by Grillot et al. [46] is the amount of stress time (60,000 hours) and the huge amount of samples stressed. On our knowledge, this is the longer reliability test ever performed on LEDs.

The authors subdivided the work in two main experiments: (i) an electrical stress of 1000 hours at different current levels of devices taken from 10 different wafers, and (ii) the electrical stress of 60,000 hours at fixed current level of LEDs from 10 different wafers and with different chip size. The aim of the first experiment was the demonstration that the degradation at high stress current and low test current is related to traps generation in the active layer. The second experiment demonstrated that the degradation in the long term is monotonic and follows a theoretical model. This model for degradation is expressed as:

$$D = D_1 + D_2 J + (D_3 + D_4 J) \ln t \tag{2.24}$$

where $J$ is the current density, $t$ the time and $D_1 - D_4$ are coefficient related to the LED.

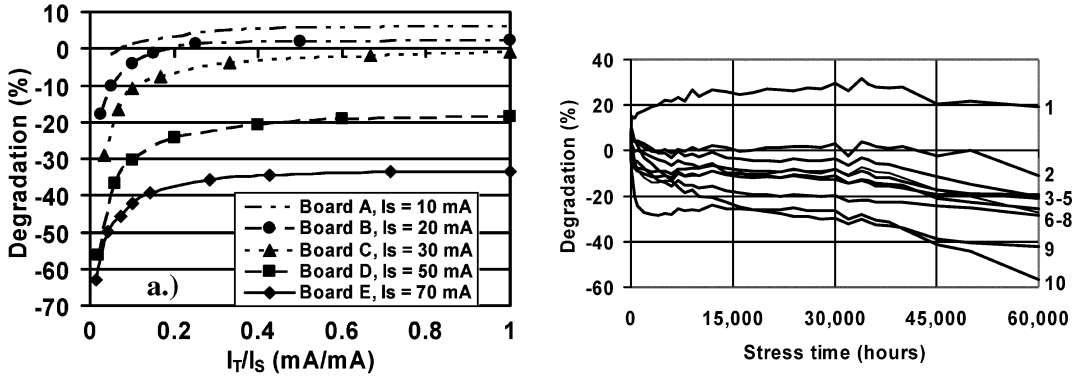


*(a)* *(b)*

*Figure 2.11: Degradation of AlInGaP LEDs. In (a) the plot of the degradation vs. the ratio of the test current and the stress current ($I_T/I_C$) measured at 1000 hours has been reported. The plot reported in (b) represents the degradation of the optical power for LEDs taken from 10 different wafers, stressed in the same conditions.*

In Fig. 2.11(a) an example of the degradation at 1000 hours of LEDs stressed at different current densities has been reported. As can be noticed, the shape of the plots is always the

same, providing the hypothesis of trap assisted degradation process. The degradation of LEDs from different wafers has been reported in Fig. 2.11(b). These results permitted to extrapolate a degradation law, since different parameters as chip size, current density and crystal quality were available. In addition the authors provide a strong correlation between the theoretical degradation model and the experimental data. An additional interesting result was that the defect density $N_T(t)$ is a linear function of the stress current.

# Chapter 3

# Thermal characterization, analysis and modeling of LEDs

*This chapter is focused on thermal aspects of Light Emitting Diodes. The thermal properties in LED systems are briefly described. In particular, the results from steady-state and transient characterization are discussed. Furthermore, the experimental solutions for thermal characterization are proposed, and the comparison between different techniques is reported, referring to results available in the literature. The second part of the chapter describes the experimental results of the work on thermal analysis, with the distinction between static and dynamic analysis. Finally, the thermal simulation results by means of Finite Element Modeling are presented, and compared to experimental results.*

## 3.1 Thermal properties in LEDs

### 3.1.1 Thermal impedance

Since the solutions of heat transfer differential equations require a large amount of arithmetics and time, a model that can easily describe the thermal behaviour of semiconductors has been widely adopted. The model is based on the equivalence between the electrical current and the heat flow. In this model, the heat generated by an active device is modeled as a current generator, while the temperature at the interfaces between different materials as the voltage. The equivalence between electrical and thermal model is depicted in Fig. 3.1. Given a simple electrical circuit with a current generator ($I$) connected to a resistance ($R$), we can apply the Ohm law in order to obtain the voltage drop on the resistance ($\Delta V = RI$). The same equation can be applied o the thermal model, where the heat generated ($H$) goes through the interface ($R_{th}$), dissipating heat and generating a temperature difference ($\Delta T = R_{th}H$). The $R_{th}$ parameters is called thermal resistance, and is a fundamental property of device, since it indicate which temperature level can reach the active region while the device is operating. This statement can be easily understood if we consider the Fig. 3.1. We may suppose that the heat generated as the input electrical power, and the temperature at the end of the thermal resistance as the ambient temperature ($T_{amb}$). The $\Delta T$ calculated represents the overall heating of the active region (the absolute temperature value will be $\Delta T + T_{amb}$). As in electrical model, the thermal

resistance of a series of resistances is the sum of those resistances. This is important when considering the different interfaces of a device: typically we find the junction-submount interface, the submount-package interface and the package-air interface (or package-heat sink and heat sink-air interface). The temperature of every section of device can be calculated starting from the thermal resistance values.

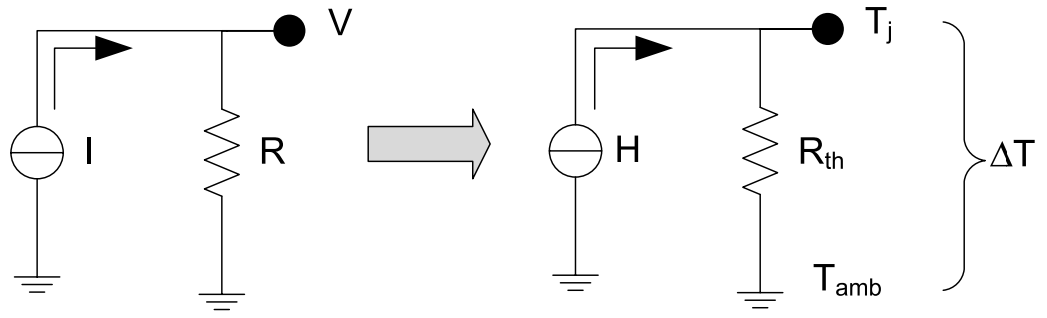


*Figure 3.1: The electrical schematic of a current generator connected to a resistance, used as a model for thermal resistance description.*

The thermal resistance is an important parameters of a semiconductor device, and depends on structural and material properties of the device (interfaces, dimensions and thermal conductivity of materials). It can give immediate information on the thermal performances of a device and can suggest the use and dimension of a heat sink for operation. However, the thermal resistance is a parameter for steady state operation, that can provide the temperature level after an initial transient phase, but does not reveal any information on the thermal behaviour in dynamic conditions. The complete model for thermal behaviour thus will include the heat capacitance, that corresponds to a capacitance in parallel to the resistance in our electrical equivalent (see Fig. 3.2). The heat capacitance is related to the physical property of the specific heat capacity of the material composing the device and to the density of that material. The heat capacitance provides an inertia to the heating.

Generally speaking, we can identify the thermal impedance ($Z_{th}$) as the parallel between thermal resistance and the heat capacitance. Starting from this basic brick, we can describe every semiconductor device simply by making series of these bricks. The application of this concept and the analysis of the distributed element model will be reported in the following session.

**Thermal impedance in LEDs** Before discussing on thermal resistance of LEDs, we must consider the particular typology of the optoelectronic device. While a common semiconductor device have only an input electrical power component (and a lower output component for dc/dc converters), an optoelectronic device has also an output optical power component. This means that the equation that define the thermal impedance in a LED is

$$Z_{th} = \frac{\Delta T}{P_{in} - P_{opt}} = \frac{\Delta T}{P_{in}(1-\eta)} \tag{3.1}$$

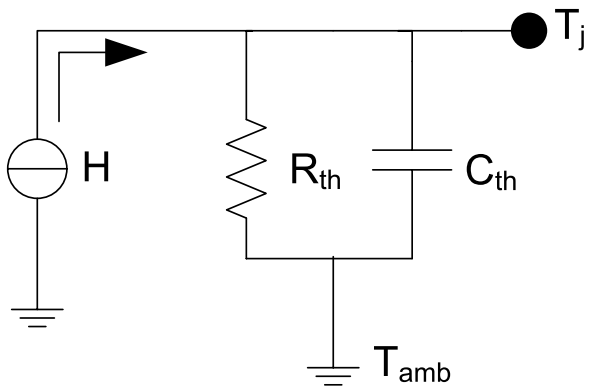


*Figure 3.2: The model of the parallel between thermal resistance and heat capacitance.*

where $\eta = \frac{P_{out}}{P_{in}}$ represents the external quantum efficiency of the device. Since the state-of-the-art devices show efficiency values around 10-20%, the power for thermal resistance calculation could be approximated as the input power, but this effect will be taken into account in few years, when LEDs manufacturer will produce devices with higher efficiency [47, 29].

The thermal resistance in LEDs has seen a decrease with the increasing of optical power, and thus heat generated. Impressing results in terms of thermal resistance decrease have been achieved acting both at semiconductor and package level. The internal quantum efficiency has been increased and the ohmic contacts technology improved, contributing to decrease the heat generated by Joule's law, non radiative recombination and phonons scattering. At the package level, different structure have been designed with the aim of minimize the heat flow path from the junction to the heat sink, and integrating the thermal mass in the device (as the Chip-On-Board technology does). For a visual history of package evolution, look to the Fig. 3.3, taken from [25].

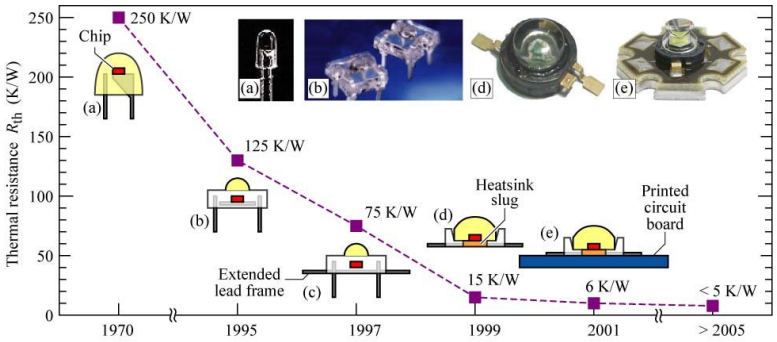


*Figure 3.3: The history of the thermal resistance improvement so far. The design of packages optimized for heat removal permitted a strong decrease in terms of heat generated [25].*

As the output power of new generation LEDs is rapidly increasing, the main concern in device design is represented by the thermal resistance minimization. With high input power levels it's important to improve also the characterization techniques for thermal impedance and thus temperature measurements, since the high temperature levels can affect both the efficiency

and the lifetime of the devices.

### 3.1.2 Temperature transient analysis and Structure Functions

In the latter section we have described the thermal impedance of a LED. As was mentioned, the impedance is the sum of a resistive and capacitive part. While the thermal resistance can be collected in steady state conditions, the analysis of the self-heating transient is required in order to investigate in details the different contributions to the overall thermal impedance. Thus a good thermal analysis relies on an accurate measurement of the thermal transient. This means that the device must be biased with a pulse with the shortest rise time possible, in order to include in the measurement the overall self heating transient.

As was mentioned in the previous section, the thermal impedance can be modeled has the series of basic blocks composed by a parallel between resistance and capacitance. Each thermal resistance represents an interface between different materials, while the heat capacitance is related to each element. Every basic block contribute to the self heating with a specific time constant. As an example, in Fig. 3.4 the self heating transient of a power LED has been reported. In particular, the plot report the transient for the LED biased at nominal conditions with and without a proper heat sink. As can be noticed, two evident time constants can be individuated for the LED biased without the heat sink, at $3\ \mathrm{ms}$ and $30\ \mathrm{s}$. In first approximation, the first thermal $RC$ can be related to the interface between the chip and the package, while the second is related to the interface between the package and the air, since is not optimized for heat removal and presents a low thermal conductivity. On the other hand, the thermal transient measured for the LED with the heat sink has the same behaviour for the first $RC$, but presents a lower second transient. This second transient is related to the interface between the package and the heat sink and is lower due to the high thermal conductivity of the contact. Some details on the experimental setup used for thermal transient measure will be proposed in section 3.4.

The thermal transient analysis is a very useful technique that permits to discriminate each contribution to the thermal resistance of the device. However, the analysis of the transient is not so precise and does not permit to evaluate the exact values of the resistances. Luckily, different analytic techniques have been developed in order to investigate the thermal impedance with more detail. These techniques are based on the analysis of the time constant spectrum, that is the different time constants composing the transient. In the literature two methods and their description are available: the TRAIT method [48], and the structure functions [49]. Since different works on the calculation of the structure functions for optoelectronic devices are available in the literature [47], this latter method has been developed in order to analyze the thermal transient. In the following lines a brief description of the method and its application will be provided, addressing to the literature for a more in-depth explanation.

The structure functions are particular functions that permits to describe the thermal resistance (differential function) and heat capacitance (cumulative function) related with the device structure. These functions can be extrapolated from the thermal transient of the device by means of analytic tools. The analysis is based on the approximation of unidimensional heat flow path from the junction to the ambient. Thanks to this approximation, the deconvolution of the thermal transient with a weighting exponential function can be performed in order to

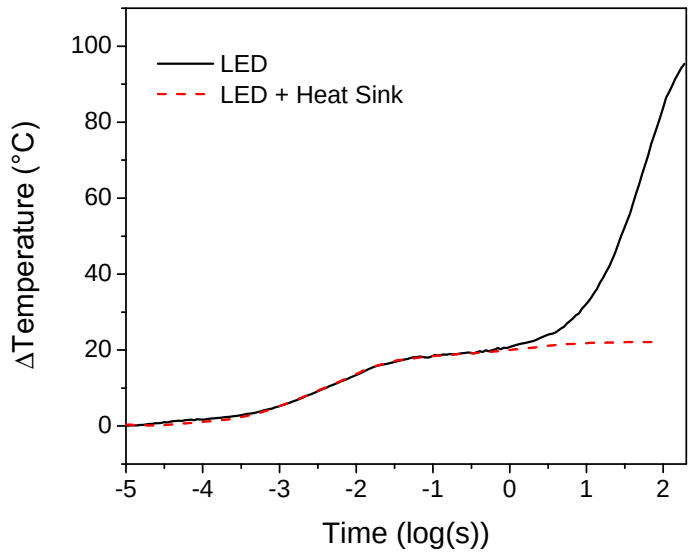


*Figure 3.4: Self heating transients of a power LED with and without the heat sink. As can be noticed, the application of the heat sink influences only the exponential with longer $\tau$.*

extrapolate the time constant spectrum. This spectrum represents the lumped-element Foster model for thermal impedance. The Foster model has to be transformed in Cauer network in order to give a physical meaning to the model. This means that the heat capacitance are placed across a thermal resistance and the ambient, while the deconvolution of the thermal transient returns the time constants of the aforementioned series of single impedances. Finally, this model can be used to represent the cumulative structure function $C_{th}$ (heat capacitance per unit length), and the differential structure function $K$. In particular, this function can be written as

$$K = \frac{C_{th}}{R_{th}} = c\lambda A^2 \tag{3.2}$$

where $c$ is the heat capacitance, $\lambda$ the heat conductivity and $A$ the cross section area of the heat flow. The two structure functions are plotted using cumulative thermal resistance ($\mathrm{K/W}$ ) as x-axis.

In order to explain what does this theory mean, an example of the two structure functions for a power LED without heat sink has been depicted in Fig. 3.5. As was mentioned before, the cumulative structure function represents the heat capacitance of the device across the heat path, with increasing thermal resistance. In the figure can be noticed plateau and steps. Each step corresponds to an interface between different materials, while plateau indicates the heat capacitance of the material beyond the interface toward the ambient. On the other hand, the peaks in the differential function below represent the interfaces. The thermal resistances between the peaks are related to each interface between different materials, and the thermal resistance where we find the asymptote is the overall thermal resistance of the device. In this case, we can easily identify a peak around $16\ \mathrm{K/W}$ that can be attributed to the thermal resistance between the chip and the junction, while the overall thermal resistance is about $76\ \mathrm{K/W}$.

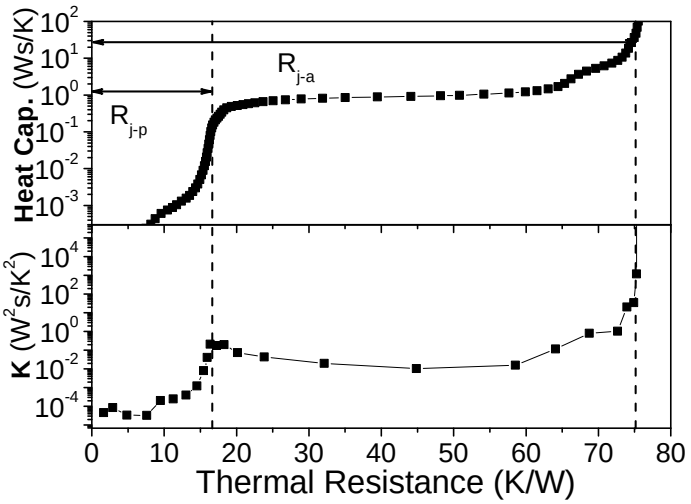


*Figure 3.5: An example of the differential structure function($K$) and its integral function (Heat Capacitance) of a power LED without heat sink. The two contribution to overall thermal resistances are evident ($R_{th} = R_{j-package} + R_{package-air}$).*

These structure function have been collected applying the method described in [49, 50]. The deconvolution and filtering of the transient has been implemented in Matlab, while the conversion from Foster to Cauer network has been realized by a C routine, due to the high precision needed. The structure functions obtained with these tools can be compared to results from commercially available instrument called *T3ster* from MicReD.

## 3.2 Thermal characterization techniques

As mentioned before, the temperature of an operating device play a fundamental role in device efficiency and lifetime. Thus is extremely important to know, with a certain accuracy, the temperature of a device. In addition, the thermal resistance value must be provided to application engineering and a good accuracy is also required. Different techniques have been studied and applied for temperature measurements inside semiconductor devices. Currently the spectrum of available measurement techniques is wide, with different pro and cons. depending on the device under test, one have to select the most appropriate measurement.

We can individuate three different domains for thermal measurement:

1. the electrical methods
2. the optical methods
3. the physical methods

A description of methods belonging to these categories will be provided, with particular attention to techniques already used for LEDs and other opto-electronics devices. For a visual reference of the different measurements techniques, with their pro and cons, go to Tab. 3.6.

| Method | Examples | Advantages | Disadvantages |
|---|---|---|---|
| Electrical | ♦ Junction voltage<br>♦ Threshold voltage<br>♦ Resistance | ♦ Packaged device<br>♦ No contact<br>♦ Potentially subsurface | ♦ Averages<br>♦ May require special device operation |
| Optical | ♦ Infrared emission<br>♦ Reflectance<br>♦ Raman | ♦ Temperature map<br>♦ No contact<br>♦ Good Spatial resolution | ♦ Need surface view<br>♦ Potentially expensive |
| Physical Contact | ♦ Scanning nanoprobe<br>♦ Liquid crystals<br>♦ Thermographic phosphors | ♦ Temperature map<br>♦ Potentially high spatial resolution | ♦ Need surface view<br>♦ Contact may disturb temperature. |

*Figure 3.6: The main categories of thermal measurement [51].*

### 3.2.1 Electrical methods

The thermal estimation based on electrical measurements can be used in particular device families, since is based on the temperature sensitive parameters (like the forward voltage of a p-n junction). The technique is based on two measurements: a calibration phase, used to identify the relationship between the parameter and the temperature, and the measurement of this parameter under operating conditions. The calibration measurement is usually performed by means of a climatic chamber or a Thermo-Electric Cooler (TEC). It's based on the assumption that the junction is at the same temperature of the ambient, thus the self-heating during measurement must be avoided. Starting from this hypothesis, two approaches can be faced: (i) a pulsed calibration measurement, or (ii) the calibration at low input power level. In the latter case, the temperature measurement will be performed switching from operating conditions to low power level, in order to monitor the temperature immediately after the operative conditions.

There are different advantages in using this kind of measurement. First of all, it can be easily implemented by ordinary instruments available in laboratory. Secondly, the measurement can be performed on packaged devices, without any need of physically accessing the semiconductor. Finally, it can reveal information on the true temperature of the junction, that presents the higher temperature value of a device. However, the averaging nature of the electrical measurement does not take into account of the distributed topology of the thermal impedance of a device. This fact implies that the temperature value extrapolated is actually an average of the temperature distribution among the junction and avoid any kind of temperature mapping on the surface of semiconductor.

The parameters used for thermal calculation are the already mentioned forward voltage of a p-n junction, the threshold current of a MOSFET, the series resistance and the current gain $\beta$ of a BJT. For a review of the different techniques, see [51]. On the other hand, we will go into details of the forward voltage measurement method, since is the only electrical measurement technique used for LEDs and p-n junction can be easily found in integrated circuits and other electrical devices.

**Forward Voltage method** The forward voltage of a p-n junction measured at a certain current show a dependence on temperature. Different authors reported the justification of such dependence [52, 53], but we propose the demonstration in details.

We start from the current vs. voltage characteristics of an ideal p-n diode, the Shockley equation:

$$J = J_s(e^{\frac{eV_f}{n_{id}kT}} - 1) \tag{3.3}$$

The term $J_s$ identifies the saturation current, that can be expressed as

$$J_s = e\left[\sqrt{\frac{D_n}{\tau_n}}\frac{n_i^2}{N_D} + \sqrt{\frac{D_p}{\tau_p}}\frac{n_i^2}{N_A}\right] \tag{3.4}$$

where $D_n$ and $D_p$ indicates the diffusion constants, $\tau_n$ and $\tau_p$ the minority carrier lifetimes, $n_i^2$ the intrinsic carrier concentration and $N_A$ and $N_D$ the dopant concentrations. Some of these parameters are temperature dependent. In particular, the intrinsic carrier concentration is expressed as

$$n_i^2 = \sqrt{N_C N_V}e^{-\frac{E_g}{2kT}} \tag{3.5}$$

and since the effective densities of states $N_A$ and $N_D$ are proportional to $T^{3/2}$, one may infer that

$$n_i^2 \propto T^{3/2}e^{-\frac{E_g}{2kT}} \tag{3.6}$$

Since the dependence of the diffusion constants with temperature is low ($D \propto T^{-1/2}$), we do not take into account that contribution. The equation 3.3, considering the case of $V_f \gg kT/e$ can be rewritten as:

$$J = J_s\left(e^{\frac{eV_f}{n_{id}kT}}\right) \tag{3.7}$$

from which the explicit expression for $V_f$ can be extrapolated

$$V_f = \frac{kT}{e}\ln\frac{J}{J_s} \tag{3.8}$$

Driving the diode with constant current ($J = J_f = constant$), and substituting equation 3.6 in 3.8, we obtain

$$V_f \propto \frac{kT}{e}\ln\frac{J}{e\left(\sqrt{\frac{D_n}{\tau_n N_D}} + \sqrt{\frac{D_p}{\tau_p N_A}}\right)T^3 e^{-\frac{E_g}{kT}}} \tag{3.9}$$

where we can indicate with $A$ the term that include the diffusion constants and the dopant concentration

$$A = \sqrt{\frac{D_n}{\tau_n N_D}} + \sqrt{\frac{D_p}{\tau_p N_A}}$$

giving this result

$$V_f \propto \frac{kT}{e} \ln \frac{J}{eAT^3 e^{\frac{-E_g}{kT}}} \tag{3.10}$$

In order to clearly identify the temperature dependence of the forward voltage, we need to differentiate the last equation:

$$\frac{dV_f}{dT} = \frac{d}{dT}\left[\frac{kT}{e} \ln \frac{J}{eAT^3 e^{\frac{-E_g}{kT}}}\right] = \frac{eV_f - E_g}{eT} + \frac{1}{e}\frac{dE_g}{dT} - \frac{3k}{e}$$

It was demonstrated that this model is quite in agreement with experimental data. The practical result of this dissertation is that the forward voltage vs. temperature relationship can be approximated with a linear behaviour. This approach has been used by several authors working on diode, and in particular on LEDs [54, 55]. The method has also widely applied to devices analyzed in this thesis work. In further section the issues we have faced in applying this method will be reported, together with some relevant results.

### 3.2.2 Optical methods

These methods are based on the assumption that some optical properties of the surface of a semiconductor device are temperature sensitive. The optical measurement can be subdivided in two main categories: the stimulated measurements and the emissive measurements. The first category indicates that measurements based on the comparison between incident and reflected (or scattered) light: examples of these techniques are the Photoluminescence Spectra, the Raman Scattering, the reflectance of the surface. In the other case, the device itself is the light source, thus one can measure the electro luminescence spectra (if the emission is generated by an external electrical field), or the Infrared emission, strictly correlated to the temperature (due to the black body radiation).

The optical methods are called non-contacting since no physical probes contact and thus perturb the measurement. In addition, the spatial resolution is dependent on spot size of the optical probe, typically a few nanometers. This feature make possible the thermal mapping of a surface. On the other hand, these kind of measurements can be performed only on those device in which the surface is optically available, and often need equipment expensive and difficult to use.

**Optical methods applied to LEDs** Different optical based setup for temperature estimation has been applied to optoelectronic devices.

The **Infrared radiation** is the more diffuse technique due to cheap and commercially available equipment used. It is based on the assumption that every body emits a spectrum that follows the Planck's law of radiation. Since the integral of the spectrum is temperature-dependent, a direct thermal measurement can be performed. The only disadvantage is the calibration of the emissivity factor, since we are measuring a device that do not show the ideal radiation of a black body.

In Fig. 3.7 the thermal maps of several LEDs have been reported. The technique measure the temperature with a good accuracy in device there the surface is available (Fig. 3.7(a)-(c)),

but artifacts are generated when a lens is placed on the device (Fig. 3.7(d), where the higher temperature are reached around the chip). In addition, the experimental limits are the strong dependence of the temperature on the emissivity parameter, the relative slow response time of the camera (about 20 ms), the difficulty in building an ad-hoc setup that can guarantee measurements repeatability.

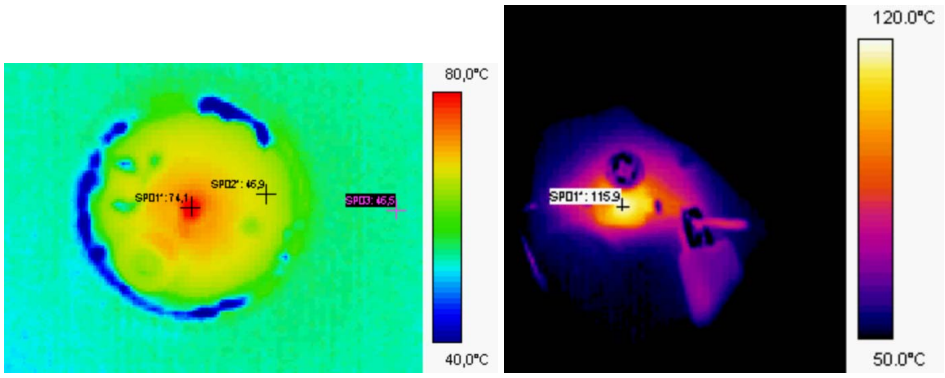


*(a)* TO-18 *(b)* OS Dragon

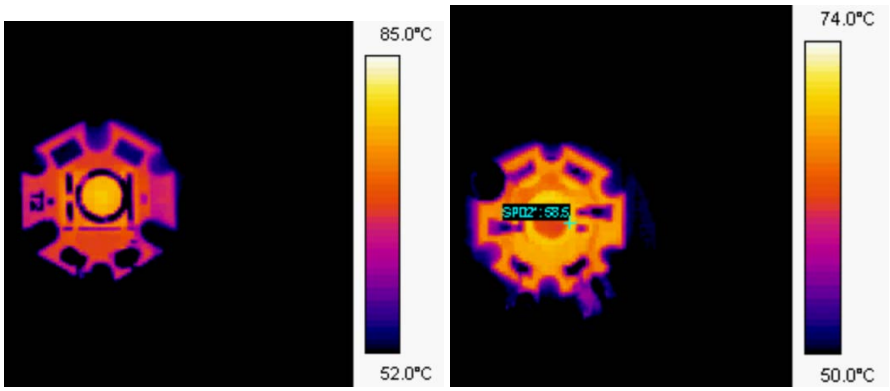


*(c)* CREE *(d)* CREE

*Figure 3.7: Thermal mapping of several device operating at nominal conditions: (a) a low-flux blue LED on TO-18 package, operated at 20mA at RT, (b-d) 1W LEDs with different packages and heat-sinks, in climatic room at* 50 °C*. The images have been taken with a FLIR ThermoVisio A20M IR camera.*

A different approach is represented by **electroluminescence measurements** for temperature extrapolation [56, 52]. In this case, the linearity between the emission wavelength and the temperature is used. The difficult in using this technique is the measurement an accurate EL spectrum in the minor time, in order to avoid self heating: this constrain is often incompatible with available measurements systems.

Finally, several experiments for thermal measurement have been made on LED by means of **micro-Raman Spectroscopy**. The Raman scattering is based on the interaction between incident light and inelastic scatter with crystal. The spectra of the scattered photon depend on the temperature since the phonon it has generated (or annihilated) is temperature-dependent. This technique has a good spatial and time resolution. An application of this measurement technique is reported in Fig. 3.8, where a thermal map of a UV-LED is reported [12].

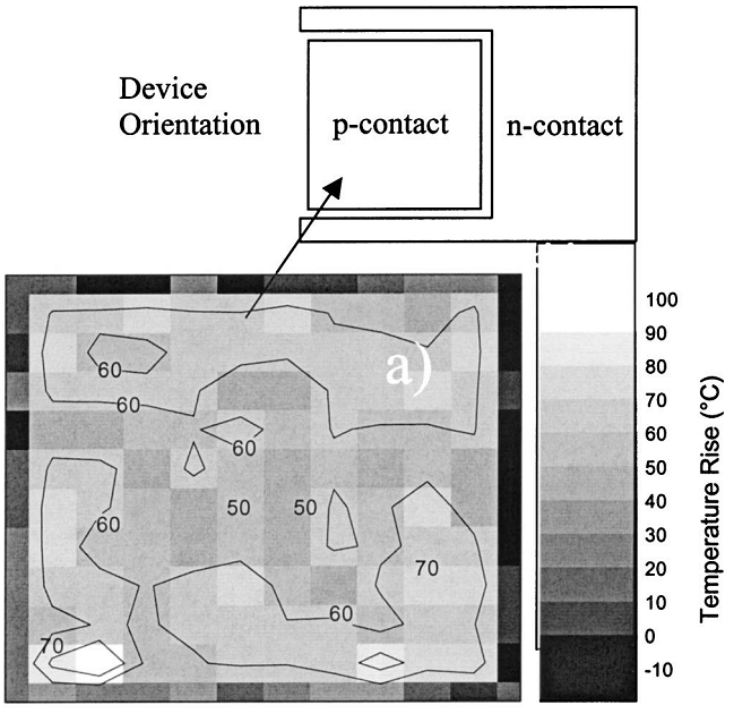


*Figure 3.8: The thermal map of a AlGAN based LED, obtained using micro-Raman spectroscopy [12].*

### 3.2.3 Physically contacting methods

The last category of thermal measurement is represented by physically contact measurements. With physically contact we intend the point contact with the device, obtained with thermocouples or scanning thermal probes, and multiple contacting with liquid crystals and thermographic phosphors. These method permit a high spatial resolution, giving the advantage of obtaining thermal map. On the other hand, these measurements need a surface in order to be applied, and can heavily perturb the measurements itself. Finally, the slow response of probes and liquid crystals avoid the transient temperature evaluation. At the moment, only one work on LED phosphor thermometry has been published [57].

## 3.3 Static characterization: Thermal Resistance

This section will describe the operating principle of the electrical characterization setup for steady-state analysis and the different implementations of these setup designed during the work.

### 3.3.1 Principle

In the previous discussion on thermal measurement techniques, we have mentioned several categories. In particular, the attention was focused on electrical measurement for thermal analysis. Since the LED is a p-n junction, the only electrical method for temperature measurement applied was the forward voltage method (see pag. 30).

As was mentioned before, the method is based on a calibration measurement and the forward voltage measurement at operating conditions. In Fig. 3.9 the procedure for LED junction temperature has been reported. The calibration is performed in a climatic chamber, but LED with short heat-flow path can be calibrated also with a TEC (this is the case of power LEDs). Since the LED is a current-controlled device, a current pulse is applied to the sample and the forward voltage is measured in the shortest time possible. This will avoid the self heating that can invalidate the measurement, giving an underestimation of the junction temperature. The voltage measurement is performed at different temperature levels, usually in the operative range of the device. The procedure is repeated for each current level investigated, since the relationship between voltage and temperature is current-dependent. In Fig. 3.9(a) an example of a calibration (also called thermal map) is reported. As can be noticed, the temperature range investigated is important for a correct temperature estimation. If we make the calibration in a short temperature range (i.e. $35\ ^{\circ}\mathrm{C} < T_j < 75\ ^{\circ}\mathrm{C}$), we could assume that the behaviour is linear and a linear fitting is sufficient for the extrapolation of the $V_f(T_j)$ relationship, also in the higher range. However, if we perform the measurement in a extended range, we will find that the behaviour is exponential. As can be noticed looking to the figure, the difference at high temperature reach about $20\ ^{\circ}\mathrm{C}$, that is an undesirable effect when measuring device with $10\ ^{\circ}\mathrm{C}$ heating at operative conditions. Thus, the exponential approximation must be provided when analyzing LED that will operate at harsh ambient conditions and/or high current levels.

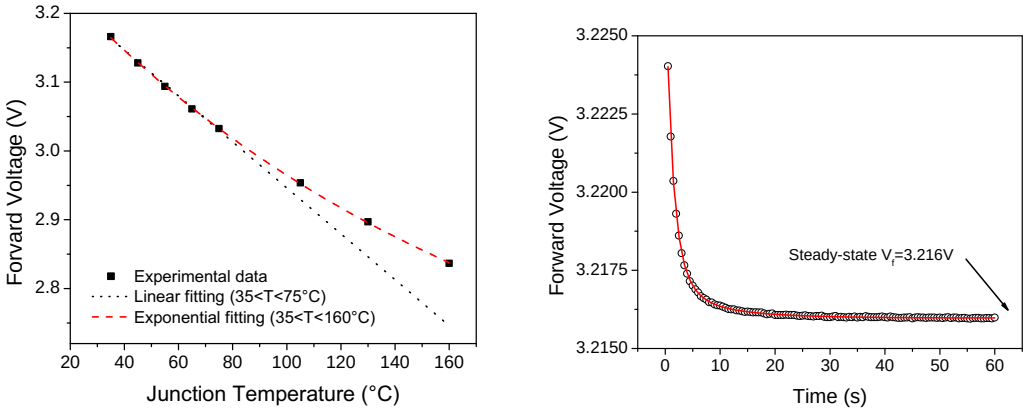


*(a)* *(b)*

*Figure 3.9: The two phases of measurement. (a) the calibration and (b) the measurement at operating conditions, with exponential fitting for extrapolation of voltage at steady-state conditions. In (a) the experimental data have been reported, together with linear fit in low temperature range ant the exponential fitting in the entire range.*

The second step of the junction temperature measurement is a trivial measurement of the forward voltage in operative conditions. In fact, once the $V_f(T_j)$ relationship is available, the temperature estimation can be always performed by simply applying the relationship to measured voltage. This is useful when measuring a device under operative conditions (i.e. including heat removal solutions as heat sinks, funs,...). In Fig. 3.9(b) an example of voltage transient is provided. Since it is not always possible to bias the device for a long time, and the

thermal transient follows an exponential law, the steady-state value can be easily extrapolated by means of fitting.

Once these two measurements are available, it is necessary to invert the $V_f(T_j)$ function and obtain the relationship $T_j(V_f)$. It's worth noticing that this step can be done only in certain cases, like the linear law or the single-$\tau$ exponential law. Inserting the values at steady-state conditions, one obtains the junction temperature at a given input power. Finally, the temperature vs. power values are reported in a plot for thermal resistance calculation. In Fig. 3.10 we have reported an example of plot for thermal resistance calculation. In this case, the linear behaviour permits an easy extrapolation of the thermal resistance, given by the slope of the linear fitting of the data. It is not always possible to obtain a specific value for thermal resistance since it is not proven that the linearity between temperature and power. Several authors reported that the thermal resistance of a LED depends on the ambient temperature and the power level [58, 55, 59]. Thus, it's always better to make accurate junction temperature measurement at operating conditions instead of using the inaccuracy that the thermal resistance parameter may introduce.

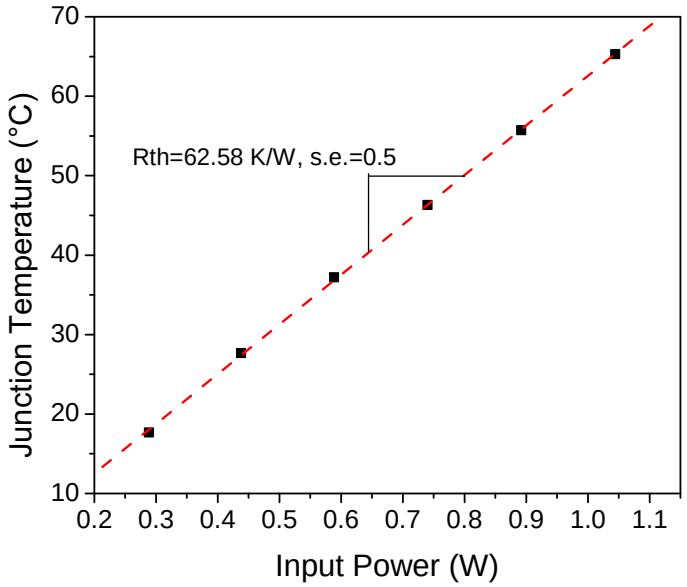


*Figure 3.10: Extrapolation of thermal resistance from the slope of input power vs. Temperature plot. The slope has been calculated by means of linear fitting. The measurements have been performed on a Chip-On-Board power LED without heat-sink.*

The explained technique has a dual method. Since the current pulse for calibration can induce some self-heating, it is also possible to make a calibration at current levels that do not imply a relevant heat generation. In that case, the low current (also called sensing current) can be used monitor the junction temperature simply biasing and measuring the voltage drop. Also the thermal measurement in steady state conditions is different: the device is biased at nominal current and when the thermal transients are terminated (and the junction is in steady-state conditions) the input current is switched from nominal value to the sensing current. The

first voltage value in low bias regime can be converted in temperature with the relationship calculated before. The procedure is well described in [60]. While the problem of fast current pulse is bypassed with low current measurement, the non-trivial electronic system for the fast switching of the currents make the technique equally difficult to implement. The presence of a parasitic electrical transient (due to the presence of an intrinsic electrical capacitance) may perturb the measurement. A solution consists in forcing the voltage to 0 for specific time when the high current is switched off and before is switching to the sensing current. However, it's difficult to fix a time period - not too long for a right temperature estimation, and not too short for for electrical transient removal - and to implement.

### 3.3.2 Experimental solutions

During the work on thermal characterization, several efforts have been spent at finding the best experimental solution for junction temperature measurements based on forward voltage method. The most difficult aim to achieve is a setup able to provide a fast impulse current, that remains stable in the range of $1 \times 10^{-6} - 1 \times 10^{3}$ seconds, at high current levels. The current pulse can be easily implemented by driving with voltage pulses a MOSFET in series to the LED, biased with constant drain current. The problem with this solution is that the current generator encounters problems when the load is not constant. In fact, when the MOS is switched off, the current generator forces its output voltage to compliance value, and when is switched on, it returns to voltage level of the load (the series of the LED and the MOS).

This issue can be overcome by providing a dummy load for the current generator. In order to replicate the load represented by the LED, one can put a similar LED biased by a MOSFET driven in counterphase with respect to the LED under test. In Fig. 3.11 the electrical circuit used for high current pulse generation has been depicted. An input voltage pulse is applied to the MOS driver, that can replicate the signal and its negative. The in-phase signal drive the gate of the MOSFET, switching on the device. In that case the MOSFET of LED2 is off. When the input goes down, the LED1 is switched off while the LED2 is turned on. In such way the current generator does not suffer of load modifications. There's also a second feature. With a little unbalancing of the load (acting on the potentiometer $R_2$) it is possible to insert a small current overshoot to LED: in this way the parasitic electrical capacitance is charged in less time, reducing the electrical transient that can introduces some inaccuracy in the measure. Finally, third MOS has been inserted with the aim of providing a constant voltage value when the LED1 is turned off. This will help the generator when the LED will be turned on since the capacitance of the LED is pre-charged. The voltage drop on the LED is measured by a digital oscilloscope, that permits to collect high resolution data with high time resolution too.

The circuit described can perform very accurate voltage measurement in different time ranges. This is useful for thermal transient measurement that will be described afterwards. We may infer that this system is not plug-and-play, since it needs several external instruments to work (voltage sources, waveform generator, oscilloscope and probes) and must be accurately calibrated (the dummy load, the potentiometers). When we have large amount of samples to measure (especially in reliability works), the time needed for measurement must be minimized, and this setup is not adequate. However, we may use the results from accurate analysis and

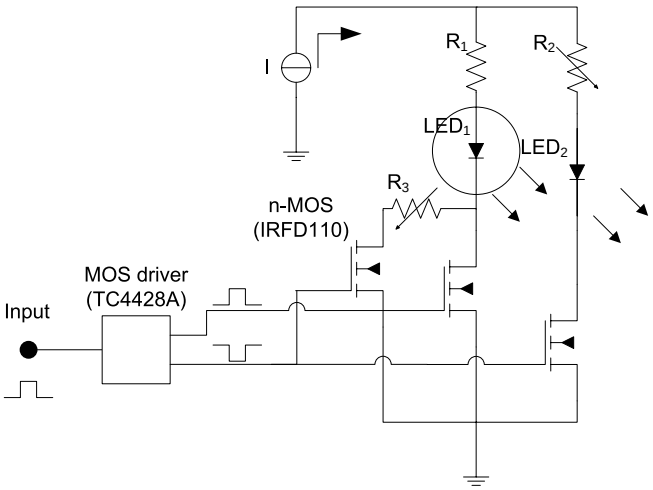


*Figure 3.11: The electrical schematic of the circuit used for current pulse generation. LED1 is the LED under test, while LED2 is the dummy one.*

compare these results with time-saving measurement, that can be performed with ordinary parameter analyzers available in testing labs. During the calibration, since the thermal transient before the thermal measurement is usually negligible, a slow pulsing obtained with parameter analyzer may not impact on the final temperature estimation.

In order to understand the impact of a slow-pulse thermal calibration, a thermal calibration has been obtained with the aforementioned circuit in a wide time range. In Fig. 3.12(a) the voltage transients measured at different temperature levels ($35 - 85\ ^{\circ}\mathrm{C}$) biasing a power device at $350\ \mathrm{mA}$ have been reported. As can be noticed, different time constants can be found, but the shape of the plots remains the same for the different temperature levels. If we integrate the voltage at different times during the transient, we will obtain thermal maps for each time step (as an example, look to the inset graph in Fig. 3.12(b)). Finally, we may use the obtained thermal coefficients in order to calculate the junction temperature at steady-state conditions. The plot of the temperature vs. the delay time of integration has been reported in Fig. 3.12(b). It's worth noticing that the impact of the pulse length on the final temperature estimation is not so strong: the error in temperature estimation obtained with pulse lengths below the $100\ \mu\mathrm{s}$ is negligible. This experiment demonstrate that for this kind of LED structure it is possible to obtain accurate temperature measurements also with programmable test instruments. However, this comparison must be performed each time we measure a device with different structure, since the thermal transient behaviour is strongly correlated to the structure (see the following section).

The experimental setup for thermal resistance measurement must take into account the modifications of the thermal impedance properties induced by instruments. The steady-state measurement must be performed in ambient conditions closest to the device operative conditions. An example of the impact of the measurement setup on temperature estimation has been reported in Fig. 3.13. Here the temperature vs. input power plots of the same device have been depicted. The device was a low-flux LED on TO-18 package, not optimized for heat removal.

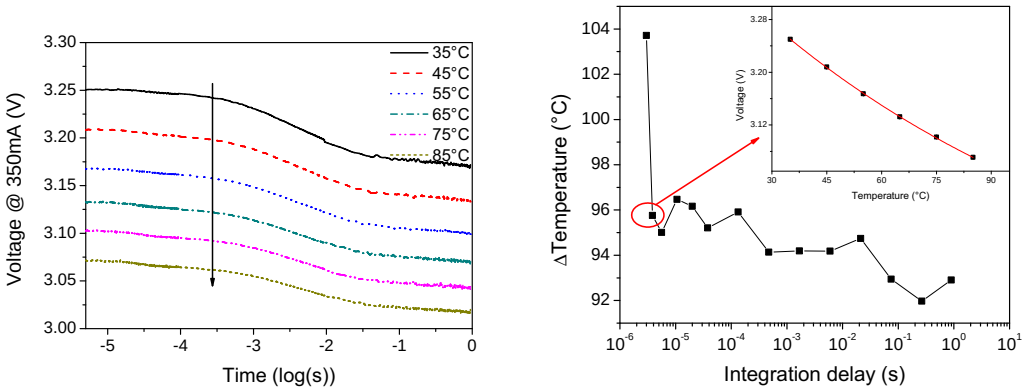


*(a)* *(b)*

*Figure 3.12: The analysis of $V_f$ calibration at different integration times. In (a) the voltage transients vs time for a power LED at different ambient temperature have been reported. The voltage value has been integrated at different times and the temperature increase of the LED calculated for the different times have been reported in (b). In the inset an explicative thermal map has been reported. Excluding the first value that includes the electrical transient artifacts, we can state that the delay in voltage measurement does not impact on the accuracy of the temperature measurement.*

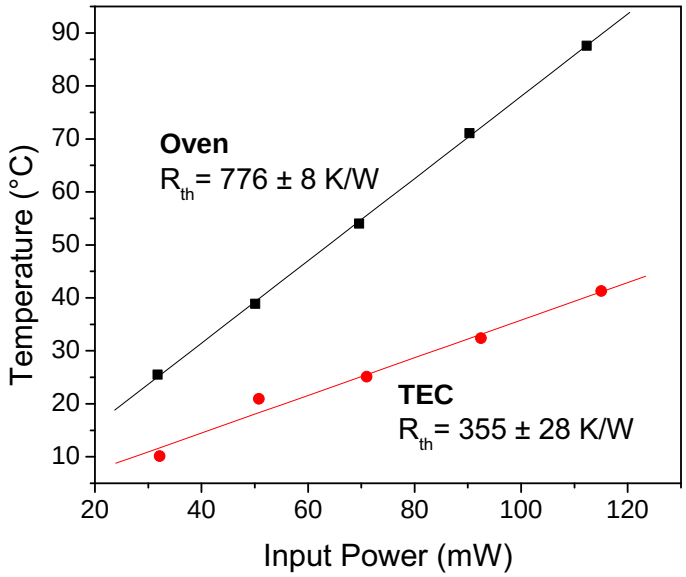


*Figure 3.13: Comparison between thermal resistance measurements of the same LED placed in the climatic chamber without forced convection (oven) and on a Peltier cell (TEC). In order to avoid the underestimation of the thermal resistance, the setup used for steady-state measurement must be appropriate for the different device structure.*

While the calibration measurement used was the same, the measurement at steady-state conditions has been measured in a climatic chamber without forced convection (squares), and on a copper TEC (circles). The thermal resistance measured in climatic chamber was found to around $776\ \mathrm{K/W}$, while the LED mounted on the TEC showed a thermal resistance of about $355\ \mathrm{K/W}$. This evident difference in thermal resistance value can be explained considering the equivalent electrical model for thermal resistance. The LED in the oven present a thermal resistance between junction and the package, and a series resistance between the package and the ambient. When the LED is placed on the TEC, the package is forced to ambient temperature and the thermal resistance between package and ambient is shortened. Thus, the overall thermal resistance measured on a TEC is about half of the value measured in air. Since the doubling of the thermal resistance may have a strong impact on reliability of the device, it's important to measure the junction temperature under operative conditions, as has be done for reliability testing described in next chapters.

## 3.4 Dynamic characterization: Thermal Transients

This section will provide some results on dynamic thermal characterization on power LEDs. After explaining the experimental setup implemented, a few examples of self heating transients and structure functions calculation will be provided.

### 3.4.1 Experimental solutions

Different experimental setup have been implemented in order to obtain current pulse with:

1. rise time < $10\ \mu\mathrm{s}$
2. pulse width with infinite duration (step)
3. current stability in a wide current range
4. high accuracy in the voltage measurement

Two experimental solutions that resolve these issues have been implemented.

The first has been used for power LED and has been already described in the latter section (Fig. 3.11). The circuit permits to have a fast switch on current pulse with high level in $50\ \mathrm{mA}$ - $1\ \mathrm{A}$ range. The transient is collected by means of a digital oscilloscope, with increasing acquisition time, from $100\ \mu\mathrm{s}$ to $100\ \mathrm{s}$. After the single parts of the transient have been collected, they are filtered and tied, in order to obtain a single self heating transient.

The second solution is very similar to the latter described, but it was implemented with a low power perspective, with current levels ranging from few $\mathrm{mA}$ to $100\ \mathrm{mA}$. The same philosophy of two equal loads has been used. However, the switching with MOS was not possible for fast switching times, and a integrated analog switch Single Pole, Double Through (SPDT) has been used, the DG419 chip.

Despite both solutions provided interesting results, the thermal analysis in dynamic conditions has been carried out mainly on power devices, since the issues caused by self heating are more important.

### 3.4.2 Results and analysis

Some thermal transients collected with the experimental setup previously described have been reported in Fig. 3.14. In Fig. 3.14(a) the transients for Chip-On-Board power LEDs with different structures have been compared. In particular, the measurements have been performed on LEDs with the encapsulation and phosphors (white LEDs), with only the encapsulation (blue LEDs) and without anything (bare chips). In this case there's no a relevant correlation between the transient behaviour and the structure, since the polymeric encapsulation presents a low thermal conductivity and can be compared to air. However, an higher self heating can be detected for white LED, due to the presence of the phosphors: the down-conversion of the wavelength give a contribution to heat generated, implying a higher temperature. It's worth noticing that the presence of the phosphors only influences the longer transient, while the transient related to the chip remain unchanged.

In Fig. 3.14(b) the self heating transients for a different power LED structure. In this case, two different approaches for heat removal at package level have been implemented. The measures revealed that one solution permits the halving of junction temperature. Also in this case, the thermal transient underlines that the improvement in terms of heat removal is located at the package level (the longer transient), while the characteristic of the first interface chip-package is not affected by the modification (the first transient).

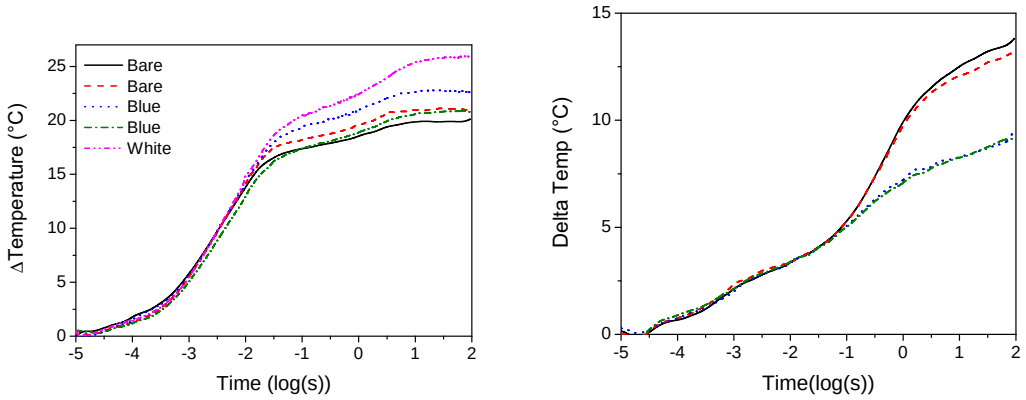


(a) (b)

*Figure 3.14: Some self heating transients for LEDs with different structure. In (a) the thermal transients for a Chip-On-Board LED with phosphors and lens (white), with lens (blue) and the bare chip (bare) are reported. In (b) the transient of the same LED package but with two different heat removal configuration are depicted.*

Since one of the main goals of this thesis is the analysis of the reliability of optoelectronic devices, the thermal properties have been used to investigate the impact of the stress on the lifetime of the devices. In order to analyze the dynamic thermal properties during ageing, analytic tools like structure functions have been used (see pag. 26 for details). As an example, the analysis on the impact of the electrical and thermal ageing on power LEDs lifetime has been provided [15, 16].

In Fig. 3.15 has been reported the evaluated differential structure functions for one repre-

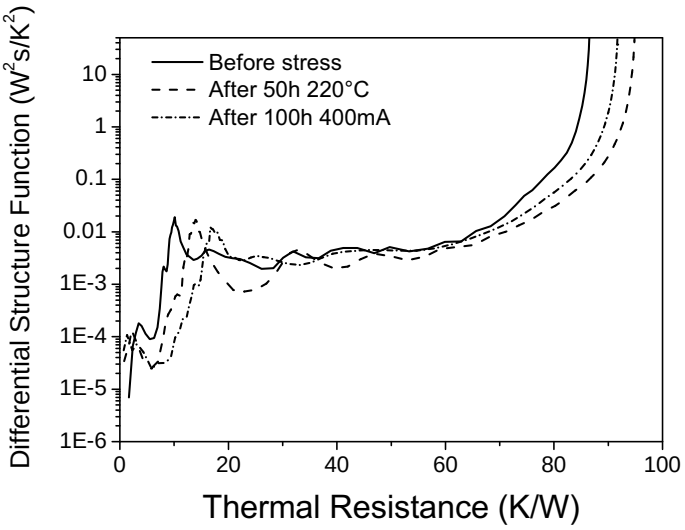


*Figure 3.15: The differential structure function for untreated power LED is compared to LEDs aged at* $400\ \mathrm{mA}$ *for 100 hours and* $220\ ^{\circ}\mathrm{C}$ *for 50 hours. The stress induced an increase in thermal resistance at the chip-package interface [16].*

sentative untreated device and two devices aged at $220\ ^{\circ}\mathrm{C}$ for 50 hours and at $400\ \mathrm{mA}$ for 100 hours. From this figure we can extrapolate various information. First, each peak corresponds to a interface or a variation in cross section area along heat-flow path. Thus, the solid line in Fig. 3.15 shows two evident peaks at $3.5\ \mathrm{K/W}$ and $10\ \mathrm{K/W}$. The first one represents the thermal resistance from junction to chip, while the second is the thermal resistance between junction and the copper frame of the package. The total amount of thermal resistance between junction and ambient is given by vertical asymptote, where the structure function goes to infinite, and is equivalent to $87\ \mathrm{K/W}$. This thermal resistance value is so high due to low thermal conductivity of the small copper frame to the ambient. For comparison, we reported in the plot the differential structure functions of aged devices. We noticed that the main variations in behaviour were concentrated in the region near the junction. While the peak corresponding to junction-chip thermal resistance remained almost unchanged for aged devices, the peak corresponding to copper case slightly moved towards higher resistance values for aged devices: $14\ \mathrm{K/W}$ for $220\ ^{\circ}\mathrm{C}$ condition and $17\ \mathrm{K/W}$ for device aged at $400\ \mathrm{mA}$.

This fact can be explained as a degradation of thermal contact between chip and package, i.e. the die attach, due to high temperatures reached by the junction. This effect was earlier reported in [20] and the increase of thermal resistance was ascribed to delamination of the die attach. The rise of thermal resistance, together with the forward voltage increase detected, could have negative impact on reliability of device, since the junction temperature is equal to $T_j = P_{diss} * R_{th}$.

This example reveals the utility of the structure functions tool. The measurement of the self heating transient can give information on the localization of thermal resistance modification. This is very useful in the development of a product, since it permits to discriminate the weak points of a device or material and how to improve the performances and the reliability.

## 3.5 Thermal Simulation

This final section reports the results of FEM simulation, both in steady-state and transient conditions. The simulation on LEDs was carried out aiming at finding a model for the thermal properties that can be related to experimental results, and at correlating the LED structure with the thermal management. After a brief explanation of the Finite Element Modeling used in this work, a few preliminary results in static and dynamic conditions will be provided.

### 3.5.1 Finite Element Modeling

In previous sections a method for thermal analysis has been provided, based on the parallel between thermal and electrical resistance. This model can be lumped or distributed: when complex configurations are present, it is possible to solve the net of thermal resistances and heat capacitance by simulation. However, this method is limited, since it's not possible to accurately define the thermal-dependent properties as heat capacity or thermal conductivity, and a good modeling requires many efforts.

An alternative approach for an accurate thermal simulation is represented by the Finite Element Modeling. Nowadays, there are tens of software that permit to solve the differential equations of heat transfer. In addition, the FEM analysis provides accurate results on thermal properties at steady-state and dynamic conditions without a preliminary modeling. Finally, since the thermal properties of the materials that usually compose a LED are available in the literature, this approach was widely adopted by the scientific community [61].

The FEM simulator used for thermal analysis of LED was ANSYS, a structural simulator that implements the heat transfer equations. In the case of the LED simulation, the equations used were the conduction and convection laws, since the irradiation does not impact on the thermal properties. We used a 2D approach were we found a symmetry, cause a 3D analysis would be more time consuming and without improving the accuracy of the results.

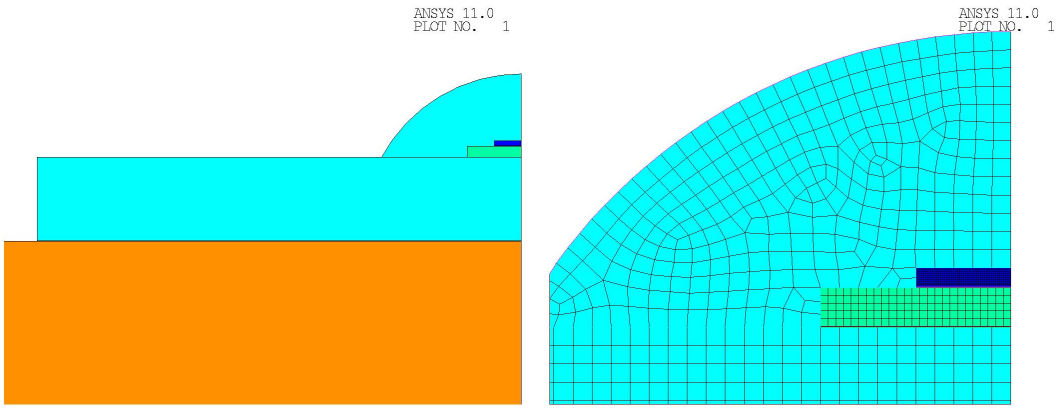


(a) (b)

*Figure 3.16: The 2D model used for thermal simulation of COB white LED configuration. In (a) the schematic used for the simulation has been represented: the orange indicates the aluminum heat sink (truncated), above which the PCB board of the LED is attached; the green area is the socket, with the GaN/SiC chip placed above (blue). in (b) the particular of the chip area is represented, together with the mesh.*

In order to compare the experimental results on thermal properties and to validate the theoretical model, the modeling has been carried out on Chip-On-Board white LEDs. Some results on thermal measurements for these LEDs have been reported in this chapter. The basic structure for these LEDs include (bottom to up):

1. an aluminum heat sink, with an ambient temperature load on the bottom surface
2. the aluminum board where the LED in attached
3. the die attach
4. the socket
5. the die attach
6. the LED in flip-chip configuration, composed by GaN (active region, where the heat is generated) and by SiC (the substrate, on the top)
7. a polymeric encapsulation, that acts as a lens.

In addition to constant temperature and heat generation loads, a natural convection has been applied on the free surfaces. The material properties have been collected in the literature [62], Between each material a thermal contact has been created with a high thermal conductivity. In Fig. 3.16 the 2D model used for simulation has been reported. As can be noticed from Fig. 3.16(b), the mesh size was adapted to the area to be meshed, in order to optimize the solution time and the results accuracy.

### 3.5.2 Static analysis

The first step of simulation was the solution in steady-state conditions. This analysis was carried out with the aim of finding a correlation between experimental and simulation results.

The Fig. 3.17 reports the results from static analysis on COB LEDs with and without the encapsulation. The heat generated by the active area was $1\ \mathrm{W}$, i.e. the heat generated by a power LED biased at nominal conditions ($350\ \mathrm{mA}$. While in the case of LED without the encapsulation the junction temperature reached about $12.6\ ^{\circ}\mathrm{C}$ (Fig. 3.17(b)), the LED with encapsulation presented a lower value of about $11.5\ ^{\circ}\mathrm{C}$ (Fig. 3.17(d)), roughly a degree below. This difference is caused by the alternative heat removal path offered by the encapsulation: even if the thermal conductivity of the polymer is low, it is still higher than the thermal conductivity offered by the chip-ambient interface. On the other hand, also the encapsulation suffers of a high self heating: this heat was the cause of lens browning seen for first generation epoxy used for encapsulation [15].

Concerning the comparison between experimental and simulation results, the junction temperature, measured in LEDs was roughly double than the simulated temperature. This discrepancy could be explained by (i) a difference between real and theoretical thermal properties and material sizes, and/or (ii) a not consistent 2D modeling, or (iii) the not-ideal thermal properties of the contacts between different materials.

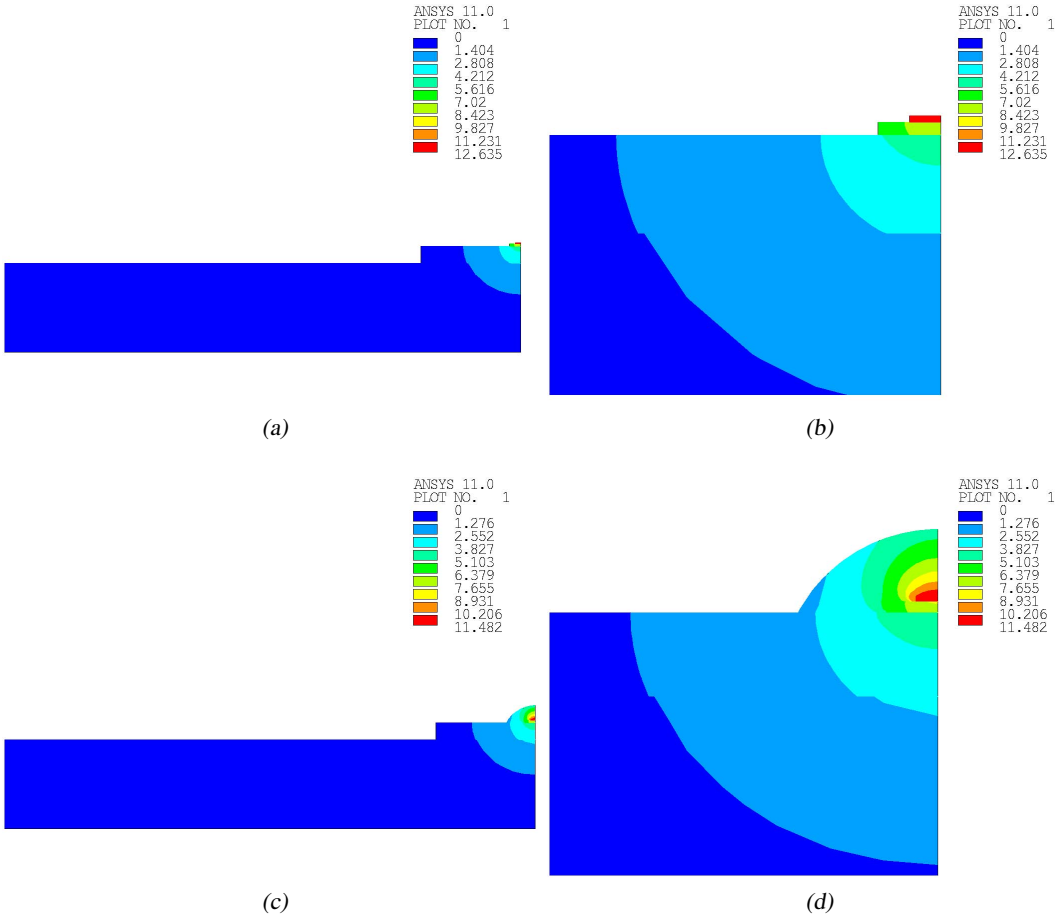


*Figure 3.17: The contour plots of the temperature for different chip configurations in steady-state conditions: (a)-(b) report the LED without the encapsulation (with the magnification), while (c)-(d) include the polymeric lens (with the magnification too). Despite the thermal conductivity of the encapsulation is low, it helps to dissipate the heat generated by the chip.*

### 3.5.3 Transient analysis

The same geometry and model of COB LED described above have been used to solve the heat transfer equations in transient conditions. The simulation was carried out at logarithmic steps in order to compare the results to the self heating transients measured on LEDs (see pag. 26).

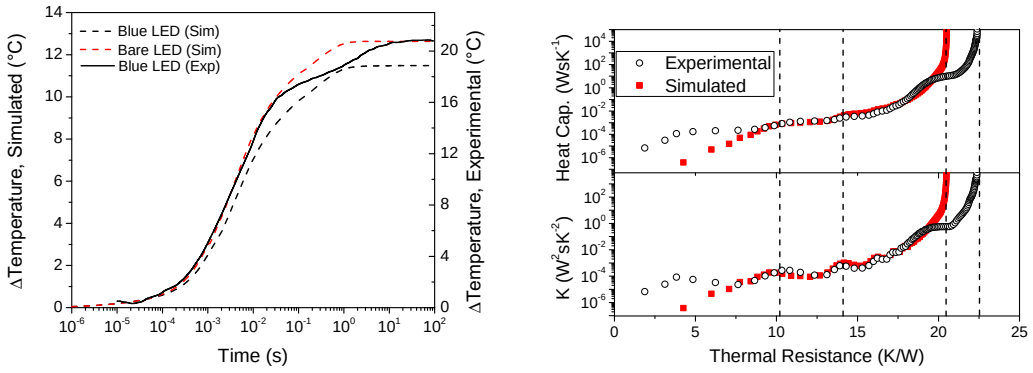


*(a)* *(b)*

*Figure 3.18: The comparison between experimental and simulation results of thermal characterization in dynamic conditions has been reported. The plot of the self heating has been reported in (a): notice that a part from the scale factor, the transients are quite similar. Adjusting the scale factor, it was possible to evaluate and compare the structure functions for experimental and simulated thermal results (b).*

In Fig. 3.18(a) an example of self heating transient obtained by simulation has been reported. The figure reports the plots of transients simulated on LED with (blue) and without encapsulation (bare). A few comments can be addressed. As can be noticed looking to the figure, the transients are equal for $t < 100$ µs, then the bare LED suffer from a higher self heating with respect to blue LED. This different behaviour was previously described and implied to the absence of the polymeric encapsulation. However, the further interface LED-encapsulation cannot be directly observed in the transient as a new time constant. An in-depth analysis on the differences can be provided by the structure functions (not reported here).

In the same figure the plot of a measured self heating transient has been reported for comparison. As can be noticed, the transients are quite different, in terms of scale factor and for the time constant between $20$ ms and $10$ s. While the first difference has been already motivated, a few words can comment the different time constants. The model for the simulation uses a heat sink with a constant temperature on the bottom. The same situation was not recreated for the experimental setup: in that case the LED was attached to a heat sink without forcing the temperature, with the only presence of natural convection. Since the situations are quite different, also the time constant related to the interface between heat sink and the ambient are quite different.

This fact can be clearly identified in Fig. 3.18(b), where the structure functions of a simulated and experimental transient are compared. Please notice that the thermal resistance values have been rescaled in order to better compare the plots. As can be noticed, the differential structure function of the experimental transient exhibits a further peak around $18$ K/W. That

peak is related to the interface between the heat sink and the ambient under natural convection condition. From the figure it can also be noticed that the structure function of the experimental measurement presents a peak around $4\ \mathrm{K/W}$: since the simulation take into account all the interfaces present in the LED, it is possible that the measured peak is related to electrical transient intrinsic to the measurement.

In conclusion, the FEM simulation was found to be a useful tool for thermal behaviour analysis of LEDs, especially for the relationship between the structure and junction temperature: once validated the model comparing results to experimental measurements, it can have a great employment in product development and reliability analysis.

## 3.6 Conclusions

In this chapter an dissertation on thermal properties of LEDs, their measurement and their analysis has been provided. In particular, the work on thermal analysis provided several results:

1. among the different thermal characterization techniques, the method based on forward voltage method was identified as the more simple to implement and capable of accurate results;

2. several experimental setups for junction temperature measurement have been implemented, depending on the ambient conditions available;

3. the theoretical model used for FEM simulation was in good agreement with the experimental results;

4. the analysis of thermal properties can give important result to failure analysis and reliability design.

The experimental setup designed and the FEM implemented during this work are a good starting point for an in-depth analysis of thermal properties of new generation optoelectronic devices.

# Chapter 4

# Lifetime prediction of Phosphor Converted LEDs

*An experimental approach for Accelerated Lifetime Testing of low-flux white LEDs is presented. The related analysis on degradation and failure modes is provided. The chapter reports also different statistical tools to be used in reliability analysis. The application of these tools permitted the extrapolation of a degradation model used for lifetime estimation.*

## 4.1 Outline and specific goals

In this chapter a reliability analysis on low flux Phosphor Converted LEDs (PC-LEDs) for display application is reported. The analysis has been performed by means of an accelerated life testing framework on selected devices from different commercial manufacturer. Literature offers several works on reliability of low-flux InGaN based LEDs. Furthermore, during the last years several efforts have been spent in getting information on lifetime evaluation of High Brightness LEDs. However, a few authors reported the effects of ageing on low flux PC-LEDs related to the package, with a correlation between lumen decay and chromatic properties modification. The main aim of this work is thus the analysis of the impact of the device composition and structure on lifetime and the investigation on the best trade-off between performances and reliability. The work has been organized in subsequent steps:

1. an in-depth characterization of optical, electrical and thermal properties with a statistical perspective;
2. the design and implementation of the accelerated life testing framework (stress conditions, time-line, number of devices, parameters to monitor, etc.);
3. the Failure Analysis by means of several imaging techniques on dead devices;
4. the investigation of degradation mechanism involved in the lumen decay process.

**Specific goals** The present work aimed at:

1. comparing different technologies and materials used in the state of the art LEDs and investigating their impact on performances of devices;
2. evaluating and implementing specific techniques for lifetime analysis, based on available reliability data provided by the manufacturer;
3. finding any correlation between device parameters (optical-electrical-thermal) in order to monitor the degradation and give a feedback to the control system;
4. extrapolating accurate degradation model by means of statistical methods applied to reliability, that can provide a lifetime prediction for operative conditions;
5. identifying the degradation mechanisms that limit the lifetime of LEDs and the physical processes involved in the failures;
6. experimenting novel failure analysis techniques not yet employed in LED reliability.

## 4.2 Device structure and characteristics

In order to fulfill the goals of the work, two families of different commercial available PC-LEDs have been chosen, namely "Set A" and "Set B". The two series of LEDs are based on different chip structure and phosphors composition, but are housed in similar package (P-LCC-4, 2X3 $\mathrm{mm}^2$). A schematic of the package used is reported in 4.1.

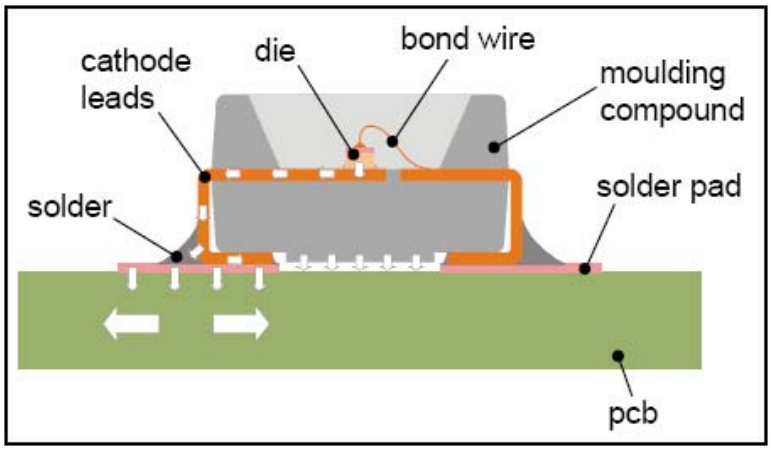


*Figure 4.1: Schematic of the package used in this work (from [63]). Heat flow path is indicated by arrows: it starts from the chip, goes thought the cathode leads and continues into the solder above the PCB. This package is not designed for high power devices since the thermal interfaces present low thermal conductivity.*

Although the two families are different, the chips are both based on GaN/InGaN semiconductor, since the emitting wavelength is the same (blue). Since the samples have been collected from commercial distributors, we did not have any information on the structure and composition of devices. In the following the reverse engineering and characterization steps will be reported, together with results obtained from the analysis and the comparison of the devices.

### 4.2.1 SEM analysis

As mentioned in [19, 15], the chip structure could play an important role in the degradation of opto-electronic devices and main efforts are spent in LEDs aiming at finding the best trade-off between reliability and performances. For this reasons, the reliability analysis reported in this chapter started from the microscopical analysis of two different chip structures. The analysis was carried out in collaboration with the Department of Electrical Engineering of the University of Cagliari, that have the proper know-how for package de-processing and the facility for microscope imaging and EDAX analysis. The main aims of the analysis were the identification of:

- the chip structure (impact on the electrical behaviour)
- the chip dimensions (impact on the light output)
- the surface composition (impact on the light output)
- the die attach design (impact on the thermal management).

The plastic package of two LEDs from Set A and Set B have been submitted to chemical etching (solvent) in order to remove the encapsulation containing the phosphors, the bonding wires have been removed and the chip was detached from the package. Afterward, the samples were inserted in a SEM system for imaging. Images have been collected both with secondary electrons (SE) and backscattered electrons (BE).

In Fig. 4.2(a) and 4.2(b) the SEM images of Set A LED are reported, taken from lateral and top side respectively. The LED of Set A exhibits a Truncated Inverted Pyramid (TIP) structure. In this structure, the side walls of the chip are etched with a particular angle, in order to reduce the internal reflections caused by the high reflection number of GaN based materials [64]. The electrical pads are placed on the top (p-side contact) and on the bottom (n-side contact): this structure is based on SiC substrate and presents a vertical conduction path. The active region of this LED is a few micrometers from the surface. The side length is about $300\ \mu\mathrm{m}$, with a chip area of about $9 \times 10^{-4}\ \mathrm{cm}^2$. The top contact exhibits 4 fingers that spread the current on the surface.

The Fig. 4.2(c) and 4.2(d) reports the SEM imaging of one LED from Set B. The structure of this device is completely different from the one of Set A. In this case the two pads are placed on the surface and the electric path is along the surface. This structure is based on insulating substrate, that in the case of GaN active region could be sapphire or GaN itself. The other difference of the structure of this LED with respect to Set A sample is the thickness. The LED of Set B is thinner than the Set A. This is a different and more efficient design approach that aims at reducing internal reflections and improving the light extraction [1]. The surface dimensions are different too, with a side length of about $350\ \mu\mathrm{m}$ (area of $1.225 \times 10^{-3}\ \mathrm{cm}^2$).

The other relevant difference between the two structures is the thermal contact between the chip and the package. In the case of Set A, the thermal contact coincides with the electrical contact (SiC has a good thermal conductivity), while for Set B the contact is the sapphire substrate, with a larger area for the heat flow.

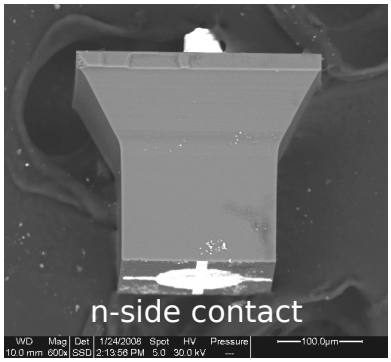


(a)

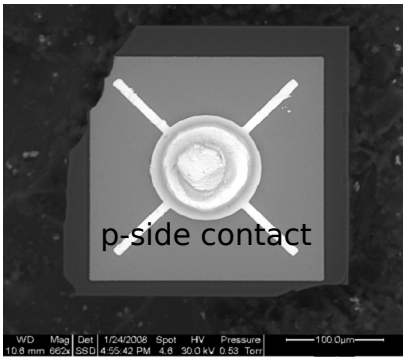


(b)

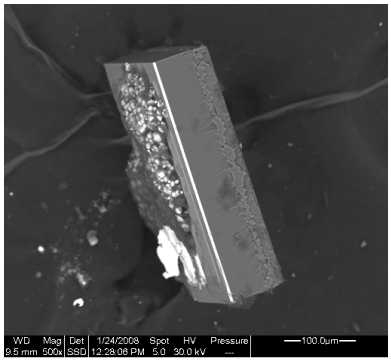

(c)

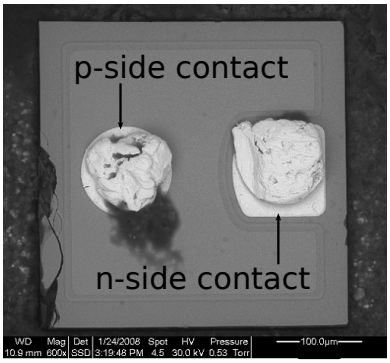


(d)

*Figure 4.2: SEM images of (a)–(b) one LED from Set A and (c)–(d) one LED from Set B.*

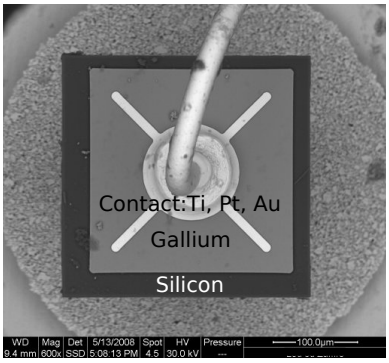


(a)

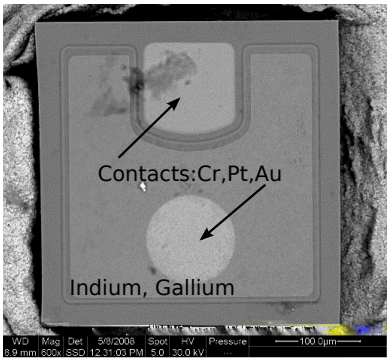


(b)

*Figure 4.3: Punctual EDAX analysis on representative LEDs from (a) Set A and (b) Set B.*

With the same SEM facility we were able to perform an Energy Dispersive X-Ray spectroscopy (EDX) in order to obtain information on surface composition of the LEDs. Main results from EDX have been reported in Fig. 4.3 for LED from (a) Set A and (b) Set B. Concerning Set A, we found the presence of silicon in the outer area (substrate, SiC), gallium in the active region (GaN) and contact based on a titanium, platinum and gold alloy. In Set B LED we found similar results that confirmed our hypothesis: the presence of indium and gallium on the surface (GaN/InGaN active region) and contact based on chromium, platinum and gold alloy. The analysis have been carried out also on the bottom of the LED of Set B (not reported here) and silicon and aluminum have been found, indicating the presence of sapphire substrate ($Al_2O_3$).

### 4.2.2 Optical characteristics

A set of 10 samples from each families has been submitted to optical characterization. The techniques employed to characterize the samples have been used during ageing. The optical characterization is based on Radiant Power measurements at different current levels and Electro-Luminescence spectra at $30\ \mathrm{mA}$ and $50\ \mathrm{mA}$ current levels.

**Radiant Power vs. Current (L-I)** The measurements have been performed by means of the semiconductor parameter analyzer HP4155 coupled with a silicon 818-UV photo-detector (spectral response $200 - 1100\ \mathrm{nm}$). The high-precision time sequencing of the HP4155 permitted to synchronize the biasing of the LED and the voltage measurement on the photo-diode. The voltage was measured $2\ \mathrm{ms}$ after the bias was applied. This system permitted to obtain measurements in a wide range of currents in short time and, most of all, avoids the self heating of the samples that could underestimate the output power. In this technique, the absolute value of the measurement is missing (i.e. radiant power). However, the reliability work is focused on the relative variation of parameters.

In order to obtain repeatable optical measurements, several aluminum samples holder has been designed. Each sample holder can accommodate 8 samples (mounted on ad-hoc PCB) for the ageing. Above the samples, the integrating sphere for optical measurements fits the hole with a low tolerance.

The plots of Radiant flux vs. current of several samples for both families have been reported in Fig. 4.4. As can be noticed, LEDs from Set B emit as twice as LEDs from Set A. This fact could be ascribed to the high quality of lattice and the thickness of chip from Set B. It has been proved that a thinner layer, coupled with roughened surface, permits a better light extraction due to the limitation of internal reflections and substrate absorption [1, 29]. This measurement technique is useful for evaluating the amount of output degradation at different current levels.

**Electro-Luminescence Spectra (EL)** The measurements have been carried out by means of Ocean Optics USB4000 spectrometer ($200 - 1100\ \mathrm{nm}$), equipped with a 2 inches FOIS-1 integrating sphere. A measurement setup similar to the previous one has been used for LED biasing, together with the triggering setup of the spectrometer. In this case, the spectrometer has been calibrated in the operating range and the results are reported in $\mu\mathrm{W}/\mathrm{nm}$.

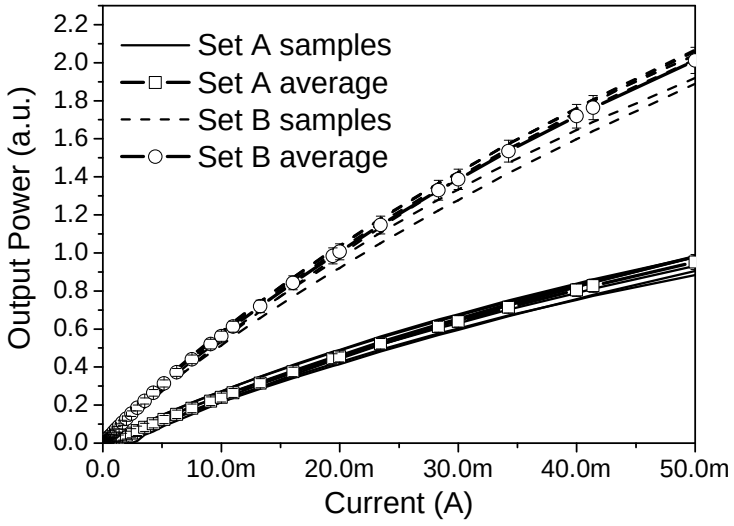


*Figure 4.4: Radiant flux vs. Current plots for several samples from Set A and Set B. In the figure the average values and the standard deviation have been reported.*

In Fig. 4.5 the EL of samples from (a) Set A and (b) Set B and measured at $30\ \mathrm{mA}$ has been reported. Looking to the figure it's clear that the spectral response of the yellow phosphors is different between the two families, indicating a different phosphors composition and deposition process. In addition, in the inset graphs are reported the zoom around the blue peak. As can be noticed, the blue wavelength is more scattered for LEDs from Set A. This instability could plays a negative role with repsoect to yellow conversion, as the phosphors are sensible to excitation wavelength. The data obtained from EL measurements could be processed in order to extrapolate several photometric parameters (lumen) and chromatic parameters as the Color Rendering Index (CRI), x and y CIE values, the Correlated Color Temperature (CCT).

In Tab. 4.1 the average values of lumen flux calculated from EL spectra of Fig. 4.5 has been reported. Concerning the chromatic parameters, the CRI values are about 80 for Set A LEDs and 69 for Set B LEDs. Although the LEDs from Set B have a enhanced luminous efficacy, the reduced CRI indicate a colder light than the high-CRI of Set A. In the ageing section, further explanations for chromatic analysis from EL spectra will be provided, in terms of x and y CIE values and the ratio between blue and yellow peak.

*Table 4.1: Luminous Flux average values for Set A and Set B LEDs*

| Current ($\mathrm{mA}$) | Set A flux (lm) | Set B flux (lm) |
|---|---|---|
| $30\ \mathrm{mA}$ | $1.79 \pm 0.1$ | $4.57 \pm 0.63$ |
| $50\ \mathrm{mA}$ | $2.64 \pm 0.15$ | $6.27 \pm 0.28$ |

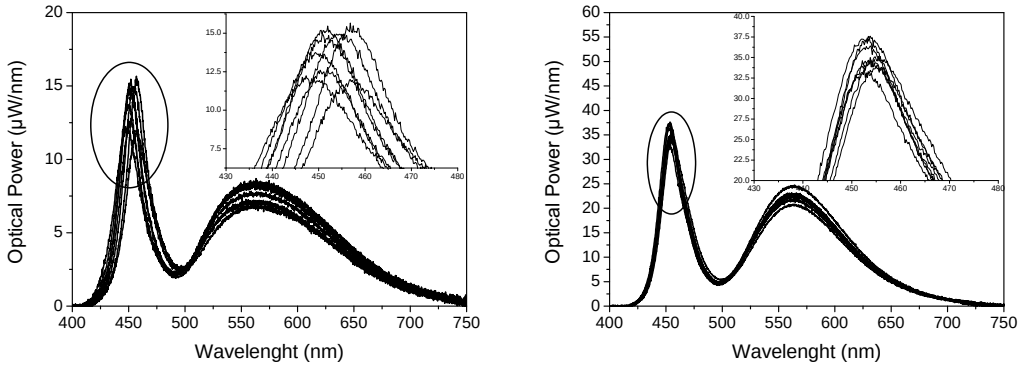


(a) (b)

Figure 4.5: Electro-Luminescence spectra of several samples from (a) Set A and (b) Set B.

### 4.2.3 Electrical characteristics

A set of 10 samples from each families has been submitted to electrical characterization. The characterization consisted of Current vs. Voltage measurements (I-V) and Capacitance vs. Voltage measurements (C-V).

**Current vs. Voltage (I-V)** The measurements have been performed by means of the Sense Meas. Unit Keithley 2612 and the HP4155, for forward and reverse voltage measurements respectively. The 2612 has been employed in pulsed regime (100 µs pulse width) in order to avoid self heating of devices. Furthermore, the 4-wire configuration was used with the aim of obtaining repeatable measurements not influenced by the parasitic impedance of wires. On the other hand, the 4155 performs DC voltage sweep and its high resolution permits low current sensing, useful when measuring in the reverse voltage range.

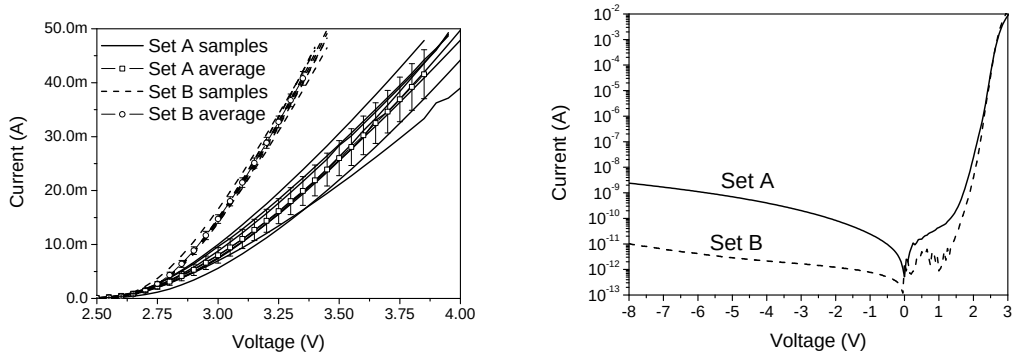


(a) (b)

Figure 4.6: Current vs. Voltage measurements of several samples from Set A and Set B. In (a) the data and the average values in the forward voltage range are reported, while in (b) two representative measurements in the reverse voltage range are plotted.

In Fig. 4.6(a) the I-V measurements of different samples have been reported together with the average values and the standard deviations. As can be noticed, the I-V characteristics of Set A and B LEDs are very different in terms of (i) voltage level and (ii) and scattering. While the Set A samples exhibit scatter data and a mean voltage level of $3.6$ V at $30$ mA, the Set B LEDs have a lower standard deviation and a mean voltage value of $3.2$ V at $30$ mA.

In Fig. 4.6(b) the I-V measurements on representative samples have been reported and plotted in semi-log scale. From the plot we can extrapolate information on reverse current. We can observe that the reverse current of Set A LEDs is higher than Set B, a possible indicator of a higher defects concentration. Low reverse current indicates good electrical properties of the material, and samples that exhibit higher current levels may be monitored during stress in order to detect defect migration.

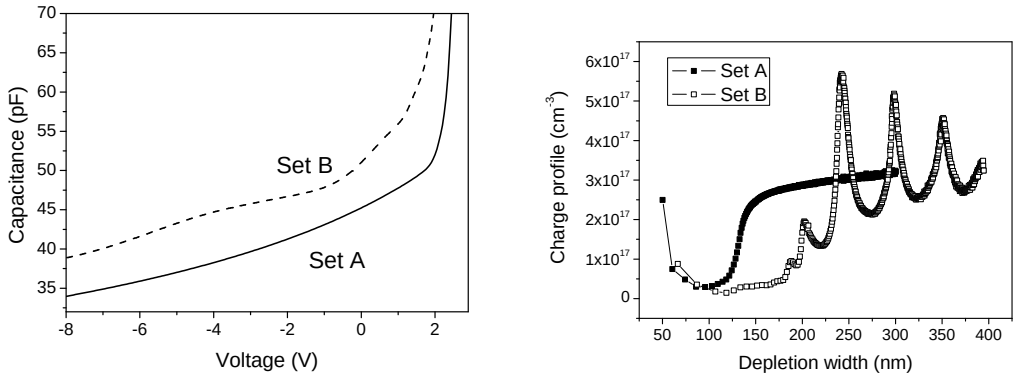


*(a)* *(b)*

*Figure 4.7: Capacitance vs. Voltage measurements of two representative samples from Set A and Set B (a). In (b) the plot of extrapolated apparent charge profile vs. the depletion width has been reported.*

**Capacitance vs. Voltage (C-V)** Capacitive measurement permits to collect information on device structure and the role of non-radiative levels inside semiconductor. Measurements have been performed by means of impedance-meter: a $V_{AC}$ component (amplitude = $50$ mV, frequency = $1$ MHz) is applied to the device and the $V_{DC}$ component is modulated in the range of $-8$ V-3 V. Using a proper model we can extrapolate its impedance. The model employed for LED measurement is the parallel of a capacitance and a conductance, referring to the junction capacitance generated by the depletion region of the p-n junction. By means of this measurement, it is possible to evaluate the distribution of charge in the proximity of the junction, information on the extension of the space charge region and band offsets and on the position of the hetero-interfaces. In Fig. 4.7(a) the C-V plots of representative samples from Set A and B have been reported. As can be noticed, the slopes of the two families of devices are very different. With an analytic method described elsewhere [23], the C-V data could be converted in the apparent charge distribution, reported in Fig. 4.7(b). The graph reports the apparent density of dopant at n-side and thus the internal structure of the chip. Since this technique uses the approximation of unilateral junction (i.e. schottky diode), we can observe also fea-

tures related to the presence of heterojunction. The plot of Set B LED exhibits five peaks that could be generated by a Multi Quantum Well (MQW) inside the active region, or various interfaces between different layers. On the other hand, the profile of LED from Set A exhibits a nearly constant behaviour beyond $150\ \mathrm{nm}$. This comparison permits to underline the structural difference between the two families.

### 4.2.4 Thermal characteristics

A deep investigation on thermal properties has been carried out on LEDs designated for ageing and some samples without PCB. The thermal resistance was extrapolated by means of forward voltage measurement described in 3.3.1. Since the number of samples was high, a setup for measurements in parallel has been designed. The current pulses for the calibration phase have been generated by the SMU Keithley 2612 (pulse width=$100\ \mu\mathrm{s}$, 4-wire configuration). Several fixture with 8 LEDs mounted on PCB (used for the ageing phase) have been inserted in the climatic chamber. Between the fixture and the SMU a Switching Matrix was used. The steady-state measurement was performed at a fixed ambient temperature of $35\ ^{\circ}\mathrm{C}$. In Tab. 4.2 average values of thermal resistance have been reported for PCB samples (72 SMD samples mounted on PCB by automatic process) and bare packages (16 SMD samples). While thermal resistance for bare package samples exhibits a more uniform behaviour and a lower mean value, the thermal resistance values of PCB samples show a higher deviation. The different behaviour detected may be ascribed to different assembly process of PCB samples (die attach, reflow, bonding,...).

*Table 4.2: Average Thermal Resistance of several samples from Set A and B, with and without the PCB*

| Family Family | Average Thermal Resistance (K/W) | Standard deviation (K/W) |
|---|---|---|
| Set A PCB | 289 | 55 |
| Set A chip | 239 | 10 |
| Set B PCB | 285 | 61 |
| Set B chip | 272 | 22 |

Some differences in thermal behaviour between the two families of LEDs have been detected. Concerning the samples from Set A, it has been detected an anomalous behaviour due to the increase of series resistance with temperature, reported in Fig. 4.8(a). This increase acts like a positive feedback in forward voltage and thus in the junction temperature and can induce instabilities. As can be noticed in the figure, the series resistance increase with temperature is more enhanced for samples with a native high resistance. In such samples, the forward voltage have a parabolic behaviour with temperature, instead the expected exponential or linear one. Furthermore, these samples exhibits a positive voltage transient when biased. In this case the junction temperature extrapolation was more approximative. The origin of such effect may be attributed to a unstable and temperature-dependent electrical contact at the metal-semiconductor interface. The anomalous behaviour described has not been detected in LEDs from Set A. However, the Fig. 4.8(b) shows the quadratic relationship between temperature

and input power, detected for several samples from Set B. This behavior may be ascribed to the modification of heat removal properties of the chip, modulated by current crowding.

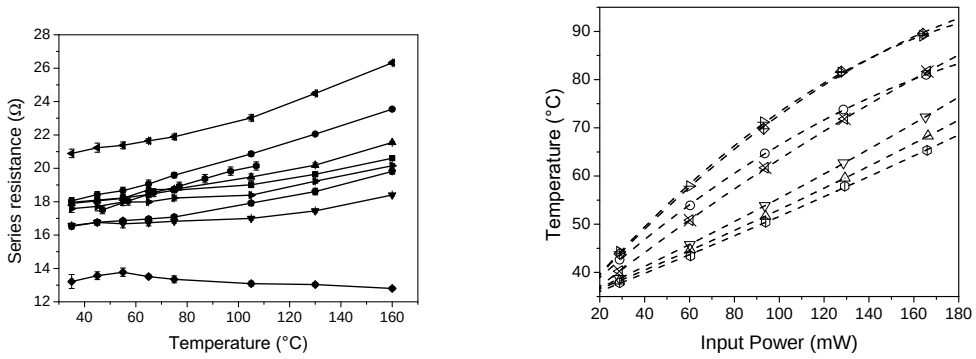


*(a)* *(b)*

*Figure 4.8: Anomalous results found in thermal characterization. In (a) the series resistance of several samples extrapolated at various temperature levels have been reported. In (b) the Temperature vs. Power plots illustrate the not linear thermal resistance behaviour (dotted lines represent the quadratic fitting).*

### 4.2.5 ESD robustness

In this section results on ESD testing are reported. The measurements have been performed by means of Transmission Line Pulse Testing (TLP, details could be found elsewhere [65]). Increasing reverse and forward current pulses ($100$ ns pulse width) have been applied to devices. The current and voltage of the pulses have been measured during testing and after each step the current at $-3$ V has been monitored as failure parameter. In Fig. 4.9 the Current vs. Voltage characteristics during testing have been reported. We choose as failure criteria the shortening of the junction, manifested as the increase of the reverse current at $-3$ V. Both for reverse and forward testing, devices showed a catastrophic failure: the data reported in Fig. 4.9 refer to the current measured just before detecting the failure. As can be noticed, the plots of Set A ESD testing are more scattered than the Set B, but the failure current is similar for all testing conditions.

The failure current measured has been reported on Fig. 4.10(a) (data tabulated on Tab. 4.3). In reverse conditions, the LEDs are less ESD robust, with an average failure current of $6.65$ A for set A samples and $4.91$ A for Set B. LEDs are more robust in forward biasing, with an average current of about $8$ A for Set A and $7.77$ A for Set B. In general, devices from Set A are more ESD robust than Set B LEDs. In order to obtain a correlation with the Human Body Model (HBM) used in manufacturer's datasheets, we can multiply the failure current by $1.5$ kV/A factor. In reverse conditions, we obtain a failure ESD voltage of about $10$ kV and $7.3$ kV for samples from Set A and B respectively. Several samples failed after ESD testing have been de-processed and analyzed by SEM imaging. In Fig. 4.10(b) the image of the finger of one failed device has been reported. The image has been used after ageing in order to compare the effects of ESD and EOS testing and find any possible correlations.

*Table 4.3: Failure current levels for Set A and B samples.*

| Series | Reverse Failure Current (A) | Forward Failure Current (A) |
|---|---|---|
| Set A | $6.65 \pm 0.44$ | $8.02 \pm 0.23$ |
| Set B | $4.91 \pm 0.29$ | $7.77 \pm 0.28$ |

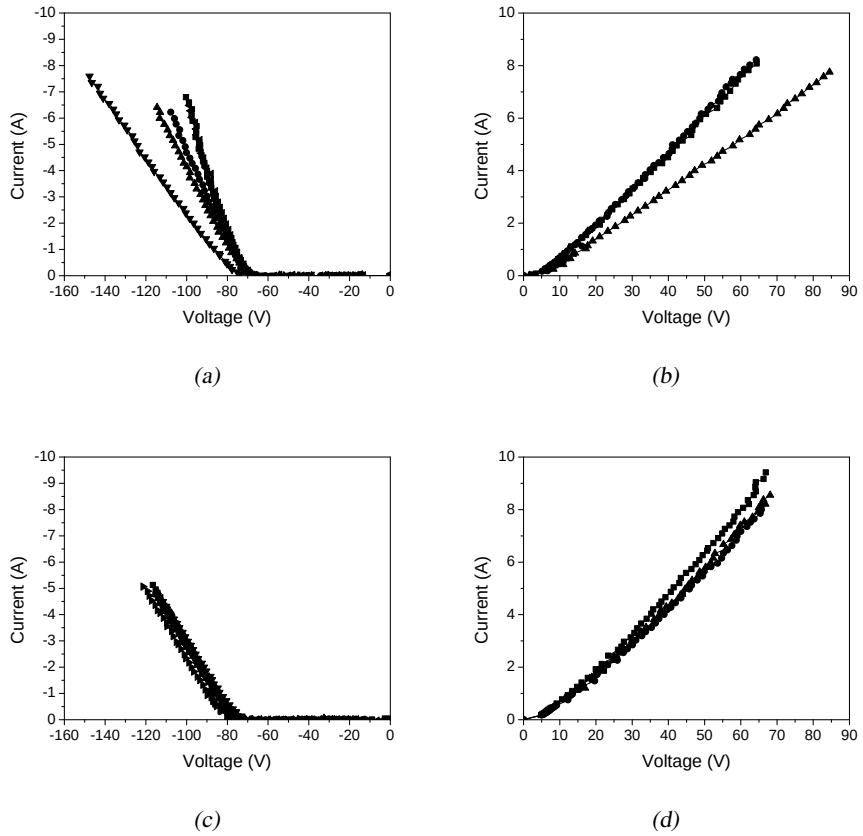


*Figure 4.9: ESD testing results. The (a) reverse and (b) forward measurements from several LEDs from Set A are reported. The same results are reported for LEDs from Set B (c)–(d).*

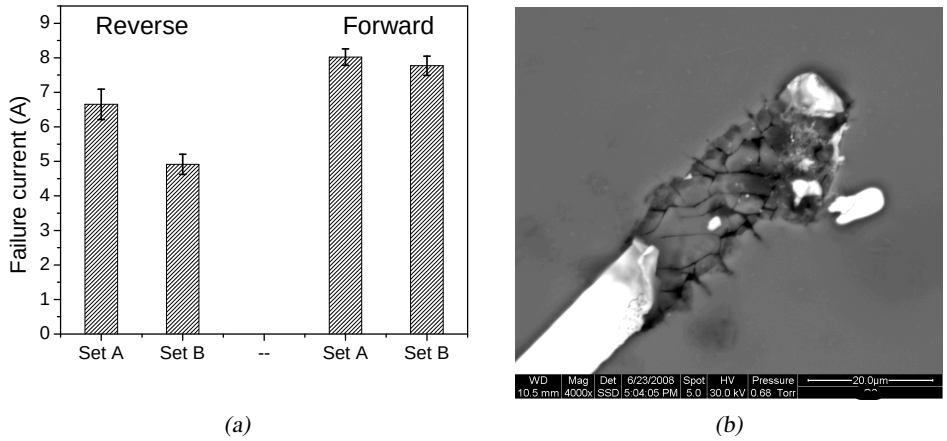


*Figure 4.10: (a) Average current values of ESD failure and (b) SEM image of one failed device of Set A submitted to ESD testing.*

## 4.3 Accelerated Lifetime Testing

Different accelerated ageing tests have been designed and carried out on LEDs aiming (i) at finding the degradation mechanisms involved in LED operation and (ii) at developing a lifetime prediction model for these devices. In particular, we performed an accelerated life test with different bias and temperature conditions (electro-thermal ageing), and a pure thermal storage (thermal ageing), in order to identify the parameters responsible for degradation.

### 4.3.1 Stress conditions

**Experimental setup** In order to obtain a suitable model for lifetime prediction of devices, a wide junction temperature range has been selected for testing. For a first order estimation of the junction temperature the thermal resistance value provided by the manufacturer ($300\ \mathrm{K/W}$) has been employed, while the electrical power has been calculated from the I-V characteristics (Fig. 4.6).

The 4 ageing groups involved have been defined by different ambient temperature and current levels:

1. $T_{amb} = 80\ ^{\circ}\mathrm{C}$, $I_{dc} = 30\ \mathrm{mA}$ (estimated junction temperature=$115\ ^{\circ}\mathrm{C}$)
2. $T_{amb} = 80\ ^{\circ}\mathrm{C}$, $I_{dc} = 50\ \mathrm{mA}$ (estimated junction temperature=$140\ ^{\circ}\mathrm{C}$)
3. $T_{amb} = 100\ ^{\circ}\mathrm{C}$, $I_{dc} = 30\ \mathrm{mA}$ (estimated junction temperature=$135\ ^{\circ}\mathrm{C}$)
4. $T_{amb} = 100\ ^{\circ}\mathrm{C}$, $I_{dc} = 50\ \mathrm{mA}$ (estimated junction temperature=$160\ ^{\circ}\mathrm{C}$)

For each condition, 8 LEDs from Set A LEDs and 8 LEDs from Set B have been designated. The ageing was paused at various time steps until the time limit of 1656 hours was reached. An unbiased testing at $140\ ^{\circ}\mathrm{C}$ have been performed on 8 LEDs from Set A and Set B. The selected storage temperature of $140\ ^{\circ}\mathrm{C}$ corresponds to about the average junction temperature for the 4 groups in the electrical-thermal ageing tests. The unbiased ageing test allowed to distinguish between thermal and electrical failure modes. The thermal storage time was 1320 hours. All the samples have been placed on PCBs in order to emulate the thermal properties of the final application. Aluminum sample holders have been designed in order to carry 8 LEDs, for faster measurements.

**Junction temperature estimation** At the beginning of each electrical ageing session, the junction temperature of each device to be submitted to stress has been extrapolated. The samples have been placed in a climatic chamber at the corresponding ageing temperature in the same position used during stress, in order to preserve heat convection conditions. After waiting for temperature stabilization (about 1h), the devices have been polarized and the steady-state voltage has been measured and converted to junction temperature with analytic techniques explained in section 4.2.4.

In Fig. 4.11 the temperatures reached by all samples and the average for each ageing group have been reported. As can be noticed, Set A samples exhibited temperature levels always

lower than Set B. Anyway, the temperature levels extrapolated are very scattered and the reliability analysis will focus on the individual devices to define a correlation between stress kinetics and junction temperature: the MTTF obtained at the end of ageing will be compared with this initial thermal characterization.

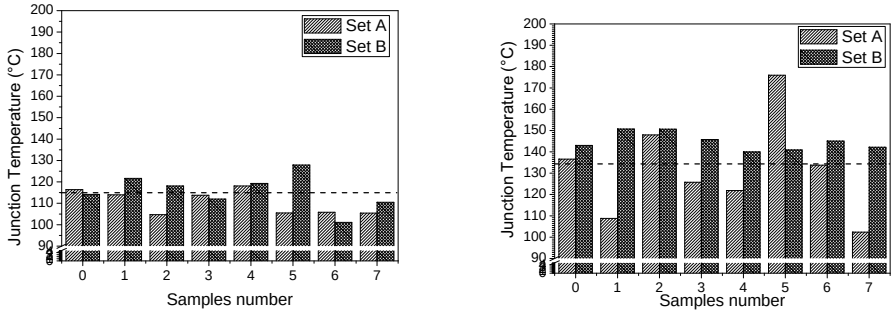


*(a)* I=30 mA, T=80 °C

*(b)* I=30 mA, T=100 °C

*(c)* I=50 mA, T=80 °C

*(d)* I=50 mA, T=100 °C

*Figure 4.11: Junction Temperatures of samples submitted to different stress conditions.*

### 4.3.2 Luminous flux degradation results

At each ageing step the optical characterization (L-I measurement, E-L spectra at $30 - 50$ mA) has been performed on each sample. The E-L spectra have been used in order to extrapolate the luminous flux (lumen). The lumen parameter is useful when analyzing opto-electronic devices for Solid State Lighting application, since this photometric quantity is weighted by the human eye sensitivity. Due to the relevance of such parameter in final application, the lumen degradation could be considered as the main indicator of reliability and lifetime estimation of devices. Furthermore, the luminous flux is the parameter to use for direct comparison of different LED families.

In Fig. 4.12 and 4.13 the luminous flux measured during stress at 30 mA and 50 mA and normalized to initial value have been reported. The plots of lumen decay for different families but same stress conditions are placed besides in order to compare the kinetic and the degradation rate. As can be noticed, the behaviour inside each ageing slot is uniform and the standard deviation of the average reported is low. The degradation has a roughly exponential time-dependent kinetic, with different rate and steady state values. In general, the degradation rate

is higher for Set B LEDs than the Set A ones. Despite the majority of the samples exhibited a gradual degradation, several samples manifested a sudden failure, described in 4.3.5.

Two different approaches of reliability analysis have been faced, in order to identify the degradation process and how they are involved in lumen decay, also related to the different structure of the devices.

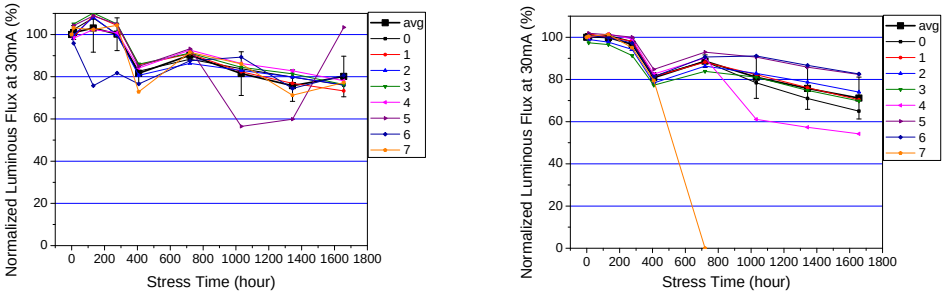


*(a)* SetA: I=30 mA, T=80 °C




*(b)* SetB: I=30 mA, T=80 °C

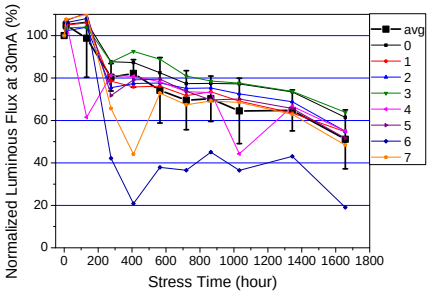


*(c)* SetA: I=30 mA, T=100 °C

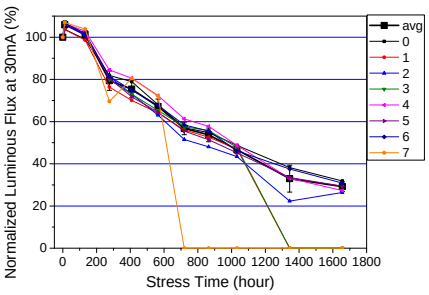


*(d)* SetB: I=30 mA, T=100 °C

*Figure 4.12: Normalized luminous flux during ageing at* 30 mA *for Set A and Set B at different temperature levels.*

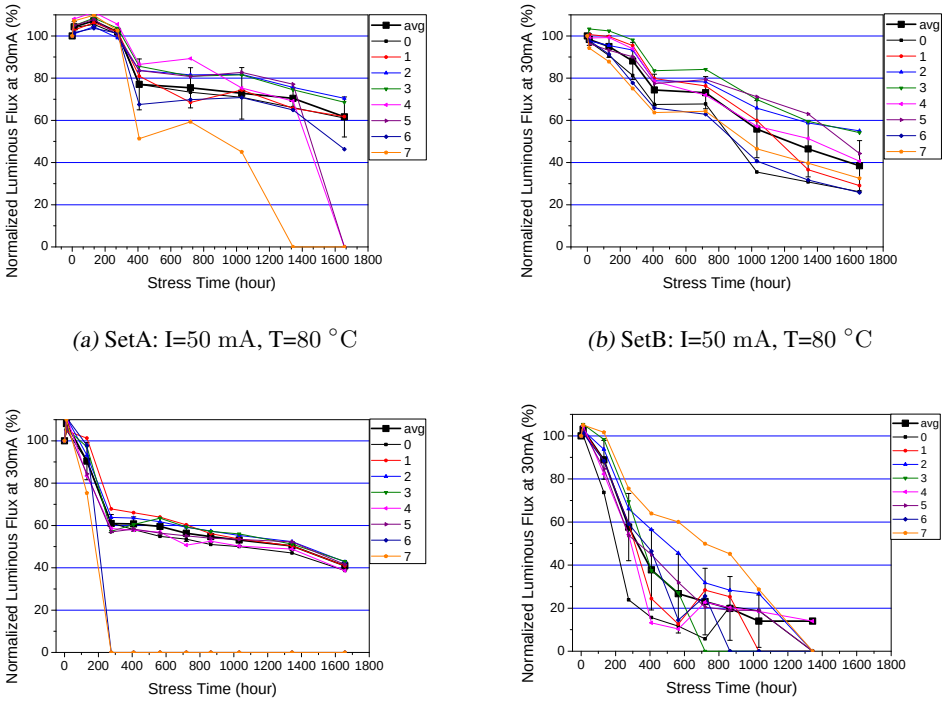


*(a)* SetA: I=50 mA, T=80 °C

*(b)* SetB: I=50 mA, T=80 °C

*(c)* SetA: I=50 mA, T=100 °C

*(d)* SetB: I=50 mA, T=100 °C

*Figure 4.13: Normalized luminous flux during ageing at* 50 mA *for Set A and Set B at different temperature levels.*

**Arrhenius Model** The thermal activated degradation process suggested us o use the Arrhenius model, based on the junction temperature extrapolated and reported in the section 4.3.1. Furthermore, the failure criteria adopted for the analysis as been selected as a 50% of luminous flux loss. Since the kinetics were affected by instabilities due to errors in the measurements, the data have been fitted by single-$\tau$ exponential function, ignoring the recovery during first hours. This method was also usefull to extrapolate the lifetime data on those LEDs that did not reach the failure criteria. This strategy was used instead of censoring data since the degradation kinetic were almost all clear and uniform for all devices. This hypothesis was well supported by following results.

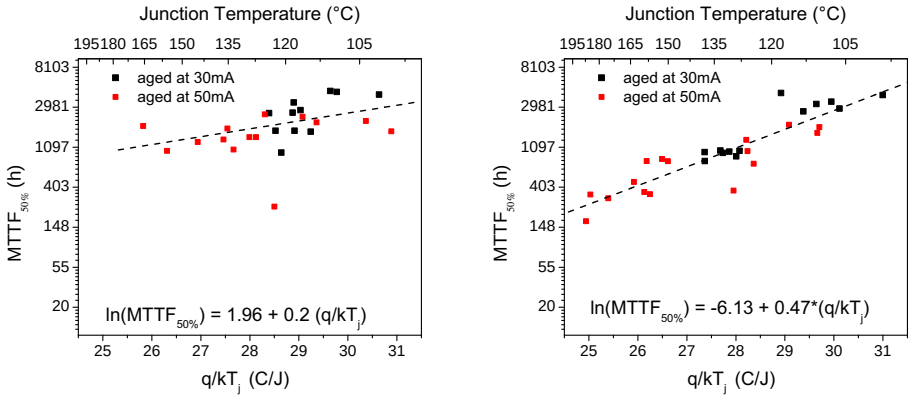


*(a)* Set A *(b)* Set B

*Figure 4.14: Mean Time To Failure with failure criteria of 50% of flux decay($MTTF_{50\%}$) for samples from Set A and Set B. The fitted Arrhenius model has been included in the plot.*

The Arrhenius law is reported in 4.1,

$$L_{50\%}(T) = A \exp\left\{\frac{E_a}{kT}\right\} \tag{4.1}$$

where $L_{50\%}$ is the lifetime at 50% of luminous loss, $A$ is a non-thermal constant, $E_a$ the activation energy of the degradation process (expressed in $\mathrm{meV}$) and $k$ is the Boltzmann constant ($k = 8.623 \times 10^{-5}\mathrm{eV/K}$). In order to verify that the Arrenius law was suitable for the description of the degradation mechanism involved in flux decay of LEDs, the natural logarithm of the lifetime (or Mean Time To failure, MTTF) at 50% have been plotted vs. the reciprocal of $kT$ (reported in Fig. 4.14) and fitted by linear regression, both for Set A and Set B samples. As can be noticed from the figure, the process seems to be thermally activated only for Set B LEDs, with $E_a = 470\ \mathrm{meV}$, against the lower activation energy of $196\ \mathrm{meV}$.

The activation energy for Set B LEDs is rather similar to energies found in the literature [66, 45], and it's valid in a wide temperature range ($105 - 190\ ^\circ\mathrm{C}$). Furthermore, the process is not correlated to the bias level, and the main contribution to the degradation process may be ascribed to the temperature level of the junction.

This result allowed us to predict the lifetime in nominal conditions: it's sufficient to extrapolate the junction temperature at RT, $30\ \mathrm{mA}$ and substitute it in 4.1 with parameters calculated by linear fitting. The $95\%$ confidence interval of predicted response could also be calculated at normal operating conditions. Using a thermal resistance of $300\ \mathrm{K/W}$, a $100\ \mathrm{mW}$ value for electrical power (corresponding to $30\ \mathrm{mA}$) in RT ambient ($T = 300\ \mathrm{K}$), we obtain an estimation of $30.28\ \mathrm{kh}$, with upper and lower predicted response of $71.37\ \mathrm{kh}$ and $3.35\ \mathrm{kh}$ respectively. It's interesting to notice that LEDs biased at half current ($15\ \mathrm{mA}$) can guarantee a lifetime of more than twice the previous value, i.e $66.27\ \mathrm{kh}$. This value is interesting, since the lumen flux of LEDs from Set B is roughly twice than the flux of Set A LEDs: for the application design issues and sample selection, it's important to compare lifetime at the same luminous flux value.

Similar results cannot be extended to LEDs from Set A since the activation energy is too small and the data too scattered to prove that the degradation process is thermally activated. In order to estimate a MTTF value for these samples, a statistical analysis has been performed by means of Weibull Model.

**Weibull Model** The data of lifetime of Set A LEDs have been analyzed by means of Weibull distribution (for a brief description of the Weibull model, see A). In order to find correlation between current level and MTTF and provide a lifetime prediction model, samples have been subdivided in the 4 different ageing groups and the data have been reported in Weibull Plot (Fig. 4.15). The shape parameter and characteristic life obtained by linear fitting have been reported in Tab. 4.4. Looking to the table is clear that the shape parameters are quite different for all ageing conditions. This may indicate that the degradation process do not have a Weibull distribution, although some reliability works on LED demonstrated the contrary [67]. This fact may be ascribed to the few number of samples per stress condition used for analysis, not sufficient for an accurate analysis. Furthermore, in many cases the steady state flux value (reached or extrapolated by exponential fitting) was above the 50% of loss. Finally, the small influence of the junction temperature on degradation affected the correct lifetime estimation and probably different degradation process are involved in lumen decay. These considerations will be applied in future reliability works, and higher volumes of samples will be analyzed.

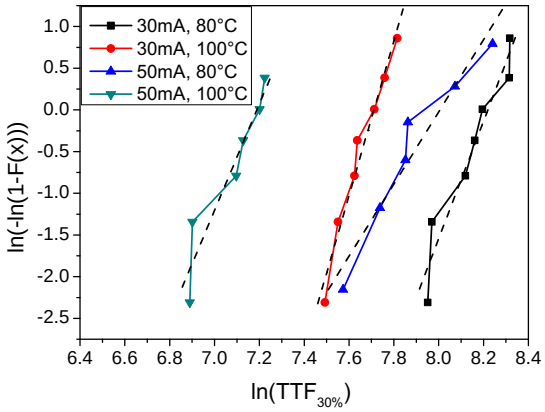


*Figure 4.15: Weibull plot of the Set A samples with failure criterion of $TTF_{50\%}$. The particular scales used for axys help to compare the processes.*

| Ageing Session | Slope Parameter | Intercept | Characteristic Life(h) |
|---|---|---|---|
| 30 mA, 80 °C | $7.05 \pm 0.87$ | $-57.95 \pm 7.12$ | 3710 |
| 30 mA, 100 °C | $9.28 \pm 0.75$ | $-71.58 \pm 5.74$ | 2232 |
| 50 mA, 80 °C | $4.32 \pm 0.56$ | $-34.61 \pm 4.46$ | 2997 |
| 50 mA, 100 °C | $6.39 \pm 1.05$ | $-45.91 \pm 7.47$ | 1325 |

*Table 4.4: Parameter obtained from linear fitting of Weibull plot reported in Fig. 4.15.*

**Thermal storage comparison** In Fig. 4.16 the thermal stress results in terms of lumen decay have been reported. Samples form Set B exhibited a higher steady-state luminous decay, i.e. the 86% of flux loss versus the 59% of Set A samples. However, the time constant of the degradation process is quite similar (405h for Set A, 401h for Set B). This means that the degradation process could be the same, but with different impact on devices, depending on chip structure, device design and phosphors composition.

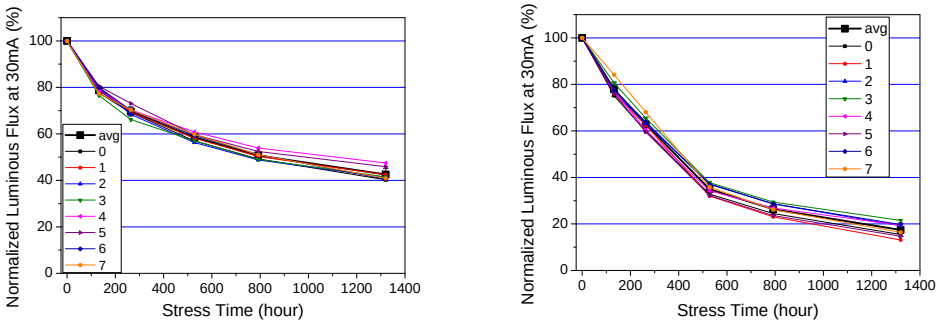


*(a)* SetA: T=140 °C *(b)* SetB: T=140 °C

*Figure 4.16: Normalized luminous flux during thermal storage at* 140 °C *for Set A and Set B LEDs.*

Furthermore, the degradation for samples submitted to thermal storage at 140 °C was found to be more enhanced than the degradation at same average value of junction temperature (Fig. 4.13(a)-(b)). This fact was justified by the uniform temperature distribution in thermally aged samples, while in electrically aged devices the heating was concentrated around the active region. This results indicate also that the degradation may occur both in the active region (chip level), and at package level (phosphors, epoxy). In order to identify the different degradation mechanisms found (thermally activated in the case of Set B LEDs), the modification in spectral properties have been analyzed and reported in the following section.

### 4.3.3 E-L spectra degradation results

The Electro-Luminescence spectra have been monitored during thermal and electrical stress. The spectra used for the analysis have been collected at the bias level of 30 mA. Two different analysis have been carried out. One was based upon photometric parameters calculated from the spectra: the X and Y CIE values. This analysis could provide information on reliability of devices in terms of quality of white. However, a few information on degradation mechanism could be collected and a the direct comparison of measured spectra could help the investigation.

**CIE 1931 color space analysis** The X and Y values can give qualitative information on chromatic properties of PC-LEDs and are widely used in characterization of commercial devices. At each storage step the x and y values (based on 1931 CIE standard) have been calculated for all LEDs. Then the average value for each ageing session has been plotted in the color map and reported in Fig. 4.17 (stress at 30 mA), in Fig. 4.18 (stress at 50 mA) and Fig. 4.19 (pure thermal storage). In the figures a little offset in x and y values from the central white can be

noticed: this is related to not perfect conversion and to chromatic properties of the represented color map; however, it does not afflict the relative variations.

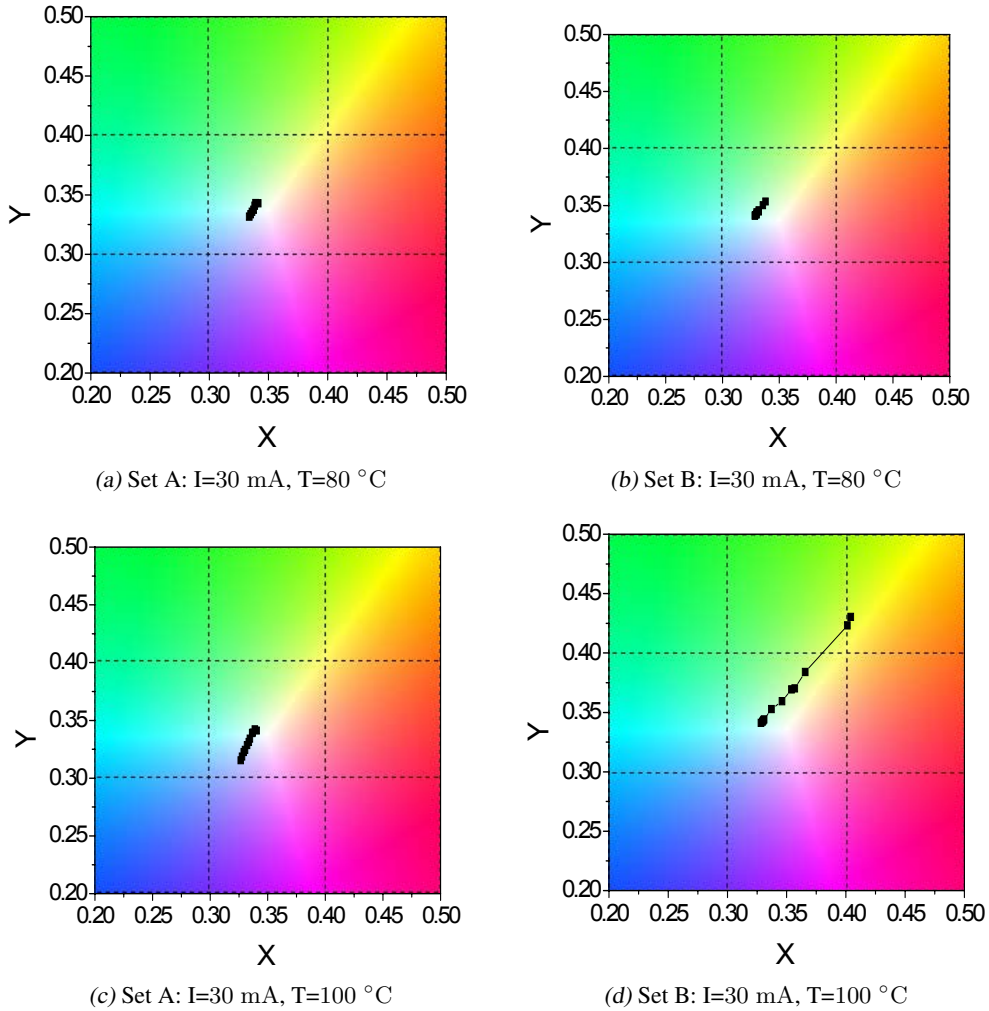


*(a)* Set A: I=30 mA, T=80 °C

*(b)* Set B: I=30 mA, T=80 °C

*(c)* Set A: I=30 mA, T=100 °C

*(d)* Set B: I=30 mA, T=100 °C

*Figure 4.17: Average color map of LEDs from Set A and B during ageing at* 30 mA *at different temperature levels.*

The figures report that the devices are subject to color shift during ageing, more enhanced at harsher conditions. It's worth noticing that the shift is related to the LED family: while LEDs from Set A exhibited a blue shift, the Set B devices tends to yellow after ageing. Furthermore, looking to thermally aged devices from Set B (Fig. 4.19(b)), one can notice that the color shift is quite different from the shift caused by electrical ageing. This means that the degradation mechanism is the same for thermal and electrical stress, that is thermally activated. As mentioned before, the more uniform temperature distribution in thermal storage may affect the overall package chromatic properties, providing a different impact on degradation with respect to electrical ageing. For a in-depth analysis of degradation mechanism involved, the comparison of E-L spectra has been carried out.

**E-L spectra comparison** In Fig. 4.20 the E-L spectra of two representative samples from Set A and B during thermal storage have been reported. In the inset graph the ratio between

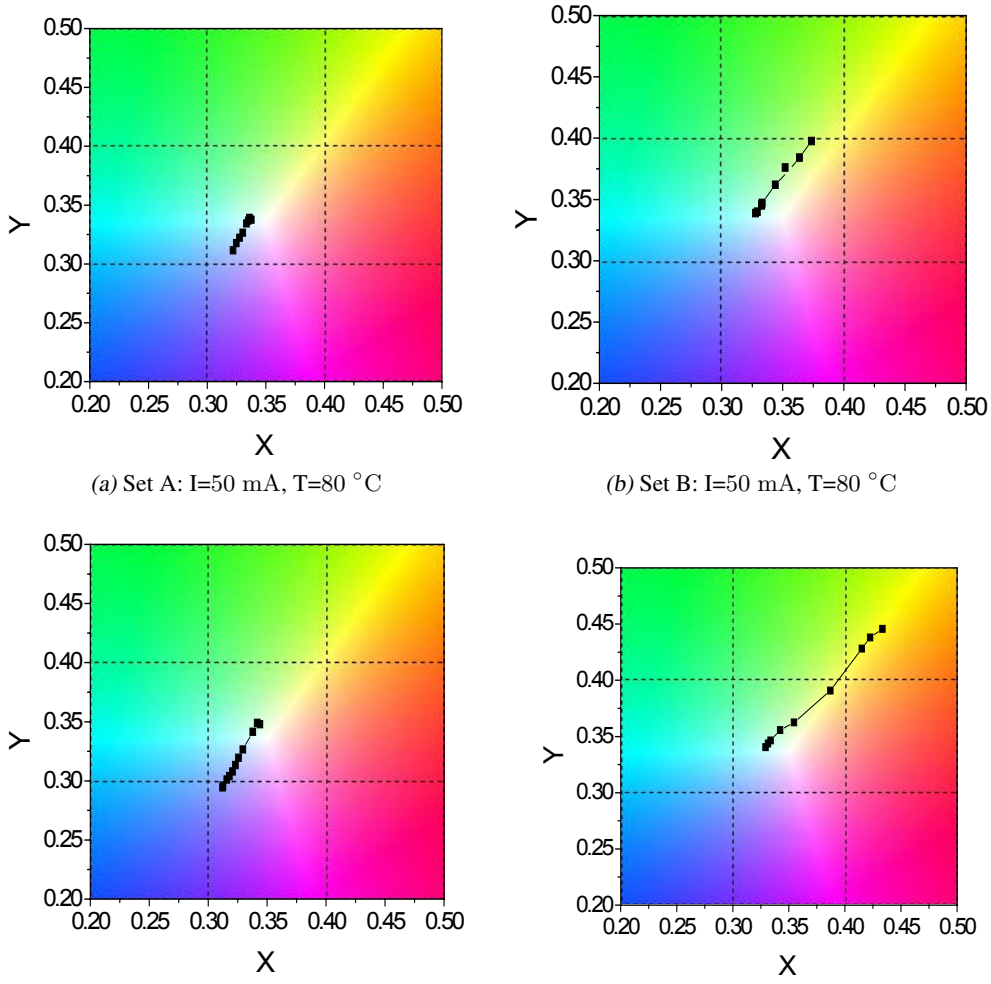


*(a)* Set A: I=50 mA, T=80 °C

*(b)* Set B: I=50 mA, T=80 °C

*(c)* Set A: I=50 mA, T=100 °C

*(d)* Set B: I=50 mA, T=100 °C

*Figure 4.18: Average color map of LEDs from Set A and B during ageing at* 50 mA *at different temperature levels.*

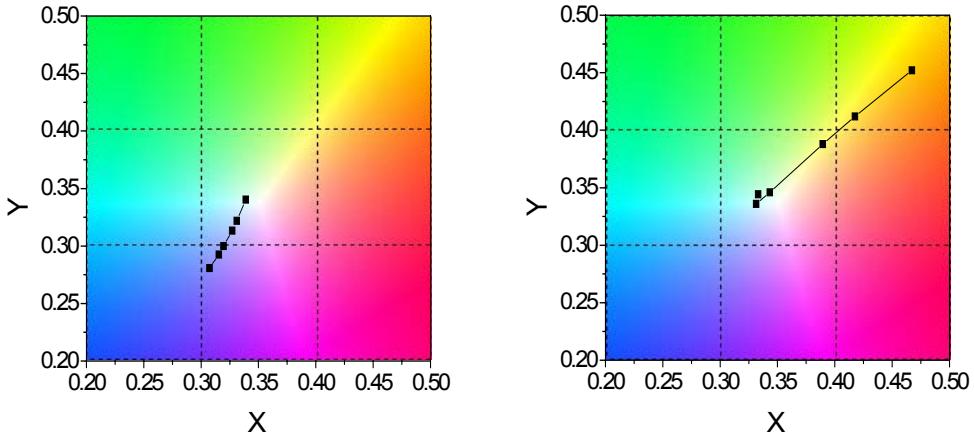


*(a)* Set A: T=140 °C

*(b)* Set B: T=140 °C

*Figure 4.19: Average color map of LEDs from Set A and B during thermal storage at* 140 °C.

the integral of yellow and blue peak has been included. The degradation mechanisms for the two families are very different. While the LEDs from Set A manifested a decay in yellow and blue peak, more enhanced for yellow (a variation in the ratio of about 40%), the blue peak of LEDs from Set B tended to disappear during stress, and the variation at the end of the stress is roughly 3000%. These behaviours are similar for all devices and the impact of ageing is higher for harsher conditions. Starting from these considerations, an attempt of degradation mechanism identification has been made.

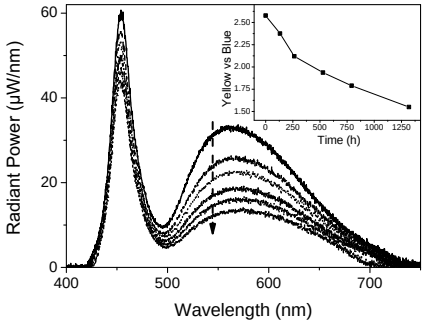


*(a)* Set A: T=140 °C

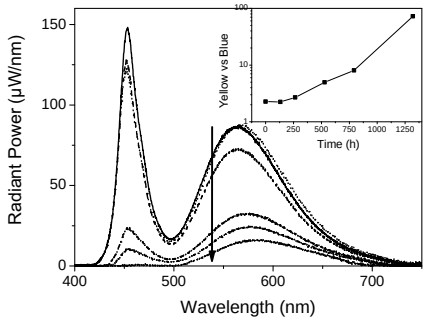


*(b)* Set B: T=140 °C

*Figure 4.20: Electro Luminescence spectra of one representative LED from (a) Set A and (b) set B submitted to thermal ageing. In the inset graph the ratio between Yellow/Blue peak during stress is reported.*

**Discussion on degradation mechanism** In both family A and B we may infer that the degradation mechanism associated with the worsening of chromatic properties is related to the package. This hypothesis is based on the proven reliability of InGaN blue LEDs when aged in the temperature and current range investigated in the earlier works [68].

Furthermore, excluding the instability of the YAG phosphors [43, 44], we have to consider the instability of the epoxy composing (i) the lens and (ii) the whole package. The transmittance of the epoxy of the lens could degrade during ageing due to high temperatures and act as a filter. On the other hand, it was observed that the white epoxy of the package darkened during ageing, with a worsening of the reflectivity that may impact on chromatic properties[15, 69]. Since for Set A the degradation is less thermally activated with respect to Set B LEDs, the variation of chromatic properties is limited and is not correlated with different ageing conditions (thermal storage or electrical ageing), as shown in Fig. 4.19(a).

The more enhanced thermally activated degradation process of LEDs from Set B suggests the use of different and more unstable material for the encapsulation. Since the activation energy is higher than the energy of LEDs of Set A, there is a correlation between temperature distribution and impact on degradation.

### 4.3.4 Electrical and Thermal results

**I-V Characteristics modification** The I-V characteristics of the whole set of LEDs have been monitored during electrical and thermal ageing. In particular, the voltage value at a fixed

current value of $30\ \mathrm{mA}$ have been evaluated, together with the reverse current modification. However, no modifications have been detected neither among Set A LEDs nor Set B. This means that: (i) the contact are stable and the electrical properties in forward region are not influenced by ageing, since the temperatures involved are fairly below critical levels [68]; (ii) the leakage current stability indicate that the degradation in first approximation could not be ascribed to an increase of defect density in the bulk or active region of the chip. Thus we may infer that the InGaN chip is not involved in the degradation of the overall device. Different comments have to be made concerning the electrical failures detected on a few samples and will be discussed in the Failure Analysis section.

**Thermal Resistance stability** The thermal resistance characterization has been performed at the beginning of the ageing sessions, during the thermal stress (528h) and at the end of every sessions (1656h for electrical stress, 1320h for thermal ageing). This analysis provided more details on the investigation of degradation mechanisms.

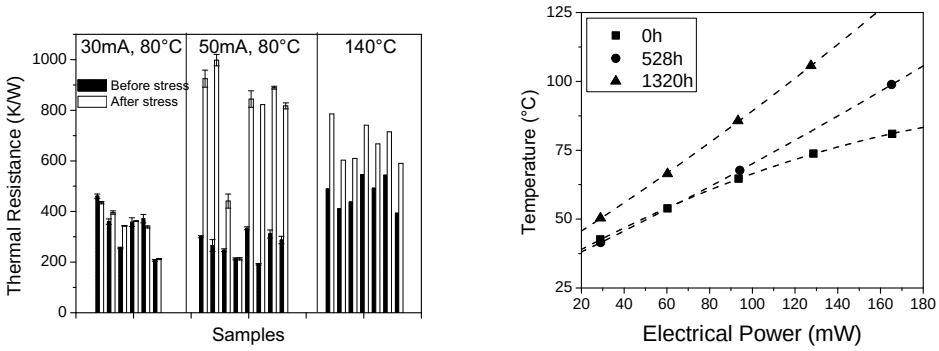


*(a)* *(b)*

*Figure 4.21: Thermal characterization: (a) comparison between Set B thermal resistance values measured before and after stress, and (b) the Temperature vs. Power plot of one representative device from Set B submitted to thermal storage.*

In Fig. 4.21(a) the thermal resistance of aged devices has been reported for each ageing condition. As can be noticed, the data for some samples are unavailable, due to the failure of the devices that make the temperature extrapolation from electrical measurements impossible (see section 4.3.5. While for Set A samples the thermal resistance remained unchanged (not reported in the figure), it could be noticed that Set B samples manifested an increase for devices aged at harsher conditions. This translates in higher junction temperatures at the end of the stress, originating a positive feedback: the higher the temperature is, the higher will be the increase of thermal resistance and so on. The temperature increase found was confirmed by a decrease in luminous efficiency at higher current levels for these LEDs. In addition, in Fig. 4.21(b) the temperature vs. input power ($T_j(P_{el})$) has been reported for one sample from Set B thermally aged. Looking into the figure we can notice that the function $T_j(P_{el})$ is quadratic at the beginning and at the end of the stress, but with different concavity. This fact could be related to the modification of luminous efficacy at different current levels reported before.

The thermal analysis was useful to detect a relationship between chip structure and impact of ageing on thermal management. The fact that the samples from Set B exhibited some sudden failures (acting like open circuits) and an increase their thermal resistance could be ascribed to a partial detachment of the contact/bonding wire/die attach. The X-ray analysis on aged and failed devices should provide information and confirmations to these hypothesis and will be reported in the following section.

### 4.3.5 Failure Analysis

The analysis performed on failed devices aimed at finding the mechanism responsible for failures and degradation processes found during ageing. This analysis was carried out by means of Scanning Electron Microscope imaging and Emission Microscopy (EMMI) and X-Ray imaging.

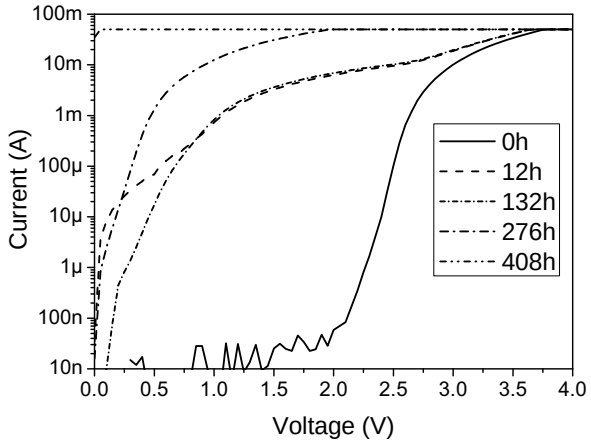


*Figure 4.22: Forward I-V characteristics of one representative sample from Set A during electrical stress at* $I = 50\ \mathrm{mA}, T = 100\ ^{\circ}\mathrm{C}$.

**SEM and EMMI analysis** The analysis was performed both on samples from Set A and Set B, but interesting results have been obtained only for failed Set A LEDs that became short circuits during stress. Several samples submitted to harsher stress conditions manifested a current increase in the low voltage region. For instance, the I-V characteristics of one LEDs submitted to ageing at $I = 50\ \mathrm{mA}, T = 100\ ^{\circ}\mathrm{C}$ have been reported in Fig. 4.22. This sample failed after first $276$ hand was removed from the package by etching and a observed by means of SEM SE imaging. Several holes with a few microns diameters have been found on the surface, around the edge of the contact. The particular of one hole has been reported in Fig. 4.23(a). The figure suggests the hypothesis that these holes are generated by thermo-electrically activated migration of already present dislocation. The increment of dislocation density can short the junction. This hypothesis was confirmed by the Emission Microscopy image reported in Fig. 4.23(b). The image was obtained with a Hamamatsu PHEMOS-200 microscope equipped with a cooled CCD camera. Here the image of the emission of other samples submitted to

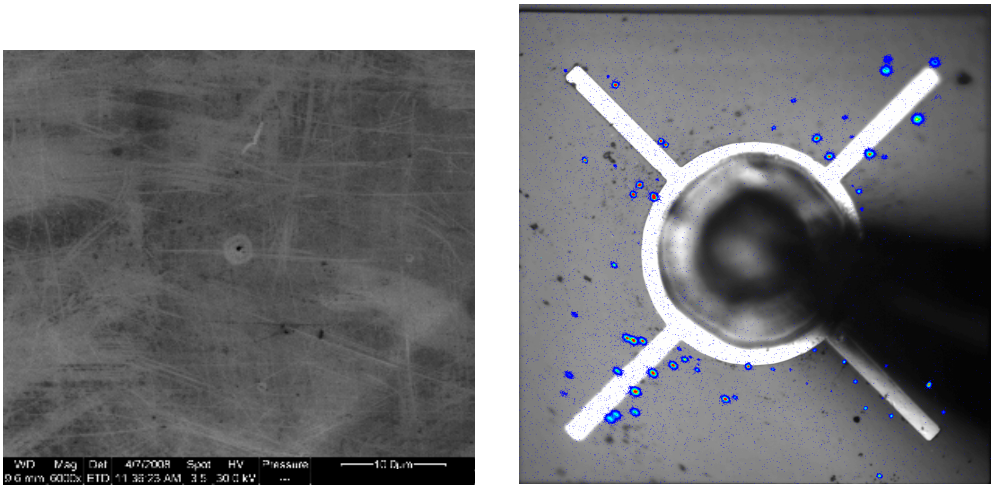

(a) (b)

*Figure 4.23: Failure Analysis on one LED from Set A. The Secondary Electron image (a) revealed several holes on the surface near and below the p-side pad. The EMMI image reported (b) has been obtained applying a reverse bias of $-5$ mA and shows the leakage path across the junction.*

identical ageing conditions and failed biased at -5mA have been reported. The false-colour spots are localized manly around the contact area. The hypothesis of shortening path is in good agreement with the increase of leakage current observed. When the current density flowing through these dislocations is higher enough, the junction is shortened and the devices does not emit any more. These shortening path could be broken by submitting the device to high current levels (above nominal values): in that case the devices return to emit, but the leakage current persists.

**X-Ray analysis** Several failed and degraded devices from Set B have been analyzed by means of X-Ray imaging thanks to the facilities provided by Applied Optic group at DEI. Looking to the Fig. 4.24 we can notice that the whole layer containing the chip, bonding wires and phosphors manifested a partial detachment from the aluminum reflector below the chip. The detachment afflicted the thermal resistance of the device due to limited heat dissipation capability, since the reflector acts like heat sink. In addition, the detachment involved the bonding wires, soldered to the reflector that is the electrical contact of the package. When the bonding wires were detached, the devices failed and became on open circuit. As mentioned above, LEDs acting like open circuits can emit when a low pressure is applied on the top of the device.

The degradation mechanism detected could be ascribed to high temperatures reached by the junction. The different coefficients of thermal expansions of the phosphors cup, aluminum and the plastic of the package impact on the adhesion of the different materials up to the detachment of the cup.

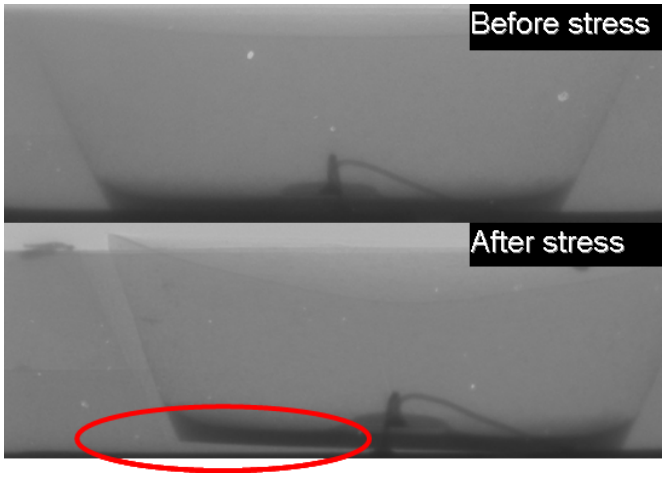


*Figure 4.24: X-Ray imaging of one samples before and after stress at $I = 50$ mA, $T = 80$ °C.*

## 4.4 Conclusions

An in-depth electro-optical-thermal characterization and ALT on different families of low-flux PC-LEDs have been carried out on a large set of samples. The initial characterization pointed out the differences in terms of performances between the two different design of LED structures. During the electro-thermal ALT the different optical, electrical and thermal properties have been monitored in order to find a correlation between different failure modes. A reliability analysis based on results obtained during stress provided the estimation of the degradation model. In particular the work provided several original results:

1. the development of a setup for fast and reliable characterization in terms of electrical, optical and thermal properties;
2. a statistical analysis of thermal resistance of a wide set of samples;
3. the detection of several failure modes (lumen decay, chromatic shift, thermal resistance increase), correlated to the stress temperature;
4. the extrapolation of the exponential degradation model, suitable for lifetime prediction;
5. the identification of the lens and package browning as responsible for lumen decay and chromatic shift;
6. the identification of mechanism responsible for failures, as the detachment of the encapsulation and the generation of parasitic electrical paths.

The work presented in this chapter provided also relevant information on package reliability, useful for the improvement of the processes and the selection of materials employed in LED manufacturing.

# Chapter 5

# Chip-On-Board Technology: a reliability analysis

*The chapter provides a description of in-depth analysis of reliability of High Brightness LEDs with Chip On Board technology. The lifetime prediction analysis and the extrapolation of the degradation model relies on a wide set of samples and ageing conditions. The possibility of directly comparing the degradation process of LEDs with and without phosphors permitted the identification of physical mechanisms responsible for luminous decay.*

## 5.1 Overview and specific goals

The output efficiency reached by High Brightness LEDs(HB-LEDs) is growing since the first devices appeared in the market. However, the issue that still limits outstanding lifetimes is represented by high temperature levels involved during LED operation (see chapter 3 for an in-depth discussion on this topic). Several solutions for a better thermal management are still under investigation: research on high thermal conductivity materials, development of novel structures, the improvement of quantum internal efficiency. Up to now, the solution that offers both high performances in terms of thermal management and low costs of productions is the Chip-On-Board Technology (COB).

The COB technology is based on a simple concept: the elimination of several thermal interfaces that contribute to the self-heating of devices. In the case of LED structure, the current packages used for HB-LEDs offer a great versatility and modularity in application design, but suffer from the high thermal resistance caused by thermal interfaces. The LED implemented in COB technology provides a great decrease in thermal resistance since the chip is directly attached to an aluminum board, that act as a heat sink due to high heat capacity. In this case the attachment of a more efficient heat sink have a lower impact on the overall thermal resistance. For an applicative example of COB LEDs, see [70].

On our knowledge, no works on COB LEDs reliability have been published up to now. Thanks to the experience in reliability analysis and opto-electronic devices characterization of our labs, an extensive analysis of reliability of COB based HB-LEDs has been performed and presented in this chapter. A set of about 180 blue and white LEDs has been submitted to

thermal and electro-thermal ageing conditions. The results obtained by the analysis confirmed the high reliability of such structures and provided the estimation of the degradation model.

The work was organized in subsequent steps:

1. the thermal and optical characterization of a wide set of samples;
2. the design and implementation of an accelerated thermal and electro-thermal ageing setup for lifetime prediction, with the continuous monitoring of devices properties during stress;
3. the analysis of results from optical and electrical data;
4. the extrapolation of the degradation model.

**Specific goals** The present work aimed at:

1. providing a detailed thermal analysis on COB technology in order to investigate the benefits of such structures in terms of thermal resistance;
2. finding the ALT setup able to provide both the accuracy of measurement and short time expense in measuring , fundamental for wide set of samples;
3. developing the degradation model, starting from the literature examples, able to make an accurate lifetime prevision;
4. identifying the degradation mechanisms responsible for luminous decay.

## 5.2 Device Structure and Characterization

Before the ALT, the devices have been submitted to a optical and electrical characterization (see details in chapter 3). In particular, the thermal characterization has been performed both in single and multi LEDs condition. Some theoretical analysis on thermal behaviour of multi-chip approach will be provided.

### 5.2.1 Device structure

The devices studied in this work are High Brightness LEDs with Chip on Board (COB) technology. The chip are $1\mathrm{x}1\ \mathrm{mm}^2$ area GaN/InGaN LEDs emitting at $456\ \mathrm{nm}$. The chip structure is vertical, based on SiC substrate. The chip has been attached to an aluminum board of about $1\mathrm{x}2\ \mathrm{cm}^2$ area and the die attach was realized by a conductive adhesive. Afterwards, the bonding wires have been created. On the chip a protective silicon encapsulation has been deposited. The encapsulation has also the important role of lens, the optical interface between the chip and air. In order to generate white light, a mixture of yellow phosphors has been included in the encapsulation. In Fig. 5.1 a schematic of COB technology LED has been reported.

The device are designed to operate at $700\ \mathrm{mA}$ bias level, that corresponds to a current density of $70\ \mathrm{A/cm}^2$. The maximum rating of junction temperature suggested by the manufacturer is $125\ ^\circ\mathrm{C}$.

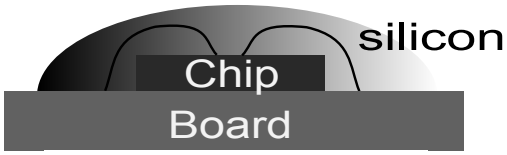


*Figure 5.1: Schematics of Chip On Board LED structure.*

### 5.2.2 Characterization

In the following, a brief overview of optical and thermal characteristics of devices under analysis will be provided.

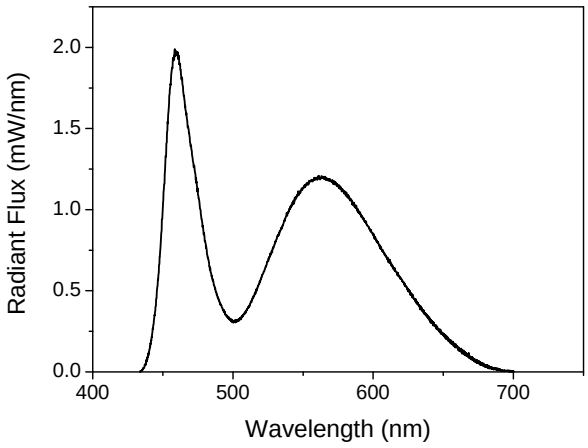


*Figure 5.2: EL spectrum of one representative devices biased at* $700\ \mathrm{mA}$.

**Optical Characteristics** In Fig. 5.2 the Electro-Luminescence spectrum of one representative device has been reported. The EL spectra have been collected in a wide current range ($1 - 1500\ \mathrm{mA}$) and the results of the spectral analysis have been reported in Fig. 5.3. In particular, in the figure the blue vs. white ratio has been reported. Such parameter has been calculated by means of equation 5.1:

$$B/W = \frac{\int_{420\ \mathrm{nm}}^{500\ \mathrm{nm}} \mathcal{S}(\lambda)\mathrm{d}\lambda}{\int_{420\ \mathrm{nm}}^{700\ \mathrm{nm}} \mathcal{S}(\lambda)\mathrm{d}\lambda} \tag{5.1}$$

and is used to evaluate the conversion efficiency of yellow phosphors.

As can be noticed from Fig. 5.3(a), the B/W ratio is not constant with current. In lower current range ($1 - 10\ \mathrm{mA}$) the B/W ratio tends to decrease, due to low optical flux; in the middle (and operating) range ($10 - 500\ \mathrm{mA}$) the conversion efficiency is quite stable, while in the highest current range ($500 - 1500\ \mathrm{mA}$), the ratio showed a great increase, due to a lower yellow conversion efficiency. This fact can be explained looking to Fig. 5.3(b), where the B/W ratio has been compared to the wavelength shift of blue peak. From the figure is clear that the two mechanisms are correlated: the spectral response of phosphors excitation is not

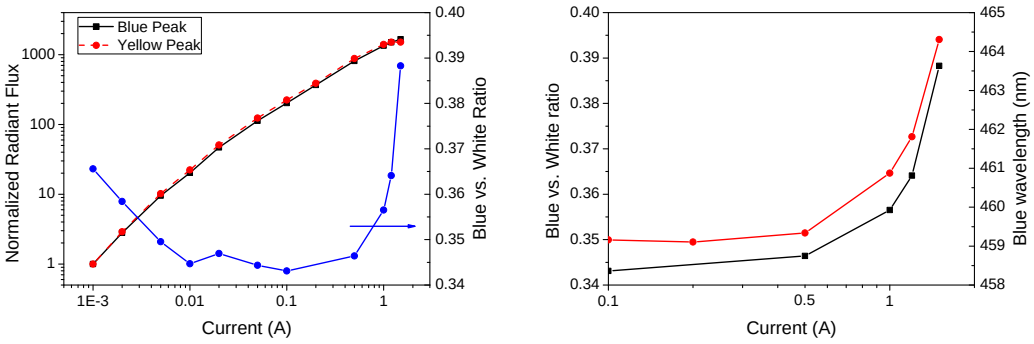


*(a)* *(b)*

*Figure 5.3: Spectral analysis for one representative device biased at different current levels: (a) comparison between the integral of blue and yellow peak and the Blue vs. White Ratio, and (b) comparison between B/W Ratio and the blue peak wavelength shift.*

constant with wavelength and a shift from the response peak causes a decrease in conversion efficiency. Finally, the red-shift of blue peak with current can be ascribed to a thermal induced bandgap narrowing: although the LED were mounted on heat sink, this negative effect cannot be removed.

**Thermal Characteristics** The thermal characterization before the stress was performed on all samples in order (i) to have a parameter to monitor during stress (i.e. the thermal resistance), and (ii) have an estimation of the junction temperature of devices submitted to electro-thermal storage. The estimation of the thermal resistance and the junction temperature was provided by the experimental method described in section 3.3.1. All samples have been characterized in the experimental setup used for ageing (see section 5.3.1). From the measurements we obtained a thermal resistance value of $13.5 \pm 0.9$ K/W for blue devices and $15.4 \pm 0.8$ K/W for white ones. The slightly higher thermal resistance value for white LEDs can be related to the low thermal conductivity of the phosphors, or to the energy losses due to photonic conversion that contributes to self-heating. However, the thermal resistance was low thanks to the short thermal path provided by COB structures like these.

While this method was useful for junction temperature estimation when the single device is biased, it gave no information on self heating when all the 8 LEDs on the aluminum plate where biased simultaneously. Looking to the Fig. 5.4, we can use an equivalent electrical circuit that can describe the thermal behaviour. In Fig. 5.4(a), the schematic of one biased LED attached to a heat sink (or board) is reported. In this case the junction temperature $T_j$ can be expressed by:

$$T_j^{Single} = T_{amb} + P\left(R_{j\_b} + R_{b\_amb}\right) \tag{5.2}$$

where $P = P_{el}$ means a total conversion from electrical input power to heat. On the other hand, when all the 8 devices are biased the junction temperature of one LED gives:

$$T_j^{Multi} = T_{amb} + PR_{j\_b} + 8PR_{b\_amb} \tag{5.3}$$

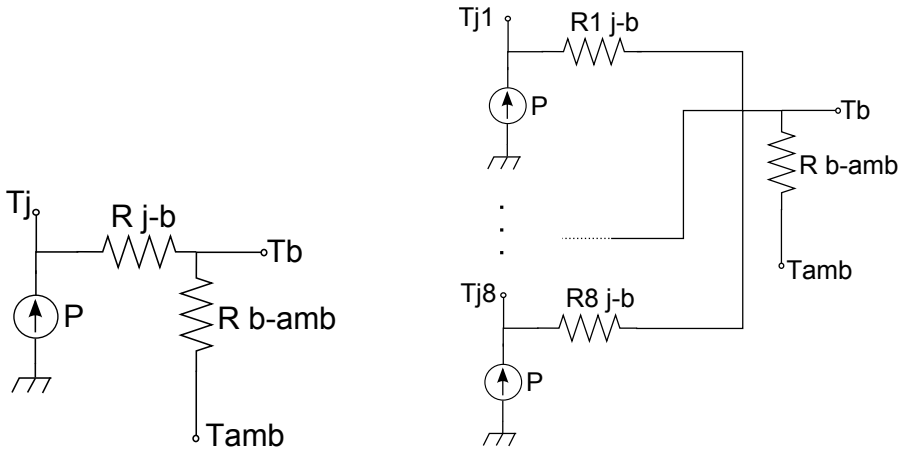


*Figure 5.4: The equivalent electrical model of thermal resistance of (a) one single device biased, and (ii) 8 devices biased simultaneously (P is the electrical power dissipated by a device, $R_{j\_b}$ is the thermal resistance between the junction and the aluminum board, $R_{b\_amb}$ between the board and the air, $T_j, T_b, T_{amb}$ the junction, board and air temperatures).*

where is clear that the junction temperature of one LED is higher than the single bias case. From this model one can extrapolate the $R_{j\_b}$ and $R_{b\_amb}$, in order to estimate the board temperature and other information on heat conduction path. Combining equations 5.2 and 5.3 one finds that

$$T_j^{Multi} = T_j^{Single} + 7PR_{b\_amb} \tag{5.4}$$

and thus extrapolating thermal resistance and temperature of the aluminum board

$$R_{b\_amb} = \frac{T_j^{Multi} - T_j^{Single}}{7P}; \qquad T_b^{Single} = R_{b\_amb}P; \qquad T_j^{Multi} = 8T_j^{Single} \tag{5.5}$$

The junction temperatures in singe and multi bias mode have been collected. Using equation 5.5, we obtained a $R_{b\_amb} \approx 1\ \mathrm{K/W}$ for nominal condition (Room Temperature and $700\ \mathrm{mA}$).

The thermal analysis presented is useful when a multi-chip approach is adopted. Even if a $1\ \mathrm{K/W}$ thermal resistance has a small influence in single-LED configuration, it must be considered when several High Power LEDs share the same heat-sink: i.e., a SSL system equipped with 10 2 watt-LEDs, may induce a further self heating of about $20\ ^{\circ}\mathrm{C}$ with respect to single LED.

## 5.3 Accelerated Lifetime Testing

The main activity on COB LEDs reliability is focused on lifetime testing of devices under accelerated conditions. Two different testing approaches are proposed: a thermal storage session at different temperature levels, and a combined electro-thermal ageing session at nominal conditions and at a fixed junction temperature level. This approach permitted to distinguish between different degradation mechanisms activated by temperature level or current flow, in order to provide the most accurate degradation model for the lifetime estimation. In addition, the test was performed on LEDs with and without phosphors in order to isolate the degradation modes related to phosphors conversion.

### 5.3.1 Experimental setup

The ALT has been designed in order to obtain degradation models starting from short term ageing session. Thus, several ageing conditions have been selected, both for the thermal storage and for the electro-thermal stress. The temperature range selected for thermal storage was $100 - 200\ ^{\circ}\mathrm{C}$. On the other hand, we selected the conditions for electro-thermal stress that can guarantee a constant junction temperature, i.e. $160\ ^{\circ}\mathrm{C}$. In addition, a stress at nominal operating conditions ($70\ \mathrm{mA}$, Room Temperature) has been implemented. Tab. 5.2 gives an overview of all stress conditions: in the table the total ageing times have been reported.

In order to provide a statistical description of the degradation model, 8 white LEDs and 8 blue LEDs have been submitted to every ageing session, for a total amount of about 180 devices. The 8 devices have been attached to an aluminum plate by means of thermally conductive adhesive. The electrical contact realized made possible to bias all the samples in series, and to perform measurements with a 4-probe configuration. Each LEDs was designated with a code like the following

| W | O | G | 5 |
|---|---|---|---|
| ↓ | ↓ | ↓ | ↓ |
| Color | Oven temperature | Self heating | LED number |

where the Color label can be W (for White) or B (for blue), the Oven temperature and Self heating label refer to Fig. 5.1, and the last is the LED Id (ranging between 0 and 7). Both thermal storage and thermo-electrical ageing have been performed in climatic chambers. The electrical ageing has been performed by means of dc current driver designed to meet ageing needs.

As mentioned before, the junction temperature of the 8-LEDs series biased together is higher than the temperature of the single device. In addition, the heat convection characteristics of climatic chamber used for ageing are different; thus a different approach was used for temperature estimation. The LEDs have been inserted in the climatic chamber and biased at current level that can guarantee a certain amount of self-heating. The forward voltage measured in steady state conditions (after 20 minutes since the thermal capacitance of the heat sink is high) was used to extrapolate the junction temperature from the thermal map obtained before. If the junction temperature measured was higher (lower) than desired level, the operation

| Character | Oven Temperature/Self heating |
|---|---|
| 0 | RT/0 |
| E | 20 °C |
| G | 40 °C |
| I | 60 °C |
| L | 80 °C |
| M | 100 °C |
| O | 120 °C |
| Q | 140 °C |
| S | 160 °C |
| U | 180 °C |
| Z | 200 °C |

*Table 5.1: Meaning of the characters used in the name coding of the devices.*

| **Code** | $T_j$ | $I_d$ | $T_{amb}$ | **Stress time** |
|---|---|---|---|---|
| B/WM0x | 100 °C | 0 mA | 100 °C | 4000 h |
| B/WO0x | 120 °C | 0 mA | 120 °C | 4000 h |
| B/WQ0x | 140 °C | 0 mA | 140 °C | 4000 h |
| B/WS0x | 160 °C | 0 mA | 160 °C | 3500 h |
| WS0bx | 160 °C | 0 mA | 160 °C | 2000 h |
| WU0x | 180 °C | 0 mA | 180 °C | 150 h |
| WU0bx | 180 °C | 0 mA | 180 °C | 1000 h |
| B/WZ0x | 200 °C | 0 mA | 200 °C | 64 h |
| B/W0nx | 70 °C | 700 mA | 20 °C | 4000 h |
| B/WQEx | 160 °C | 300 mA | 140 °C | 500 h |
| B/WOGx | 160 °C | 700 mA | 120 °C | 1500 h |
| B/WMIx | 160 °C | 900 mA | 100 °C | 1250 h |
| B/W0Qx | 160 °C | 1200 mA | 20 °C | 64 h |

*Table 5.2: Stress status details*

would be repeated at lower (higher) current level until the target temperature was reached.

### 5.3.2 Thermal Storage Results

In the following the results of thermal storage session are reported. Firstly the optical, chromatic and electrical results are presented. Furthermore, an analysis on optical results is provided, and the estimation of degradation model is proposed.

**Optical Results** In Fig. 5.5-5.10 the optical results of devices submitted to thermal storage have been reported. For each figure we have reported: (a) the normalized lumen decay, (b) the B/W ratio, (c) the normalized integral of the blue peak for white LEDs, and (d) for pure blue LEDs. Each plot reports all samples and the average. All the data have been obtained by EL spectra collected at 350 mA during stress.

The first results is the luminous flux decay. Devices submitted to stress show a roughly

exponential kinetic, with a degradation rate dependent on the temperature level. The data of lumen decay have been used to extrapolate a degradation model, that will be provided afterwards. It is worth noticing that the total stress time are not the same for every ageing session, and the values of the Time To Failure (TTF) are not always available.

The B/W ratio give some information useful for degradation mechanism evaluation. The behaviour of the B/W ratio is quite different from lumen decay: the thermal storage implied an increase of the ratio that seems to be thermally activated. However, the activation energy of such process seems to be higher than the energy of lumen decay process. This is underlined by the degradation amount showed in Fig. 5.5(b) (storage at 100 °C) and Fig. 5.10(b) (storage at 200 °C): while for 100 °C storage the B/W ratio did not change, the increase for 200 °C storage was prominent yet after first hours of stress.

The last parameter monitored during ageing was the integral of blue peak for both white and blue LEDs. The comparison between peak kinetics of blue and white LEDs can give useful information on the amount of the blue degradation that contributes to overall luminous flux decay. From the figures it could be noticed that the decrease of the blue peak during stress is similar in blue and white LEDs: this means that the degradation mechanism related to blue peak decay is not correlated with phosphors presence.

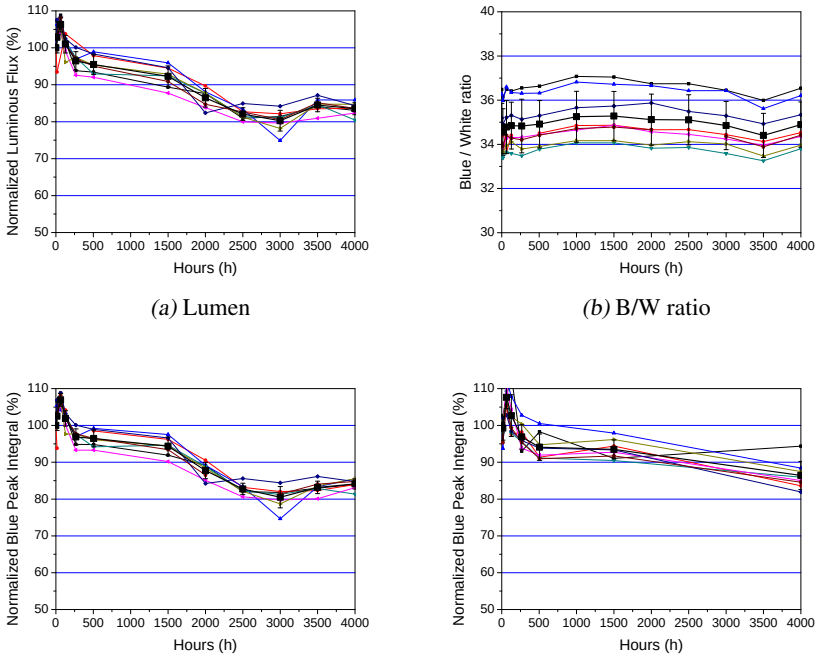


*(a)* Lumen *(b)* B/W ratio

*(c)* Blue Power (White LEDs) *(d)* Blue Power (Blue LEDs)

*Figure 5.5: Optical results of B/WM0 LEDs: (a) normalized lumen decay, (b) Blue vs. White ratio, and normalized integral of blue peak for LEDs (c) with and (d) without yellow phosphors.*

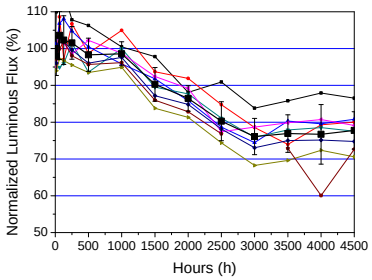


*(a)* Lumen

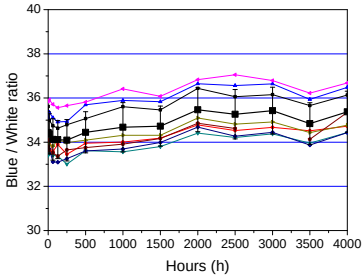


*(b)* B/W ratio

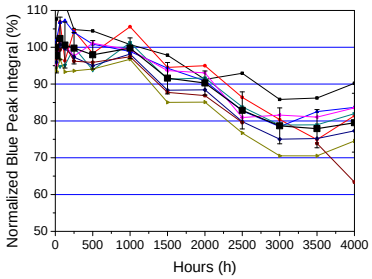


*(c)* Blue Power (White LEDs)

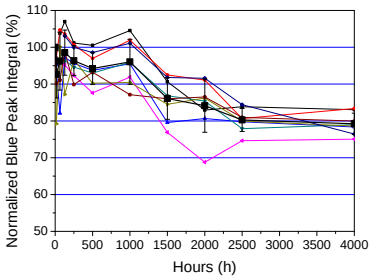


*(d)* Blue Power (Blue LEDs)

*Figure 5.6: Optical results of B/WO0 LEDs: (a) normalized lumen decay, (b) Blue vs. White ratio, and normalized integral of blue peak for LEDs (c) with and (d) without yellow phosphors.*

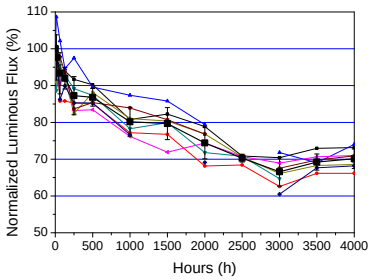


*(a)* Lumen

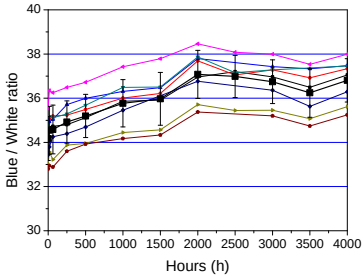


*(b)* B/W ratio

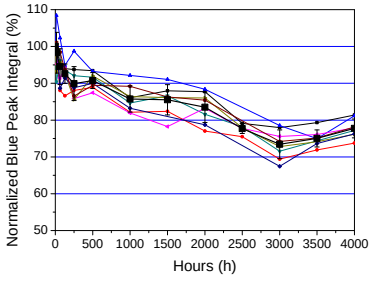


*(c)* Blue Power (White LEDs)

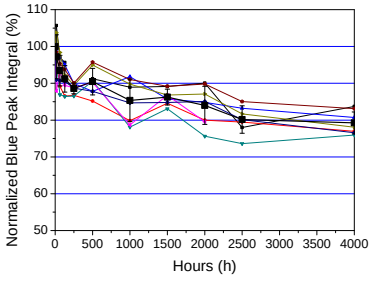


*(d)* Blue Power (Blue LEDs)

*Figure 5.7: Optical results of B/WQ0 LEDs: (a) normalized lumen decay, (b) Blue vs. White ratio, and normalized integral of blue peak for LEDs (c) with and (d) without yellow phosphors.*

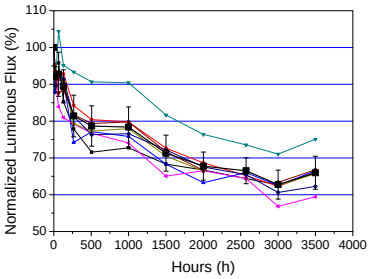


*(a)* Lumen

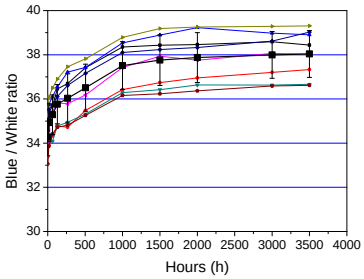


*(b)* B/W ratio

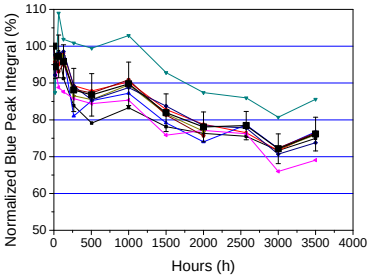


*(c)* Blue Power (White LEDs)

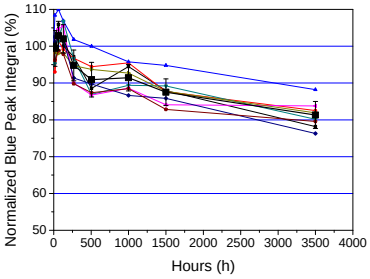


*(d)* Blue Power (Blue LEDs)

*Figure 5.8: Optical results of B/WS0 LEDs: (a) normalized lumen decay, (b) Blue vs. White ratio, and normalized integral of blue peak for LEDs (c) with and (d) without yellow phosphors.*

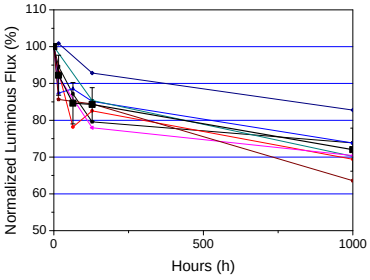


*(a)* Lumen

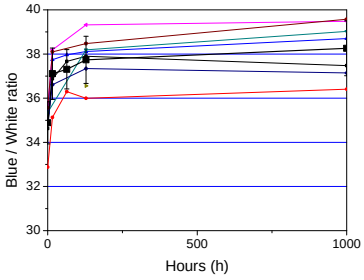


*(b)* B/W ratio

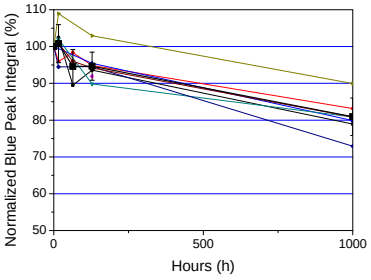


*(c)* Blue Power (White LEDs)

*Figure 5.9: Optical results of WU0 LEDs: (a) normalized lumen decay, (b) Blue vs. White ratio, and normalized integral of blue peak for LEDs (c) with yellow phosphors.*

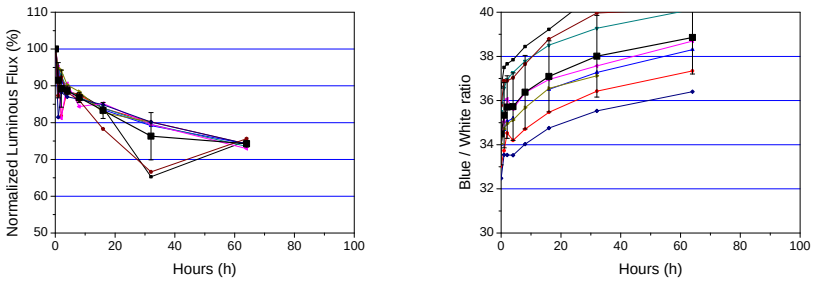


*(a)* Lumen *(b)* B/W ratio

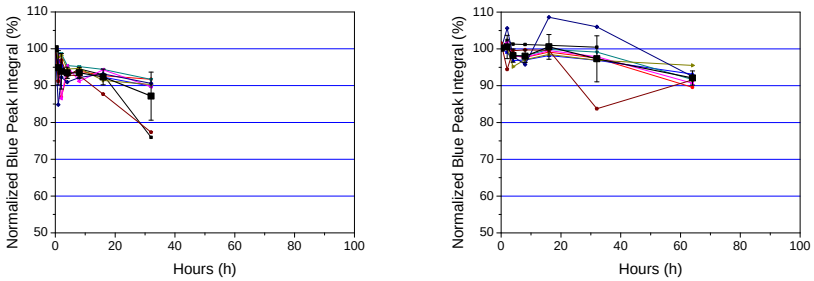


*(c)* Blue Power (White LEDs) *(d)* Blue Power (Blue LEDs)

*Figure 5.10: Optical results of B/WZ0 LEDs: (a) normalized lumen decay, (b) Blue vs. White ratio, and normalized integral of blue peak for LEDs (c) with and (d) without yellow phosphors.*

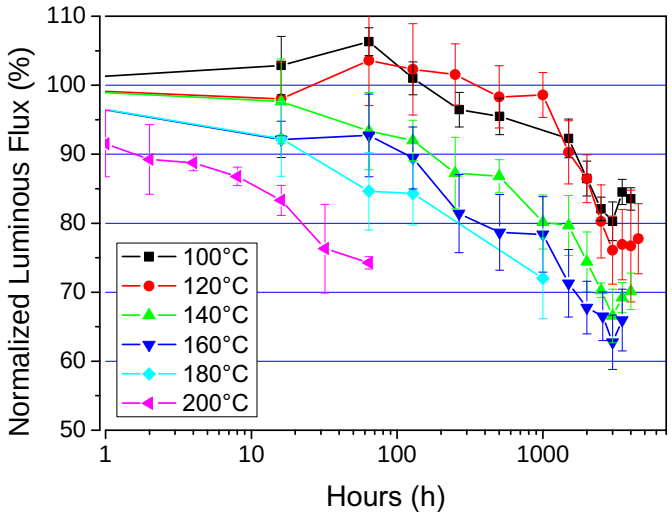


*Figure 5.11: Overview of the average lumen decay at different storage temperature levels.*

**Chromatic Results** The EL spectra measured at $350\ \mathrm{mA}$ were used to extrapolate the CIE 1931 X and Y values. The method employed for extrapolation has been described in 4.3.3. The resulting chromatic spaces have been reported in Fig. 5.12. The same data have been reported in Fig. 5.13 for direct comparison between the different ageing sessions.

The thermal storage implied a decrease in X and Y components: in chromatic terms, we assisted to a blue-shift. The X and Y decrease was found to be thermally activated, with a more enhanced degradation at harsher conditions. This degradation mechanism can be easily related to the B/W Ratio increase reported before: an increase in the output blue radiation worsen the overall chromatic properties of the device. However, the chromatic shift shown in Fig. 5.12 is not high enough to exit from the bin provided by the manufacturer. This means that the degradation is not detectable by the eye sensitivity.

The degradation mechanism responsible for chromatic shift is related to the worsening of optical properties of the encapsulation or a degradation of phosphors efficiency. The latter seems to be not relevant since the stability of phosphors at high temperatures has been widely demonstrated [44, 43]. In addition, the shift in X,Y have the same slope for the different ageing conditions. This slope is given by the yellow and blue points in CIE map. This means that no modifications in blue and yellow dominant wavelength are present, that is a uniform worsening of transmittance properties of the encapsulation.

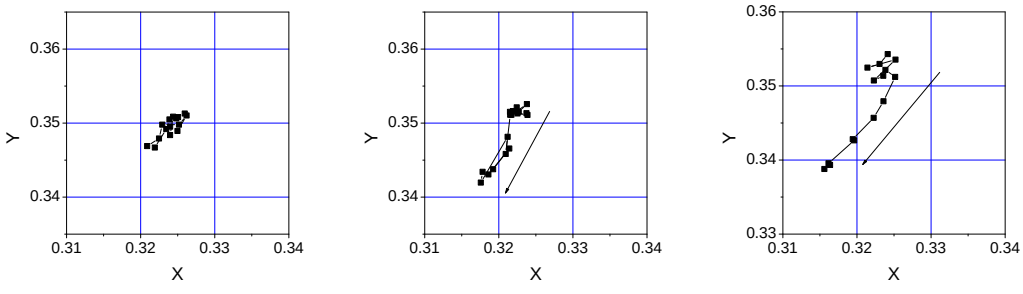


*(a)* WM0 (100 °C) *(b)* WO0 (120 °C) *(c)* WQ0 (140 °C)

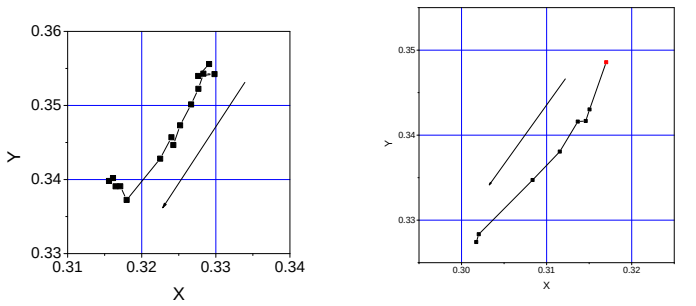


*(d)* WS0 (160 °C) *(e)* WZ0 (200 °C)

*Figure 5.12: CIE $X, Y$ values of samples submitted to thermal storage. The X and Y scales are the same for each plot.*

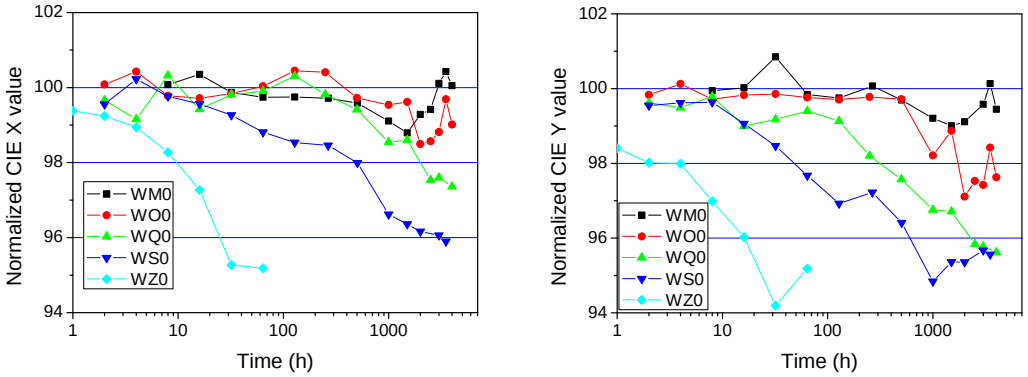


*(a)* CIE X *(b)* CIE Y

*Figure 5.13: Comparison of CIE $X, Y$ values during thermal storage at different temperature levels.*

**Electrical Results** The last parameters used to evaluate the degradation of LEDs were the electrical characteristics. In Fig. 5.14-5.18 the I-V plots before and after thermal storage are provided. The data have been collected by means of HP 4155 Parameter Analyzer. As can be noticed from the figure, no modifications have been detected during ageing, nor in white samples, neither in blue ones. This result indicates

- a good stability of ohmic contacts (current slope remained unchanged in the forward voltage region);
- the absence of defect migration/generation process (current in reverse voltage region and forward generation/recombination region did non increase).

Since the degradation in efficiency of GaN LEDs is related to I-V characteristics modifications [68, 71], we supposed that the blue output degradation was not related to a real decrease in efficiency of the GaN LEDs.

The last results to take into account is the degradation detected for devices aged at 200 °C (Fig. 5.18). In this case, a contained increase of current in reverse voltage region may indicate a degradation of the blue chip, due to defect migration activated by high temperatures. However, this temperature represents an exception, really far from operative conditions.

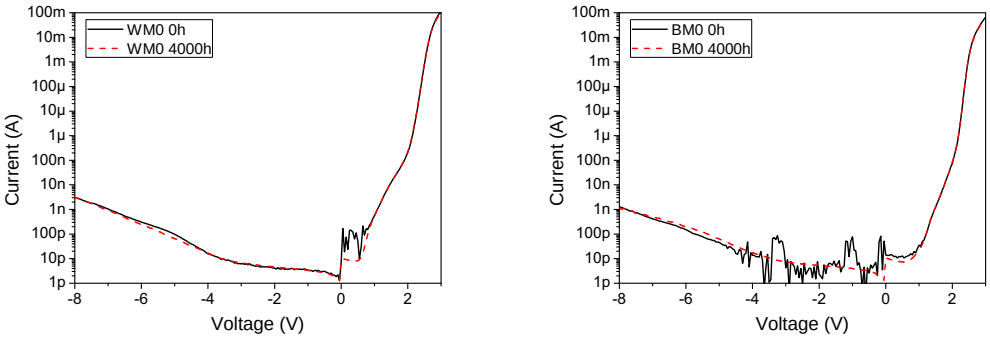


*(a)* WM0 (100 °C) *(b)* BM0 (100 °C)

*Figure 5.14: Semi-log plot of Current vs. Voltage characteristics before and after stress on (a) White and (b) Blue LEDs.*

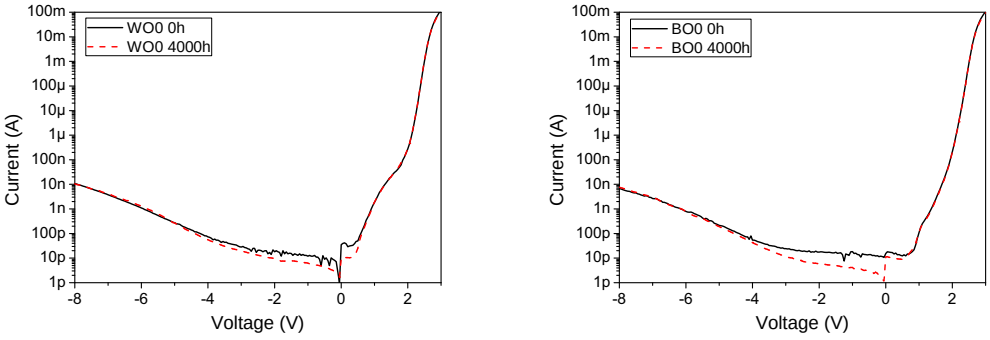


*(a)* WO0 (120 °C) *(b)* BO0 (120 °C)

*Figure 5.15: Semi-log plot of Current vs. Voltage characteristics before and after stress on (a) White and (b) Blue LEDs.*

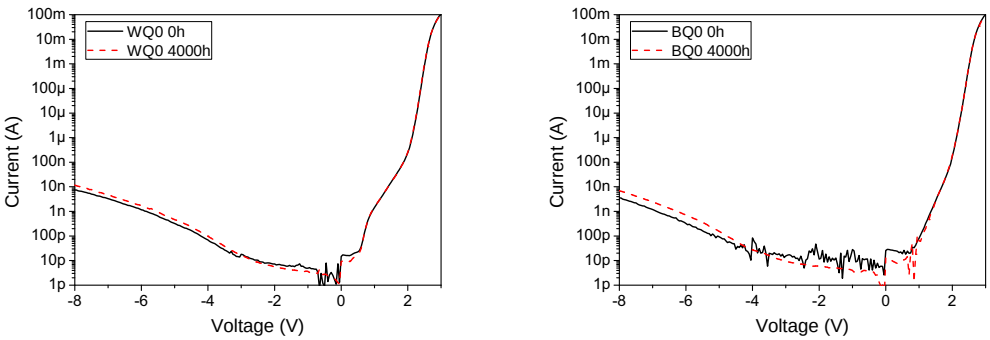


*(a)* WQ0 (140 °C) *(b)* BQ0 (140 °C)

*Figure 5.16: Semi-log plot of Current vs. Voltage characteristics before and after stress on (a) White and (b) Blue LEDs.*

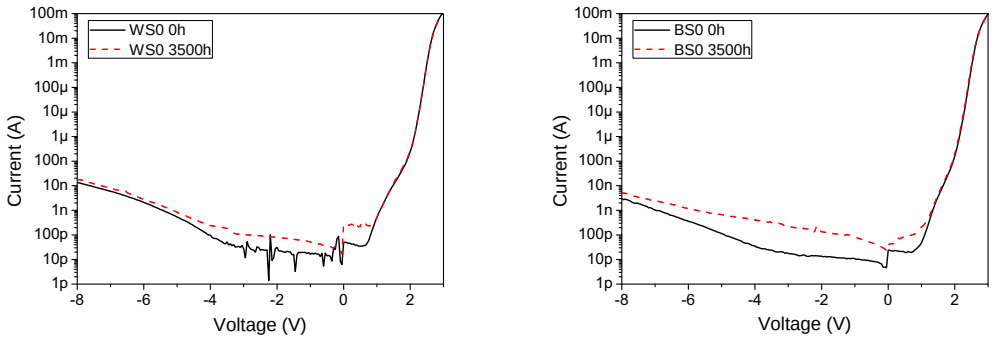


*(a)* WS0 (160 °C) *(b)* BS0 (160 °C)

*Figure 5.17: Semi-log plot of Current vs. Voltage characteristics before and after stress on (a) White and (b) Blue LEDs.*

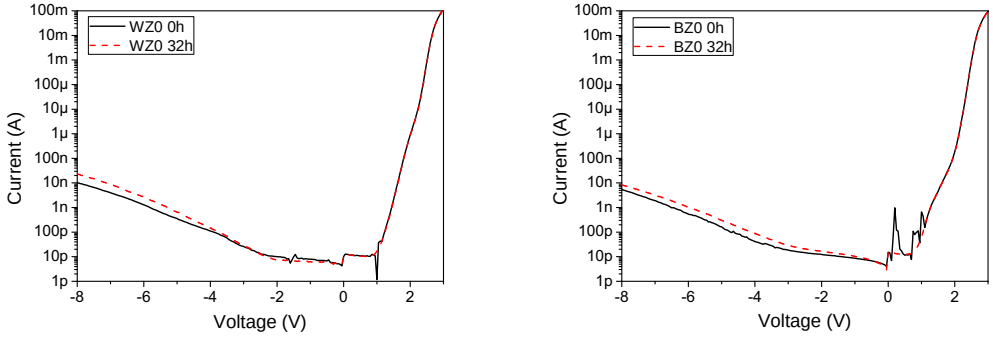


*(a)* WZ0 (200 °C) *(b)* BZ0 (200 °C)

*Figure 5.18: Semi-log plot of Current vs. Voltage characteristics before and after stress on (a) White and (b) Blue LEDs.*

**Emission Microscopy results** In order to understand the role of the lens and the chip in the degradation of LEDs, several preliminary optical measurements have been performed on untreated and aged devices. The following procedure has been followed: (1) the integrated optical power of several untreated blue devices and aged at 160 °C has been measured by emission microscope (see chapt. 4 for details); (2) the encapsulation of these LEDs have been removed, together with their bonding wires; (3) the LEDs have been contacted by means of micro-probes and their emission has been collected. The results of this process have been reported in Fig. 5.19. As can be noticed the aged devices with encapsulation manifested a 10% of loss compared to untreated devices (as reported by optical power measurements). However, the situation after encapsulation detachment is quite different: the aged devices show a higher emission than the untreated ones. This means that the main responsible for LEDs degradation must be sought in the encapsulation, since the chip did not manifest any degradation. The fact that the emission without lens is higher for aged samples means that the starting optical power of devices was higher than the emission of untreated samples reported in Fig. 5.19. The results from this preliminary investigation confirm the fact that the chip is not involved in the degradation process: however, an improvement of the process must be applied, repeating the measurement for a wider set of LEDs and using different techniques that can investigate the transmittance properties of the encapsulation during stress.

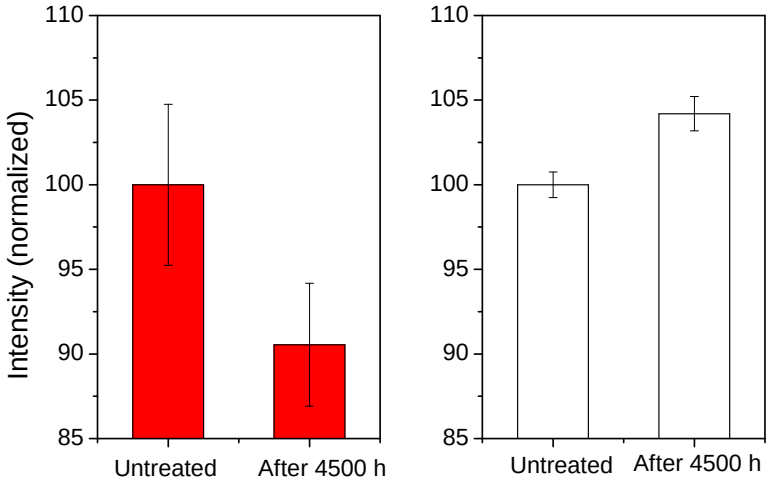


*Figure 5.19: The average values of the normalized luminous intensity measured on untreated and aged (160 °C) blue samples (a) with lens, and (b) after lens detachment, measured my means of emission microscope. The samples have been contacted by micro-probes, since the lens detachment implied the breaking of the bonding wires.*

**Degradation Model** The data collected by means of optical characterization have been used to perform an analysis that aimed at finding the degradation mechanism related to the thermal storage. The comparison between different parameters (lumen decay, blue peak decrease, B/W Ratio increase) gives the opportunity to find the physical process responsible for the degradation.

The analysis started from the luminous flux decay of white LEDs. A failure criterion of 15% of loss has been chosen, since all devices reached that limit at this stage of ageing. The TTF of luminous flux have been extrapolated by means of exponential fitting of curves in Fig. 5.5-5.10 and reported in the Arrhenius plot in Fig. 5.20 (squares). As can be noticed, the process is thermally activated for junction temperature levels above 120 °C. The linear fitting of the data provided the degradation mechanism parameters, according to the Arrhenius equation reported at pag. 63. The results have been reported in the Tab. 5.3. Concerning the temperature range of $100 - 120$ °C, we may infer that the activation energy of the degradation process is low: we did not extrapolated the analytical value since a linear fit on a set of two data is not statistically relevant. This means that two degradation processes are acting: (i) a thermally activated process in higher temperature range, and (ii) a slower degradation process in the lower temperature range.

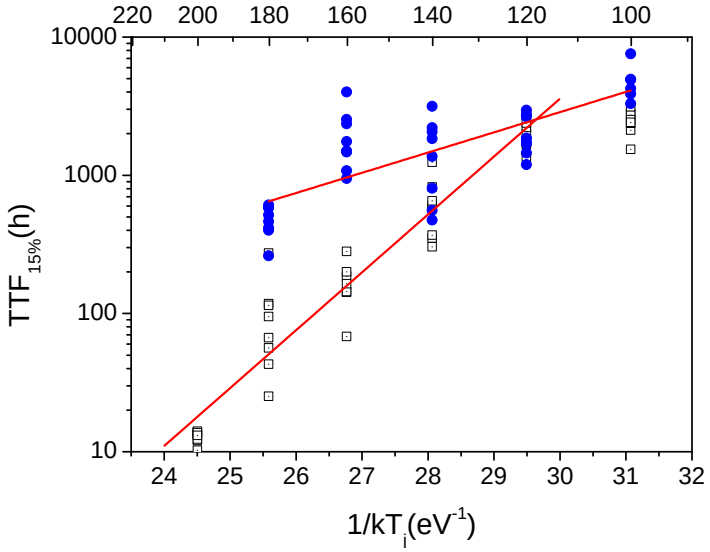


*(a)*

*Figure 5.20: Arrhenius plot of Time To Failure of 15% loss in luminous flux of blue LEDs (circles) and 15% loss in optical power of blue LEDs (squares). The figure also includes the linear fitting of the data.*

| Parameter | Slope(meV) | Intercept(ln(h)) |
|---|---|---|
| $TTF_{15\%}$ lumen ($T_j \leq 120$ °C) | $964 \pm 47$ | $-20.74 \pm 1.26$ |
| $TTF_{15\%}$ blue power | $337 \pm 48$ | $-2.14 \pm 1.35$ |

*Table 5.3: Parameters of linear fitting of data in Fig. 5.20.*

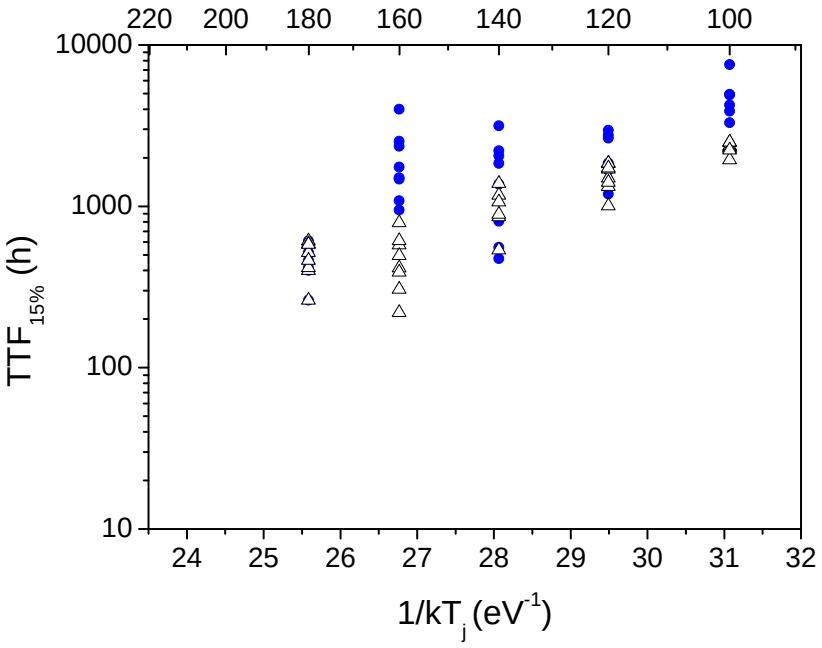


*(a)*

*Figure 5.21: Arrhenius plot of Time To Failure of 15% loss in optical power of blue LEDs (circles) and of blue emission of white LEDs (triangles).*

Before discussing the results, we provide the analysis on the optical power loss of blue LEDs. Since the degradation of the blue peak was similar for white and blue LEDs (see Fig. 5.21 for comparison), we used the data from blue LEDs in order to obtain a degradation law of such parameters. As can be noticed, the trend is unique in the whole temperature range, indicating the presence of one degradation mechanism. The activation energy of this degradation process was found to be $337\ \mathrm{meV}$.

The results can be summarized:

- the blue peak decay shows a single degradation mechanism with activation energy of $337\ \mathrm{meV}$;
- the blue peak devay is similar both for blue and white LEDs;
- the lumen decay shows two slopes in the Arrhenius plot: one thermally activated in the higher temperature range ($964\ \mathrm{meV}$), and one at lower temperature levels;
- the lumen parameter takes into account of both the blue and yellow peak: at higher temperatures it pays the consequences of blue decay and yellow decay vs. overall emission.

This lifetime analysis provided several important results, above all:

1. the degradation of the blue emission of white LEDs is similar to the optical power decay of blue LEDs, indicating the phosphors and the phosphors+glue mixture as responsible for degradation in the high temperatures range;

2. the activation energy of the blue decay is correlated to the degradation of white LEDs in lower temperatures range: the activation energy of $337\ \mathrm{meV}$, is similar to other reliability works on LEDs [45, 66] and could be used for lifetime estimation of white LEDs.

3. any accelerated lifetime testing in the temperature range beyond $120\ ^{\circ}\mathrm{C}$ must be avoided since the process found are not correlated with the process present in nominal condition;

4. the present data on degradation of encapsulation (white LEDs) could be compared with reliability data on improved structures and materials: since the activation energy of the degradation process in high temperatures range is high, the comparison could be performed in that range for faster results.

### 5.3.3 Electro-Thermal Ageing Results

In the following, the results on electro-thermal stress will be provided. The stress was carried out aiming at finding a possible correlation between current density and degradation rate. In order to avoid the effects of self-heating (see previous section) and to preserve the acceleration conditions, a constant junction temperature of $160\ ^{\circ}\mathrm{C}$ has been used. In order to implement this model, the electrical ageing have been performed in climatic chambers at $25, 100, 120\ ^{\circ}\mathrm{C}$, an the current was chosen in order to obtain the desired junction temperature. The current levels were, respectively, $1200, 900, 700\ \mathrm{mA}$, that corresponds to current densities of $120, 90, 70\ \mathrm{A/cm^2}$. In addition, a stress at nominal conditions (RT, $700\ \mathrm{mA}$) has been performed.

**Optical Results** In Fig. 5.22-5.25 the optical results in terms of luminous flux, B/Y Ratio and blue peak have been reported. With respect to thermal aged devices, different considerations must be addressed. Firstly, the lumen degradation is not observable for all devices since the stress is at an early stage. However, a general exponential trend can be recognized. Samples aged at $700\ \mathrm{mA}$ (Fig. 5.23) and at $900\ \mathrm{mA}$ (Fig. 5.24) showed respectively an increase on the standard deviation of the average after 500 hours and a strong decrease after 128 hours. These facts are consequences of the same process found during stress on white LEDs. On several samples, the encapsulation suddenly exhibited a crack, and a consequent luminous degradation. This mechanism was ascribed to the mechanical stress of the lens, originated by the high temperature gradient between the surface of the chip (high current, high temperature) and the surrounding ambient temperature. In addition, the effect was detected only in white LEDs. This means that the silicon of the encapsulation have a lower tensile strength when the phosphors are included.

The B/W ratio results give additional information. In general, we assisted to an early decrease of the ratio (Fig. 5.25, followed by an increase similar to thermal storage case. This characteristic will be examined in chromatic results section.

Finally, the comparison between luminous flux decay among each stress conditions has been reported in Fig. 5.26. In the figure was also plotted the degradation kinetic at $160\ ^{\circ}\mathrm{C}$ storage for comparison (the junction temperature during electrical stress is about $160\ ^{\circ}\mathrm{C}$). We can stress two interesting results from this figure. Firstly, in the semilog plot, the degradation

after 250 hours is different for each ageing conditions: it's interesting to notice that the first cracks in the encapsulation started to compare around the 250 hours of ageing. The second results can be found looking to the linear plot: before 250 hours the degradation was almost similar for all samples, indicating the degradation is dependent on the junction temperature, and not on different current levels.

Also in this case, the results from optical characterization will be used in the lifetime analysis for the degradation model estimation.

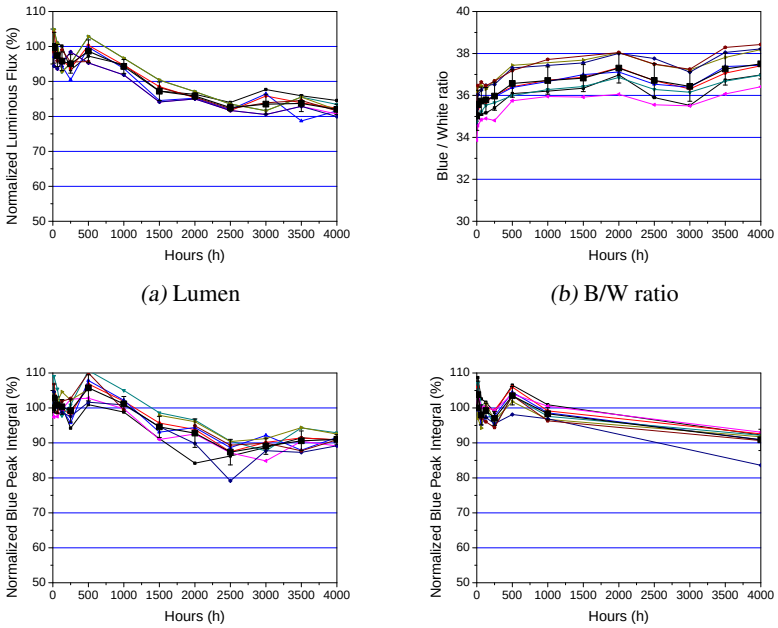


*(a)* Lumen *(b)* B/W ratio

*(c)* Blue Power (White LEDs) *(d)* Blue Power (Blue LEDs)

*Figure 5.22: Optical results of B/W0n LEDs: (a) normalized lumen decay, (b) Blue vs. White ratio, and normalized integral of blue peak for LEDs (c) with and (d) without yellow phosphors.*

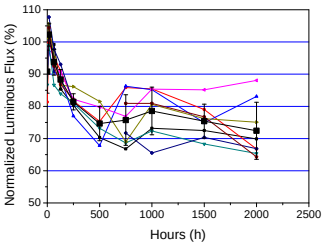


(a) Lumen

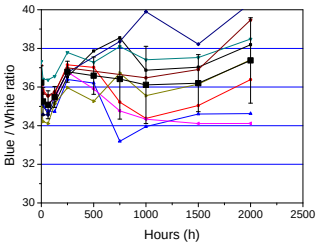


(b) B/W ratio

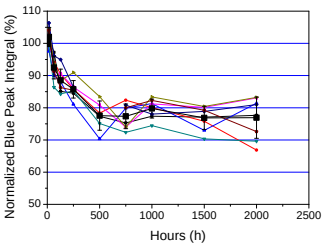


(c) Blue Power (White LEDs)

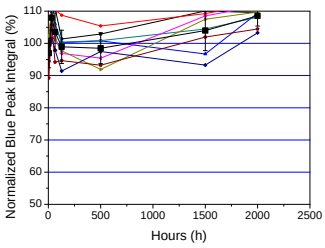


(d) Blue Power (Blue LEDs)

*Figure 5.23: Optical results of B/WOG LEDs: (a) normalized lumen decay, (b) Blue vs. White ratio, and normalized integral of blue peak for LEDs (c) with and (d) without yellow phosphors.*

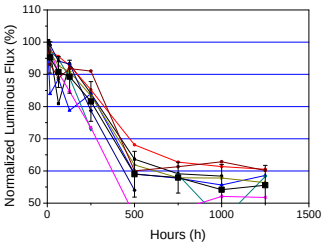


(a) Lumen

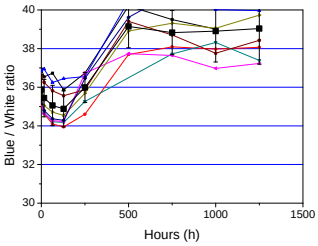


(b) B/W ratio

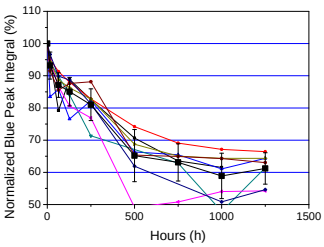


(c) Blue Power (White LEDs)

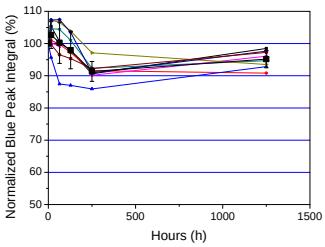


(d) Blue Power (Blue LEDs)

*Figure 5.24: Optical results of B/WMI LEDs: (a) normalized lumen decay, (b) Blue vs. White ratio, and normalized integral of blue peak for LEDs (c) with and (d) without yellow phosphors.*

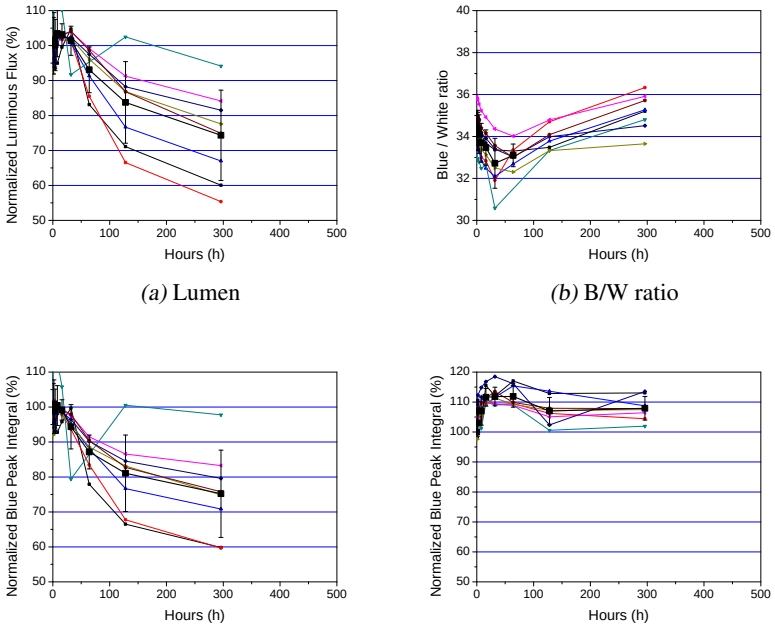


*(a)* Lumen *(b)* B/W ratio

*(c)* Blue Power (White LEDs) *(d)* Blue Power (Blue LEDs)

*Figure 5.25: Optical results of B/W0Q LEDs: (a) normalized lumen decay, (b) Blue vs. White ratio, and normalized integral of blue peak for LEDs (c) with and (d) without yellow phosphors.*

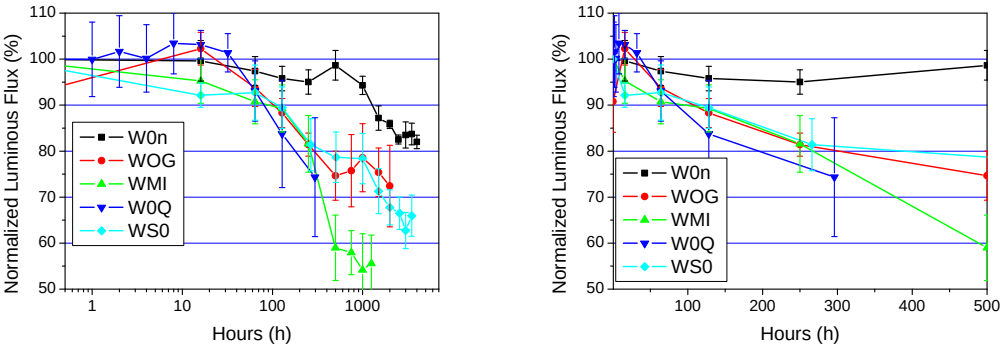


*(a)* *(b)*

*Figure 5.26: Overview of the average lumen decay at different ageing conditions in (a) semilog and (b) linear scale.*

**Chromatic Results** The CIE X,Y values have been extrapolated and reported in the color space in Fig. 5.27, and for comparison in Fig. 5.28. Looking to the latter figure, it's clear that the spectral shift is not monotonic as was observed for thermal stressed devices. While during first hours of stress the X and Y values tend to increase (especially for devices aged at RT, 1200 mA), a second process induce a decrease in both X,Y values. Finally, the values return to increase. This is clearly visible for Y values, where the three-slopes kinetics are activated by the stress current.

These results can be commented with a few hypothesis:

- the blue chip emission is not constant during stress and may influence the chromatic properties;
- the blue emission, especially for higher current densities, may induce a degradation in lens transmittance properties due to the UV component of the blue peak tail;
- the local high temperature gradient may worsen the optical properties of the silicon around the junction and the efficiency of the surrounding phosphors.

Since the kinetics are complicated, we only provided hypothesis on degradation mechanism.

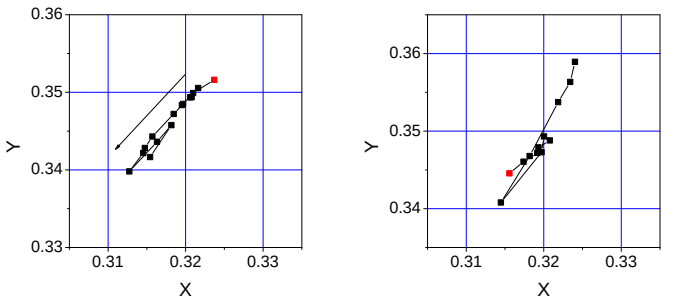


*(a)* 20 °C, 700 mA




*(b)* 120 °C, 700 mA

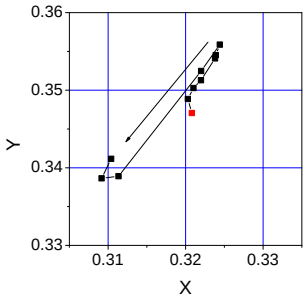


*(c)* 100 °C, 900 mA

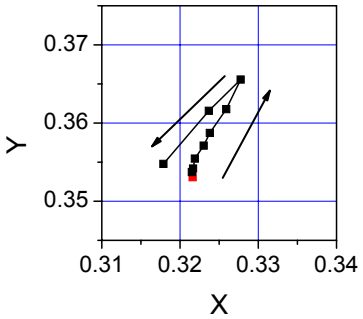


*(d)* 20 °C, 1250 mA

*Figure 5.27: $CIEX,Y$ values of samples submitted to electro-thermal storage; the red squares represent $X,Y$ values before stress.*

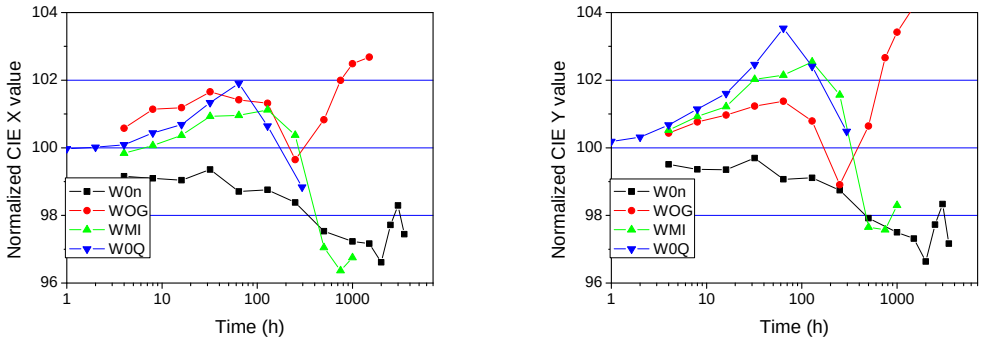


*(a)* CIE X *(b)* CIE Y

*Figure 5.28: Comparison of $CIEX,Y$ values during thermal storage at different temperature and bias levels.*

**Electrical Results** In comparison with thermal storage results, the electrical characteristics of electrically-treated devices are very different. In Fig. 5.29-5.32 the I-V characteristics in semi-log scale of devices before and during stress are reported. While the characteristics in forward voltage region remained almost unchanged, a great increase in reverse current was detected. In first approximation, the amount of current increase is proportional to the current density.

This modification is the fingerprint of a process of generation/migration of defects in the active/bulk region [71, 72]. However, since no degradation in luminous efficiency in blue LEDs has detected, we supposed that the increase of dislocation density was localized in the bulk region. An other hypothesis could be the activation of passive magnesium at the p-side, corresponding to the initial luminous increase detected in all samples electrically aged.

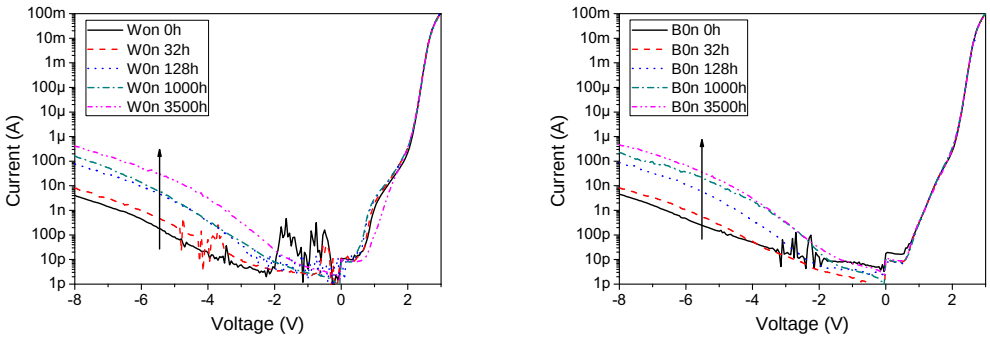


*(a)* W0n (20 °C, 700 mA) *(b)* B0n (20 °C, 700 mA)

*Figure 5.29: Semi-log plot of Current vs. Voltage characteristics during stress on (a) White and (b) Blue LEDs.*

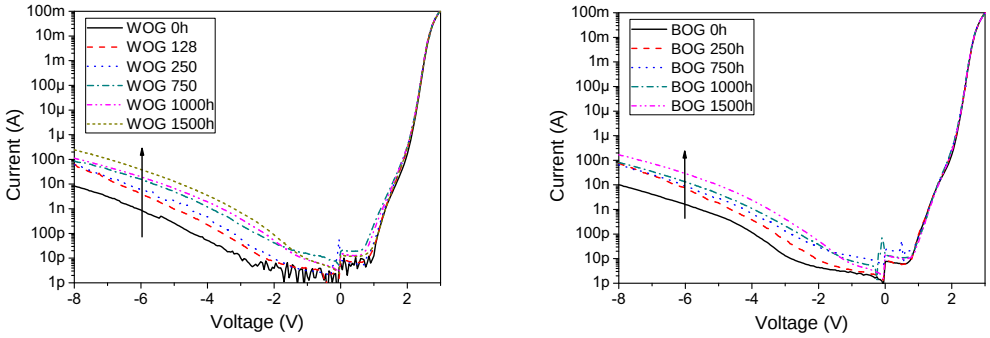


*(a)* WOG (120 °C, 700 mA) *(b)* BOG (120 °C, 700 mA)

*Figure 5.30: Semi-log plot of Current vs. Voltage characteristics during stress on (a) White and (b) Blue LEDs.*

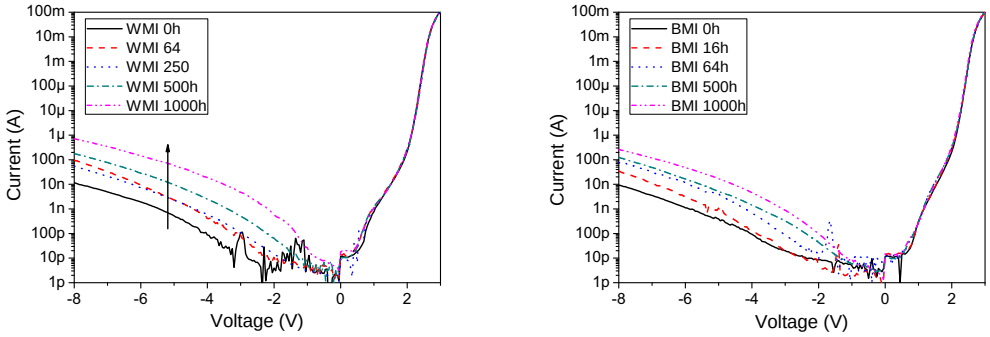


*(a)* WMI (100 °C, 900 mA) *(b)* BMI (100 °C, 900 mA)

*Figure 5.31: Semi-log plot of Current vs. Voltage characteristics during stress on (a) White and (b) Blue LEDs.*

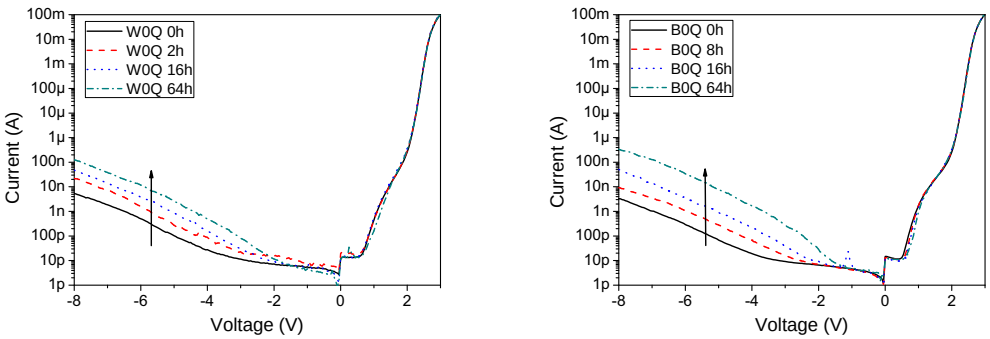


*(a)* W0Q (20 °C, 1250 mA) *(b)* B0Q (100 °C, 1250 mA)

*Figure 5.32: Semi-log plot of Current vs. Voltage characteristics during stress on (a) White and (b) Blue LEDs.*

**Degradation Model** The results from optical analysis have been used for extrapolation of the degradation model. In order to find an analytical correlation between stress current and degradation, the TTF at 15% of luminous flux as been extrapolated for each series of LEDs. The data collected have been plotted versus the stress current, and reported in Fig. 5.33.

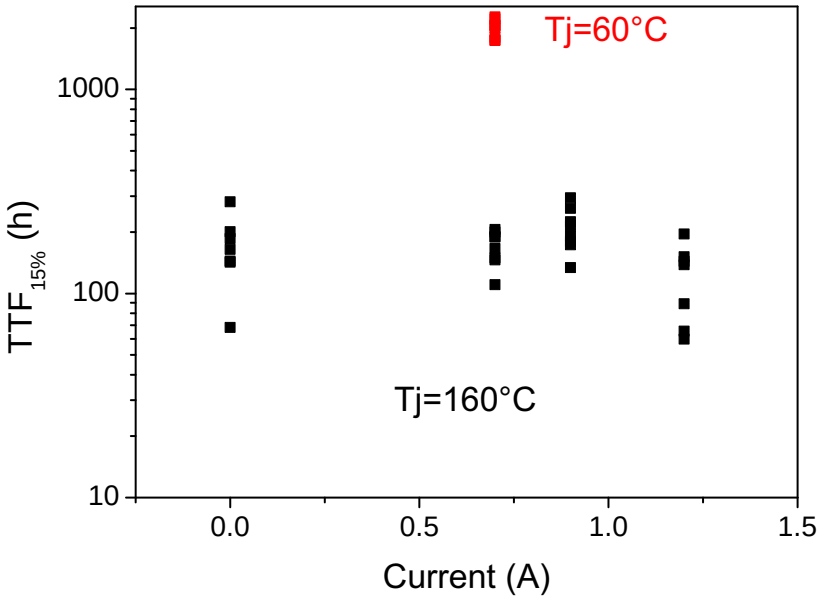


*Figure 5.33: Time To Failure of 15% flux loss in electro-thermally aged devices vs. injected current. The results have been compared to degradation induced by pure iso-thermal storage at* $160\ ^{\circ}\mathrm{C}$*. The red squares indicate the degradation of LEDs aged at nominal conditions (*$700\ \mathrm{mA}$*, RT).*

In the figure have been reported also the results of iso-thermal storage at $160\ ^{\circ}\mathrm{C}$ and at nominal conditions $700\ \mathrm{mA}$. As can be noticed, it is not possible to individuate a dependence between degradation at constant junction temperature and current. This imply that the main responsible for degradation is the heat generated by the device. It's important to notice that the TTF at 15% is earlyer than the generation of cracks on the encapsulation. This analysis does not take into account of these failure modes that limits the lifetime of the device and are roughly related to the current density of the devices. Since the cracks do not imply a parametric degradation, it's still impossible to extrapolate a degradation model of such process, and the analysis on temperature induced degradation reported before is the only approssimation valid for a lifetime prevision.

## 5.4 Conclusions

The reliability analysis work presented in this chapter provides relevant information on degradation mechanisms of white LEDs on Chip On Board technology. A set of 180 white and blue samples was submitted to an extensive thermal characterization and the subsequent combined electro-thermal lifetime analysis provided the following results:

- the technique used for fast thermal characterization can be time-saving when dealing with wide set of samples;
- the luminous flux degradation is activated by temperature and density current;
- we found degradation mechanisms related to different physical process; (encapsulation properties worsening, decrease in phosphors conversion efficiency, etc.)
- the analysis revealed that the presence of different activation energy in different temperature ranges may lead to overrate the LEDs lifetime;
- the blue GaN based chip showed a good stability during operation at accelerated conditions.

An intrinsic result of this analysis is represented by the experimental setup, that permitted to obtain detailed information during ageing on several physical quantities (spectra, I-V, thermal resistance) on a large set of devices, giving the statistical approach of a reliability work on high brightness LEDs not yet described in the literature.

However, the most important result is given by the long lifetime provided by COB LEDs presented in this chapter, even under critical environmental conditions.

# Chapter 6

# Deep-UV emitting diode: an alternative solution for SSL

*The chapter provides an overview of the technology and reliability of AlGaN based LEDs emitting in the Deep UV region (DUV). The electrical and optical characteristics of devices emitting at different wavelength are presented, focusing in particular on EL spectra and recombination mechanism analysis. The second part of the chapter provides an analysis of failure mechanism detected during electrical stress of DUV.*

## 6.1 Outline and specific goals

The recent progresses in high quality AlGaN-based hetero-structures make possible the demonstration of LED emitting in Deep UV region. Since the potential application field of such devices is very wide, it's fundamental to reach lifetimes longer than the kilo-hours limit. Despite the international research community is focusing its attention on the growth of high efficiency DUV LEDs [73, 74], very few works has been done on reliability and degradation process identification [13, 75, 76]. The main research activity presented in this chapter is the lifetime analysis and degradation mechanisms identification, capable of fill the actual lack in knowledge of physical processes responsible for the degradation of AlGaN-based LEDs.

In particular the work was subdivided in several steps:

1. an in-depth optical and electrical characterization of AlGaN based LEDs emitting in $247 - 310$ nm range, focusing on luminescence properties of devices investigated;
2. the lifetime testing at nominal operating conditions;
3. the analysis of the behaviour of different parameters (L-I, EL spectra, I-V, C-V);
4. the discussion on degradation process responsible for the luminous decay;
5. a failure analysis on not-emitting devices.

**Specific goals** The present work aimed at:

1. improving the comprehension of radiative and non-radiative recombination mechanisms in AlGaN based LEDs, on the basis of results available in the literature;

2. studying the impact of ageing at nominal operating conditions on optical and electrical properties of DUV LEDs emitting at different wavelengths;

3. identifying the degradation processes responsible for optical power decrease and finding a possible correlation with emitting wavelengths;

## 6.2 Deep UV application and LEDs

The Ultra-Violet emission is being widely used in present applications, ranging from illumination to biomedicine. The term Ultra Violet (UV) refers to the electromagnetic radiation in the wavelength range of $10 - 400$ nm. Since the UV band is very spread, several sub-bands have been created with a application-oriented classification. Such classification has been reported inFig. 6.1.

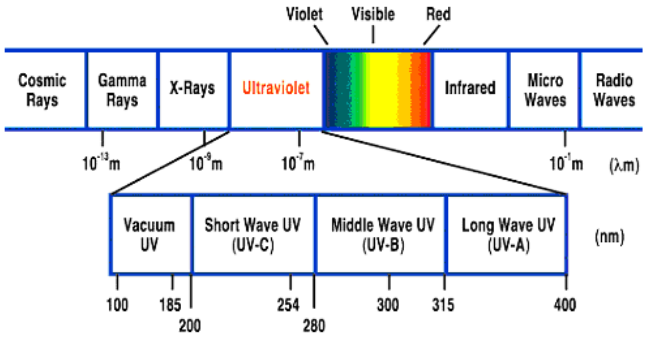


*Figure 6.1: Spectral classification of Ultra-Violet emission.*

### 6.2.1 Application of UV light

**UV-A,** $400 - 315$ nm Many kinds of adhesives, fluorescence, and other chemistries react to UV-A light. The applications working in UV-A band include:

- pumping emission for white light generation 2.2.3
- UV curing systems, UV coating/printing assemblies for PVC, film, glass materials
- Security products such as Bank note detectors, Bio-weapon Detectors, Crime scene inspection
- Phototheraphy devices to treat skin diseases
- Automotive leak detector, Food checking.

**UV-B,** $315 - 280\ \mathrm{nm}$ It has well known that UV-B light exposures can be hazardous to human eyes and skin, but also UV-B is assumed to be a beneficial to human health, since it produces vitamin D in the skin, and prevent skin cancer caused by inefficient UV-B exposure. The applications working in UV-B band include:

- Sterilization systems to purify water, surface, and air
- Analysis of Minerals
- EPROM Erasure

**UV-C,** $280 - 100\ \mathrm{nm}$ UV-C rays, also called as germicidal rays, are the highest energy, most dangerous type of ultraviolet light. With that energy, it destroys DNA & PNA in microorganisms such as bacteria, viruses & mold, Thus, it generates Ozone. Especially $254.7\ \mathrm{nm}$ is the most effective wavelength for disinfections.

### 6.2.2 UV light from LED

During last years, several factors permitted the development and the penetration in the market of UV LEDs:

- the recent progresses in the growth of high quality AlGaN layers and QWs;
- the introduction of ROHS EC regulations that avoids the use of mercury in electronic devices (mercury-based lamps is actually the main solution in UV light generation);
- the need of portable UV lamps for water sterilization coupled with the photovoltaic technologies.

Several research groups started to develop technologies and materials in order to grow devices emitting in Near and Deep UV (DUV). Currently, devices emitting at wavelength as low as $232\ \mathrm{nm}$ have been demonstrated [74, 73]. Furthermore, first devices emitting at $247\ \mathrm{nm}$ are commercially available.

Despite the excellent characteristics of these devices, their emission spectrum is characterized by the presence of one or more deep-level related emission bands [75], that indicate the presence of radiative paths that can compete with near band edge (NBE) emission in determining carriers recombination. It has been also indicated that the presence of these secondary emission bands can be problematic for bio-sensors applications, because they can interfere with the fluorescence signal of common bio-materials [13]. Therefore, a detailed analysis of the spectral features of DUV LEDs is an important tool for the evaluation of the quality of the devices, as well as for the understanding of carrier recombination dynamics in the active region. For this reason, the first part of this work presents the results of a complete analysis of the electroluminescence behavior of advanced DUV-LEDs.

Furthermore, only a little work on the reliability of these devices has been published so far [13, 9, 76]. While catastrophic degradation has been attributed to metal alloying at macroscopic defects in the p-layer [13], very little information has been reported on gradual degradation

of light output. However, a possible explanation of the mechanism responsible for gradual degradation has been provide by [76]. The authors suggest that the degradation mechanism is the diffusion of the Al atoms from p-AlInGaN cladding layer to the adjoining layers with a smaller Al mole fraction. This process induce (i) a lowering in potential barriers, (ii) a decrease in the concentration of carriers inside the active region and (iii) a current increase due to the increase of carriers passing the cladding layer. The fingerprint of the supposed diffusion process was the linear power decrease with the square root of ageing time.

## 6.3 Characterization

The analysis has been carried out on deep-ultraviolet LEDs of area $350\text{X}350\ \mu\text{m}^2$ ($1\text{X}1\ \text{mm}^2$ for L247). The structure consists of an n-AlGaN: Si cladding layer, an AlGaN multiple-quantum-well (MQW) layer, a p-AlGaN cladding layer, and a p-AlInGaN contact layer (see schematic inFig. 6.2. Details on devices structure can be found in [77]. The analyzed devices had emission wavelengths equal to $310, 295, 280, 265, 247\ \text{nm}$, depending on the aluminum molar fraction in the quantum wells. The samples will indicated with the emitting wavelength and the prefix L- (i.e. L295).

This kind of analysis has provided information on how the different radiative mechanisms compete for the recombination of electron-hole pairs.

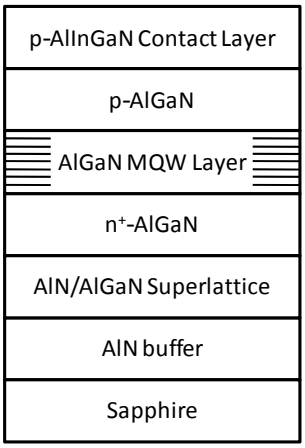


*Figure 6.2: Schematic structure of one analyzed DUV-LED.*

### 6.3.1 Thermal properties

The thermal resistance of the analyzed samples has been extrapolated by means of forward voltage methods 3.3.1. The thermal coefficient of L295 at $20\ \text{mA}$ is $-2.62\ \text{mV/K}$, in good agreement with other experimental data [52]. The thermal resistance extrapolated is about $240\ \text{K/W}$. With an input power of $110\ \text{mW}$, corresponding to a $20\ \text{mA}$ current, we obtain a self-heating of about $27\ ^\circ\text{C}$. This means that when operated at RT, the junction temperature of the device does not exceed $50\ ^\circ\text{C}$, well below the limit suggested by the manufacturer.

### 6.3.2 Spectral features

A detailed analysis on spectral profiles of several untreated samples has been performed in collaboration with the Dept. of Physics of the University of Parma. Samples L295 and L278 have been submitted to EL measurements by means of a monochromator.

The spectral profiles of untreated samples consist of an asymmetric main UV emission centered at about $4.46\ \mathrm{eV}$ (L278) and $4.2\ \mathrm{eV}$ (L295). The FWHM varies between 10 and $15\ \mathrm{nm}$, is in accordance with previously reported values [13], as shown in Fig. 6.3 for L278. The spectra of the analyzed devices showed interesting features: for both the series of LEDs, we have detected (i) a shoulder superimposed to the high-energy side of the main peak (at about $5\ \mathrm{eV}$ in Fig. 6.3, referred to as R band), likely related to the radiative emission from n-AlGaN layers; (ii) a shoulder superimposed to the low-energy side of the main peak (at about $5\ \mathrm{eV}$ in Fig. 6.3, referred to as L band, most probably relative to trap-assisted emission in the p-AlGaN layer;(iii) an emission band in the spectral range below $4\ \mathrm{eV}$ (band B in Fig. 6.3, previously attributed to radiative recombination through defects [75, 13].

Electron and holes injected into the LED active region only partially give light through the main band-to-band (UV) radiative recombination process. In fact, at the same time several other processes contribute to carriers recombination, including (i) non radiative recombination, (ii) radiative recombination through deep levels, (iii) electron/hole trapping, and (iv) carrier leakage out of the active region [75, 46]. Among these mechanisms, the relative weight of band-to-band and deep-level assisted transitions establishes the power-law dependence of the luminescence intensity vs current (L-I) curves [75]. In Tab. 6.1 the dependence of the Luminescence-intensity vs. current has been reported for recombination processes where band-to-band or trap-assisted mechanisms dominate.

*Table 6.1: Luminescence-Intensity dependence vs. current for different recombination mechanisms*

| Recombination | $L_{UV}$ | $L_B$ |
|---|---|---|
| band-to-band | $\propto I$ | $\propto I^{\frac{1}{2}}$ |
| trap-assisted | $\propto I^2$ | $\propto I$ |

We describe here the optical behavior of the LEDs emitting at $278\ \mathrm{nm}$ (with higher energy separation between UV and deep-level emission bands) and the factors affecting UV emission in as-received and aged samples.

Firstly, the effects of carrier overflow in the active region can be evaluated by analyzing the luminous intensity ratios $L_{UV}/L_L$ and $L_{UV}/L_R$ between the UV emission peak and each of two shoulder L and R, respectively related to trap-assisted emission in the p-AlGaN and to radiative recombination in n-AlGaN. In Fig. 6.4(a) the ratios are shown as a function of current: both the ratios present a well marked maximum at about $0.5\ \mathrm{mA}$ (R band) and $1\ \mathrm{mA}$ (L band), suggesting an increasing escape rate of carrier from the active layers at higher current levels. On the other hand, the ratio $L_{UV}/L_B$ between UV and B intensities shows an increasing trend up to a saturation at high currents.

In Fig. 6.4(b) the dependence of the intensity of the radiative emission bands on driving

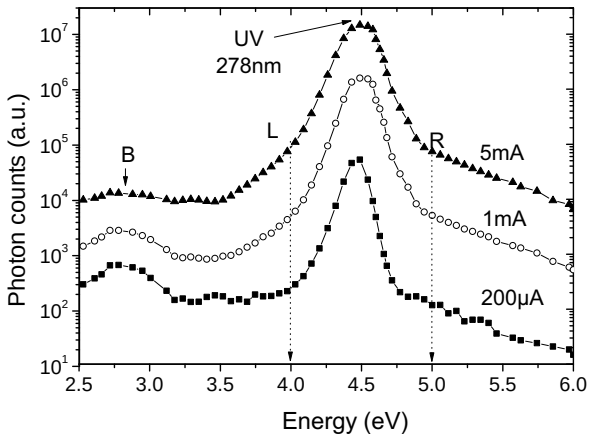


*Figure 6.3: EL spectra of one LED measured at three different current levels ($\lambda = 278$ nm).*

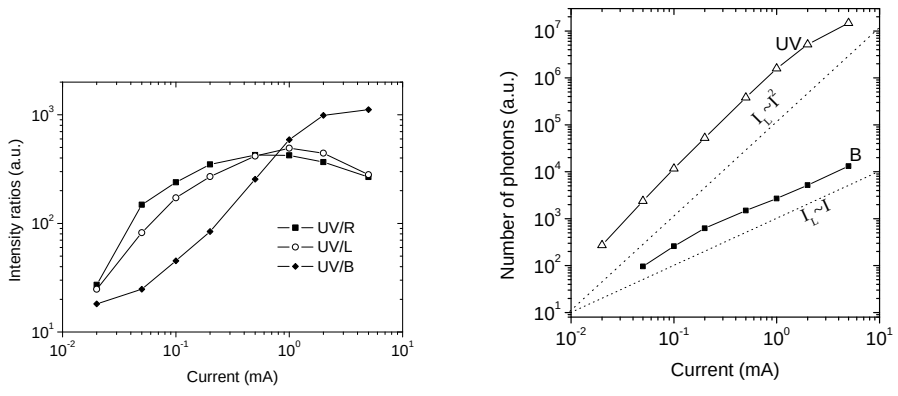


*(a)* *(b)*

*Figure 6.4: Analysis of EL spectra: (a) ratio between UV emission and L, R, and B bands, and (b) emission intensities for UV and B spectral components as a function of bias level ($\lambda = 278$ nm). Dotted lines in (b) show power law $L \propto I^P$, where $P = 1$ and $P = 2$.*

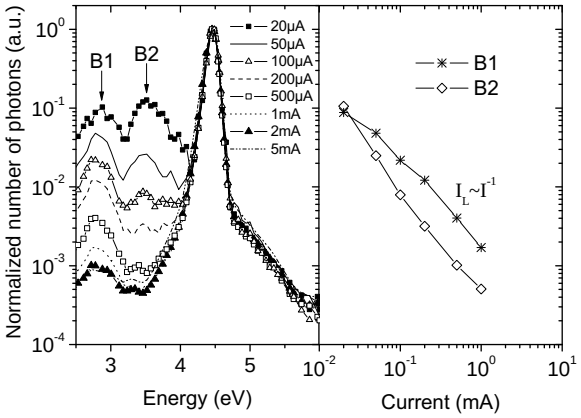


*Figure 6.5: On the left, the EL spectra measured at low current densities and normalized to UV peak. On the right, the normalized intensity of B1 and B2 bands ($\lambda = 278$ nm).*

current has been reported. As can be noticed, the intensity of the UV emission has a quadratic dependence on injected current ($L_{UV} \propto I^2$), while the deep-level band B varies linearly with current ($L_B \propto I$). On the basis of previous works [75], this fact indicates that trap-related recombination is relevant with respect to band-to-band recombination, affecting significantly the intensity-current relation. Even if the performance of the analyzed is competitive for commercial application, this results indicates that there is still room for improvement of the optical characteristics of the devices, by reducing the contribution of trap-related recombination with respect to NBE emission, until reaching linear dependence of the UV intensity on applied current.

A more detailed investigation of low-energy emission bands has been carried out over a wide current range (from 20 μA to 5 mA): the results are shown inFig. 6.5, that reports the EL spectra measured on L278 at different current levels, normalized to the maximum of the UV emission. No blue-shift of the main emission peak with increasing currents has been detected on the analyzed samples: this suggests that localization effects in the AlGaN layers are negligible [78]. Two wide emission bands (B1 centered at about 2.78 eV and B2 at 3.4 eV) are well resolved at currents below 200 μA: the presence of these bands can be ascribed to the presence of two deep-level radiative recombination mechanisms within the active region. The validation of this hypothesis is given by considering that relative intensity of these bands increases on decreasing current. In fact, at high injection current levels, these parasitic radiative paths saturate, and their contribution to the overall emission becomes negligible with respect to the main UV peak. As a consequence, the normalized intensities of B1 and B2 (shown in Fig. 6.5) decrease on increasing current following an almost inverse proportionality, suggesting a saturation of the related centers at high carrier densities.

## 6.4 Effects of ageing

For each emitting wavelength, one or two LEDs have been selected for submitted to lifetime testing. Since these structures are still unstable, no accelerated conditions have been chosen and the nominal current of $20\ \mathrm{mA}$ at RT ($10\ \mathrm{mA}$ for L247) have been selected for stress, corresponding to a current density of $16.3\ \mathrm{A/cm^2}$. At several steps a complete electrical (I-V, C-V) and optical (EL, L-I) characterization has been performed on each sample.

Since the number of samples available for analysis was limited, the results won't be statistically relevant as the reliability analysis is based on large set of samples. However the work aimed at finding main the main degradation process affecting the stability of novel technology devices: a complete reliability testing can be performed once the infant mortality is overcome.

### 6.4.1 Optical properties

Stress induced the decrease of the Optical Power of the devices in the whole investigated current range. The kinetic of the OP decay can be understood from the diagram in Fig. 6.6(b), showing the OP degradation measured at $10\ \mathrm{mA}$ during stress time. The OP decrease took place mostly during the initial 200 hours of treatment, while the behavior of the devices was found to be quite stable in the remaining stress time. In order to evaluate the entity of the optical power decay at the different measuring current levels, in Fig. 6.6(a) the L-I curves measured before and during stress and normalized to the values obtained on the untreated sample have been reported. OP decay was found to be more prominent at low measuring current levels: for a measuring current of $1\ \mathrm{mA}$, OP loss was around 60%, while on the other hand, at $20\ \mathrm{mA}$ we detected only a 30% OP decrease. This fact suggests that OP decrease is related to the generation of non-radiative centers, that reduce the internal quantum efficiency of the devices [28, 46]. At high current levels, these centers are saturated by the high flux of injected carriers, and therefore optical power loss is limited.

The degradation of spectral profiles during stress is reported in Fig. 6.7. No significant variation of the spectral shape has been detected as a consequence of ageing: this fact indicates that the decrease of the main UV peak is not related to the generation/increase of alternative radiative recombination paths, and strengthens the hypothesis that OP loss is due to the increase of the non-radiative recombination rate. Furthermore, the OP decrease during stress did not show a square-root time-dependent kinetic, making the hypothesis of Al diffusion not valid [76].

The stress has been performed on each sample emitting at different wavelengths. All samples exhibited a lumen decay during first hours of stress. The Fig. 6.8 show the OP decay for all samples submitted to stress. An important results from the comparative analysis is the wavelength-dependent degradation rate detected. As can be noticed, the degradation is prominent for those devices that emit at lower wavelength. This result can be clearly identified in Fig. 6.9, where the percentage of OP loss at 1000 hours have been reported.

Since the growth process and the structure of the devices is always the same, the different behaviour in terms of reliability can be ascribed to different molar fraction of Al in AlGaN QW. The fact that the OP decay increase with higher Al concentration can be related to defectivity

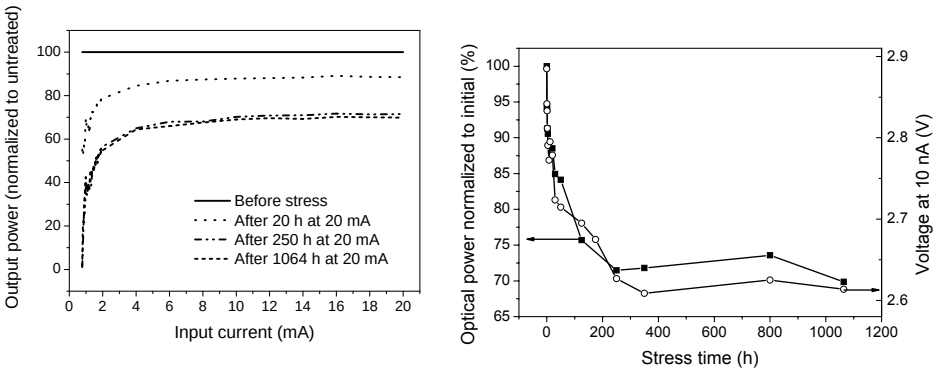


*(a)* *(b)*

*Figure 6.6: Optical power decay: (a) normalized L-I curves measured before and after stress, and (b) comparison with low forward voltage measured at* $10\ \mathrm{nA}$ *(*$\lambda = 295\ \mathrm{nm}$*).*

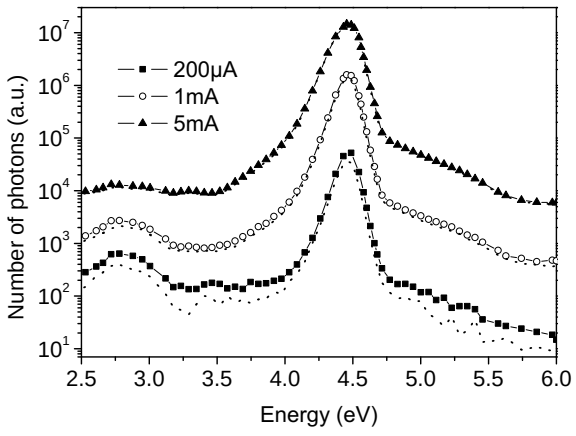


*Figure 6.7: EL spectra(symbols) before and after (dotted lines) 200h of ageing at different current levels(*$\lambda = 278\ \mathrm{nm}$*)*

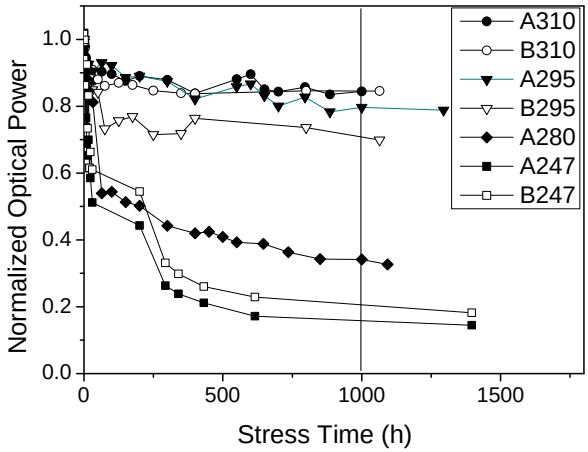


*Figure 6.8: Comparison between luminous decay of all the samples submitted to electrical ageing.*

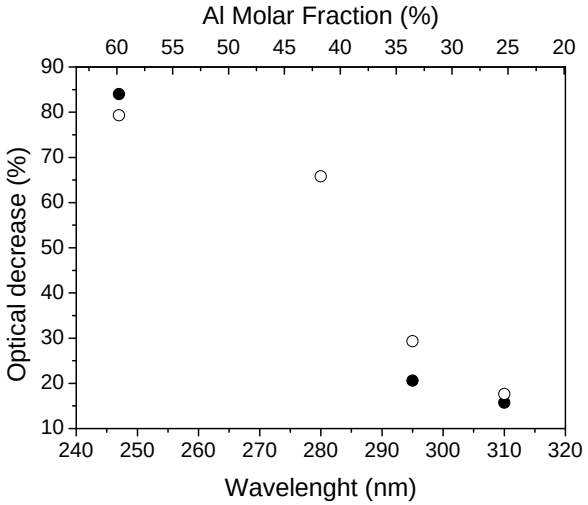


*Figure 6.9: Percentage of luminous decrease at 1000h of ageing for LEDs emitting at different DUV wavelengths.*

originated by Al inclusion in QW. A high concentration of Al can be responsible of high dislocations density in the lattice structure, leading to a increase in non-radiative recombination centers. This hypothesis is in agreement with optical and spectral results reported before.

### 6.4.2 Electrical properties

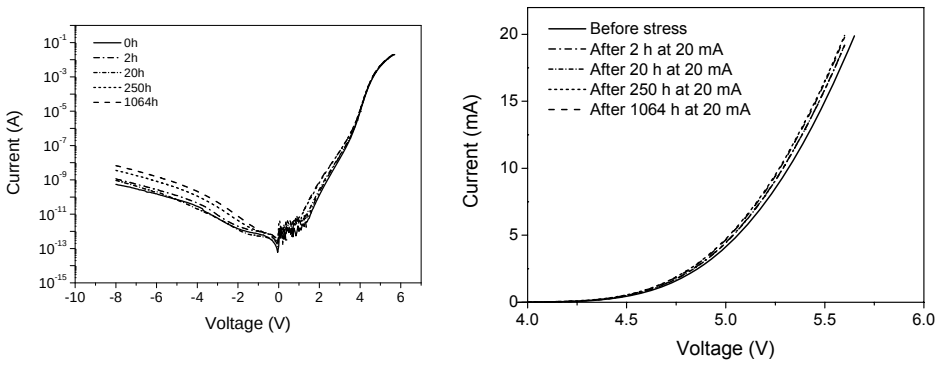


*(a)* *(b)*

*Figure 6.10: I-V characteristics measured before and after stress in (a) log-scale and (b) linear scale ($\lambda = 295$ nm).*

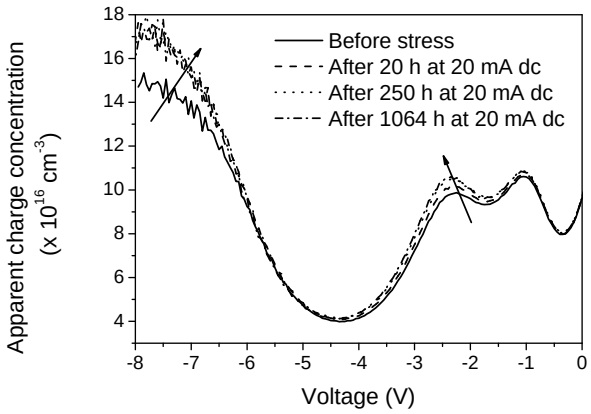


*Figure 6.11: Apparent Charge Concentration vs. reverse voltage measured after and before ageing($\lambda = 295$ nm)*

In order to better characterize the degradation process, we have carried out an extensive electrical characterization of the samples submitted to stress. DC ageing did not induce significant modifications of the forward I-V curves of the devices, i.e. no significant increase or monotonic kinetic of operating voltage has been detected after stress (see the semi-logarithmic I-V curves in Fig. 6.10). On the other hand, the devices current increased (x 10) both in the reverse and low positive bias region, suggesting that stress induces the increase of the generation/recombination or tunneling components. To prove this hypothesis, in Fig. 6.6(b) the OP decay of L295 has been compared to low forward voltage measured at 10 nA during stress. As

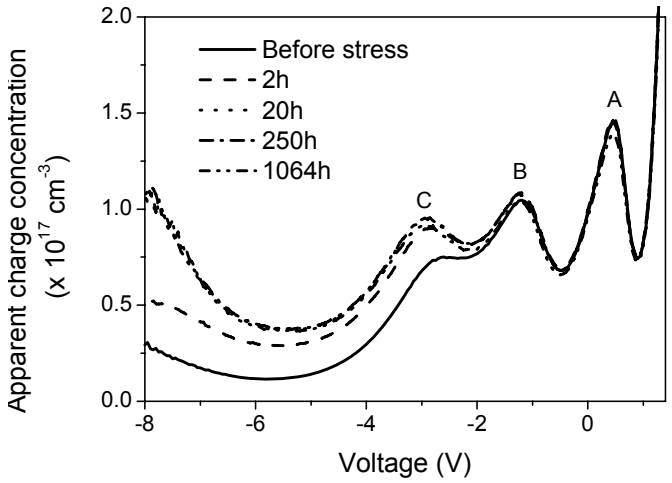


*Figure 6.12: Apparent Charge Concentration vs. reverse voltage measured after and before ageing($\lambda = 310$ nm)*

the figure shows, the two kinetics are correlated, indicating that the hypothesis of generation of defects: these may induce both an increase in generation/recombination and/or tunneling components of the I-V curves and the generation of non-radiative path close to the active region.

From the optical characterization of devices degradation, we have obtained evidences that OP decrease can be due to an increase of the non-radiative components in the active region. This process can be related to the propagation of defects towards the active region of the devices, taking place as a consequence of carrier flow. In order to find a correlation between degradation process and modifications of the properties of the active region, we have carried out capacitance-voltage characterization of the devices at each step of the ageing tests. By C-V characterization it is possible to extrapolate information on the Apparent Charge Distribution (ACD) within the space charge region [79, 80, 81, 23], under the $n + /p$ asymmetric junction approximation. Fig. 6.11 and 6.12 show the variation of the ACD profile induced by stress at $20$ mA on samples L295 and L310 respectively.

DC bias ageing induced the increase of the charge concentration: especially close to the heterointerface before the bulk side and close to the bulk side itself. These changes take place mostly during the initial 250 h of treatment, just like the optical power decrease. This fact suggests that the optical power decrease and the modifications of the charge profile are correlated, and is consistent with previous literature work on InGaN-based blue LEDs [8]. Degradation can be attributed to the increase of the non-radiative recombination rate, related to the worsening of the properties of the active layer of the devices. The ACD profiles measured during stress indicate that stress induces localized modifications of the charge distribution, that can be related to the generation of defective states. Therefore, while optical measurements indicate that stress is related to the increase of the non-radiative recombination components, capacitive analysis gives further insight in this degradation process, supporting the hypothesis that stress induces modification in the charge distribution in the active layer due to defects modifications. As a result, we have found that OP degradation is correlated to the modification of the properties of the active layer of the LEDs, especially in the last charge accumulation point before the bulk and close to the bulk.

### 6.4.3 Catastrophic failures

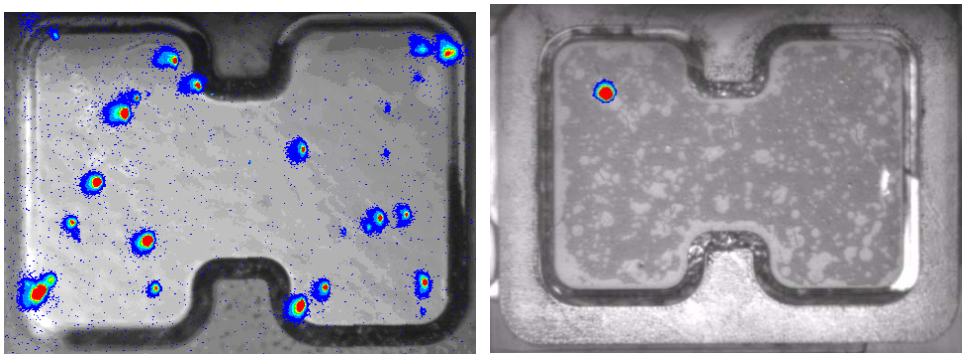

(a) (b)

*Figure 6.13: EMMI image of two LEDs failed after ageing and showing short-current behaviour. The spots permit to localize the short position ($\lambda = 265$ nm).*

Finally, a small number of devices operating at short wavelengths (L265) showed catastrophic failures during stress, with a sudden decrease of their output power. After catastrophic failure, devices behave like short circuits. Emission microscopy carried out after stress allowed us to identify the position of the short (Fig. 6.13(a)-(b)). This kind of degradation process has been previously attributed to poor morphology of LEDs structure [78], related to the presence of defects in the AlGaN layers.

## 6.5 Conclusions

A study on DUV LEDs performance and reliability has been reported. The relation between the different radiative emission processes, by evaluating the relative electroluminescence intensity of the three main emission bands of the LEDs has been analyzed in detail. It was also presented an analysis of the mechanisms that limit the reliability of these devices during dc stress: it has been shown that (i) OP degradation can be ascribed to the increase of the non-radiative recombination rate, and (ii) the degradation rate is related to the molar fraction of Al inside the QWs. C-V analysis provided further information on the degradation process, indicating that as a consequence of stress, the charge distribution in the active layer is modified, possibly due to the generation of defective states. Toghether with reported degradation mechanisms, a failure mode responsible for sudden death of device was found and it has been ascribed to a poor morphology of the LED structure.

# Chapter 7

# Conclusions

The Ph.D. project described in this thesis was focused on the reliability aspects of Gallium Nitride based LEDs, related to the thermal properties. The work aimed at:

i giving an updated overview of the LED technology and performances and the related issues;

ii offering an in-depth analysis of thermal properties in LED, with the punctual explanation of the experimental implementation of the measurement setup;

iii designing, implementing and analyzing results of accelerated lifetime testing on different LED families;

iv identifying the degradation mechanisms that limit the lifetime of analyzed devices;

v providing the degradation models for LEDs lifetime estimation.

The thesis provided a dissertation on the state of the art of LED technology, giving a brief example of the performances of such devices. By giving some examples of reliability works taken from the literature, it was possible to draw the issues that currently affect the performances and lifetime of LEDs. The description of LED properties was included in the introduction, in addition to the explanation of the data collected by device measurement. In particular, an in-depth description of thermal properties of LEDs was provided, in order to explain the problematics related to thermal management. The experimental and simulation results have been reported as well, underlying the difficulties of obtaining a good setup for temperature measurements in microelectronic devices.

Afterwards, the core of the work has been presented. The description of reliability analysis on three different LED families has been provided: (i) low flux white LEDs (chapter 4), (ii) high power white LEDs with Chip On Board technology (chapter 5), and (iii) Deep UV emitting AlGaN based LEDs (chapter 6). Details on experimental setup, ageing design, and results analysis have been reported. In particular, a degradation model has been extrapolated for several devices, able to provide lifetime previsions under operating conditions. Furthermore, several degradation mechanisms have been detected, thanks to the cross correlation of results from different measurements (electrical, optical, thermal). The more interesting failure modes

detected are: (i) the modification of the optical properties of the encapsulation, due to the high temperatures involved, (ii) the detachment of the encapsulation layer in low flux white LEDs, that induced a thermal resistance increase and the total failure of the device, (iii) the generation of non-radiative recombination centers in UV LEDs, (iv) the generation of parasitic path that short the junction.

The original results of the accelerated stress testing can be useful for the scientific community and for the lighting engineering, since the degradation of studied LEDs is strongly related to the ambient conditions and to the interface between the device and the ambient. The results provided by the work have been published in more than 20 publications in international journals and conferences.

# Appendix A

# Statistical Distributions and Models for Reliability

The study of the impact of the stress applied on the device reliability can be performed in accelerated stress conditions. This principle is based on the assumption that the failure times are linearly related to the stress conditions. The failure time distribution at stress level $s_1$ is expected to be the same at the other stress levels $s_2, s_3, ...$ as well as under nominal conditions. There are different relationships between accelerated conditions and nominal conditions:

- failure time
  $t_0 = A_F t_s$
  where $t_0$ ($t_s$) is the failure time under nominal (accelerated) conditions, and $A_F$ the acceleration factor;

- cumulative distribution functions (CDFs)
  $F_0(t) = F_S\left(\frac{t}{A_F}\right)$

- probability density functions
  $f_0(t) = \left(\frac{1}{A_F}\right) f_S\left(\frac{t}{A_F}\right)$

- failure rates
  $h_0(t) = \left(\frac{1}{A_F}\right) h_S\left(\frac{t}{A_F}\right)$

The most common distributions are the exponential and the Weibull, that will be described in the following lines. In addition, a description of the Arrhenius model will be provided, since is widely applied in lifetime analysis of LEDs.

## A.1 The Exponential Distribution

When the Time To Failure is exponentially distributed with a constant failure rate $\lambda_S$, we are facing an exponential distribution. The CDF of the exponential distribution is:

$$F_S(t) = 1 - e^{-\lambda_S t}$$

with the CFD at nominal condition expressed as:

$$F_0(t) = F_S\left(\frac{t}{A_F}\right) = 1 - e^{-\lambda_S t/A_F}.$$

The failure rates are related as

$$\lambda_0 = \frac{\lambda_S}{A_F}.$$

For examples on exponential distribution application, see [82].

## A.2 The Weibull Distribution

The Weibull distribution is an exponential distribution with an further parameter. The Weibull CDF can be expressed as:

$$F_S(t) = 1 - e^{-(t/\theta_S)^{\gamma_S}} \qquad t \geq 0, \gamma_S \geq 0, \theta_S \geq 0$$

where $\gamma_S$ is the shape parameter of the Weibull distribution, and $\theta_S$ the scale parameter (or characteristic life) under stress conditions. The CDF under nominal conditions is:

$$F_0(t) = F_S\left(\frac{t}{A_F}\right) = 1 - e^{-(t/\theta_S A_F)^{\gamma_S}} = 1 - e^{-(t/\theta_0)^{\gamma_0}}.$$

The failure times distributions under accelerated and nominal conditions have the same shape parameter $\gamma_0 = \gamma_S$ and $\theta_0 = \theta_S A_F$. If the shape parameter is different for different stress conditions, then the failure rate cannot be shaped by the Weibull distribution. We can also define the MTTF at nominal conditions:

$$MTTF_0 = {\theta_0}^{1/\gamma}\Gamma\left(1 + \frac{1}{\gamma}\right).$$

In order to visually identify a Weibull distribution, one can apply some transformation to the CDF:

$$\begin{aligned} F_0(t) &= 1 - e^{-(t/\theta_0)^{\gamma_0}} \\ \ln\left(\frac{1}{1 - F_0(t)}\right) &= \left(\frac{t}{\theta_0}\right)^{\gamma_0} \\ \ln\left[\ln\left(\frac{1}{1 - F_0(t)}\right)\right] &= \gamma_0 \ln t - \gamma_0 \ln \theta_0 \end{aligned}$$

Thus, with a proper transformation of CDF and plotting modified data vs. $\ln t$ one can extrapolate the shape and the scale parameter performing a linear fitting.

## A.3 The Arrhenius Model

In microelectronic devices, it's common to find that the degradation is induced by the temperature stress. The thermally activated degradation process can be represented by the Arrhenius model, that uses the Arrhenius reaction rate equation:

$$r = Ae^{-(E_a/kT)}$$

where $A$ is a thermally independent constant, $E_a(\mathrm{eV})$ the activation energy of the process, $k$ the Boltzmann constant, and $T(\mathrm{K})$ the temperature. The activation energy $E_a$ is the factor that determines the slope of the reaction rate curve with temperature. In general, $E_a$ is treated as a slope of a curve rather than a specific energy level. A low $E_a$ value indicates a low thermal activation of the process; on the other hand, a high activation energy indicates a high degree of temperature dependence.

The activation energy is usually calculated by linear fitting of the plot $\ln TTF$ vs. $\frac{1}{kT}$. Once one knows the activation energy of a process, can calculate the acceleration factor for a given stress temperature:

$$A_F = \exp \frac{E_a}{k} \left( \frac{1}{T_0} - \frac{1}{T_S} \right).$$

# Bibliography


[1] U. Zehnder, B. Hahn, J. Baur, M. Peter, S. Bader, H. J. Lugauer, and A. Weimar, "GaInN LEDs: straight way for solid state lighting," in *Society of Photo-Optical Instrumentation Engineers (SPIE) Conference Series*, ser. Society of Photo-Optical Instrumentation Engineers (SPIE) Conference Series, vol. 6797, Sep. 2007.

[2] C. H. Seager, S. M. Myers, A. F. Wright, D. D. Koleske, and A. A. Allerman, "Drift, diffusion, and trapping of hydrogen in p type GaN," *J. Appl. Phys.*, vol. 92, no. 12, pp. 7246–7252, 2002.

[3] M. Meneghini, L. Trevisanello, G. Meneghesso, E. Zanoni, F. Rossi, M. Pavesi, U. Zehnder, and U. Strauss, "High-temperature failure of GaN LEDs related with passivation," *Superlattices and Microstructures*, vol. 40, pp. 405–411, Oct. 2006.

[4] H. A. et al., "Growth of thick InGaN with the aim of realizing bright green LED and LD," in *Proc. of Display & solid state lighting Conference, Seoul, Korea*, 2008, pp. 126–129.

[5] M. Osinski, J. Zeller, P.-C. Chiu, B. S. Phillips, and D. B. Barton, "AlGaN/InGaN/GaN blue light emitting diode degradation under pulsed current stress," *Appl. Phys. Lett.*, vol. 69, no. 7, pp. 898–900, 1996.

[6] M. Meneghini, L.-R. Trevisanello, R. Penzo, M. Benedetti, U. Zehnder, U. Strauss, G. Meneghesso, and E. Zanoni, "Reversible degradation of gan leds related to passivation," *Reliability physics symposium, 2007. proceedings. 45th annual. ieee international*, pp. 457–461, April 2007.

[7] L. Stafford, L. F. Voss, S. J. Pearton, H. T. Wang, and F. Ren, "Improved long-term thermal stability of InGaN/GaN multiple quantum well light-emitting diodes using TiB- and Ir-based p-ohmic contacts," *Applied Physics Letters*, vol. 90, no. 24, p. 242103, 2007.

[8] F. Rossi, M. Pavesi, M. Meneghini, G. Salviati, M. Manfredi, G. Meneghesso, A. Castaldini, A. Cavallini, L. R. U. Strauss, U. Zehnder, and E. Zanoni, "Influence of shortterm lowcurrent dcaging on the electrical and optical properties of AlGaN blue Light-Emitting Diodes," *J. Appl. Phys.*, vol. 99, pp. 053 104–1–053 104–7, 2006.

[9] Z. Gong, M. Gaevski, V. Adivarahan, W. Sun, M. Shatalov, and M. A. Khan, "Optical power degradation mechanisms in AlGaN-based 280 nm deep ultraviolet light-emitting diodes on sapphire," *Appl. Phys. Lett.*, vol. 88, pp. 121 106–1–3, 2006.

[10] T. Yu, S. Shang, Z. Chen, Z. Qin, L. Lin, Z. Yang, and G. Zhang, "Luminescence degradation of InGaN/GaN violet leds," *J. of Lumin.*, vol. 122, pp. 696–699, 2007.

[11] S. Tomiya, T. Hino, S. Goto, M. Takeya, and M. Ikeda, "Dislocation related issues in the degradation of GaN-based laser diodes," *IEEE Journal of Selected Topics in Quantum Electronics*, vol. 10, no. 6, pp. 1277–1286, 2004.

[12] A. Chitnis, J. Sun, V. Mandavilli, R. Pachipulusu, S. Wu, M. Gaevski, V. Adivarahan, J. P. Zhang, M. A. Khan, A. Sarua, and M. Kuball, "Self-heating effects at high pump currents in deep ultraviolet light-emitting diodes at 324 nm," *Applied Physics Letters*, vol. 81, no. 18, pp. 3491–3493, 2002.

[13] A. A. Allerman, M. H.Crawford, A. J. Fisher, K. H. A. Bogart, S. R. Lee, D. M. Follstaedt, P. P. Provencio, and D. D. Koleste, "Growth and design of deep-UV (240-290 nm) light emitting diodes using AlGaN alloys," *J. of Crys. Growth*, vol. 272, pp. 227–241, 2004.

[14] Y. Gu, N. Narendran, T. Dong, and H. Wu, "Spectral and luminous efficacy change of high power LEDs under different dimming methods," in *Proceedings of SPIE 6337, 6337J*, 2006.

[15] L. Trevisanello, M. Meneghini, G. Mura, M. Vanzi, M. Pavesi, G. Meneghesso, and E. Zanoni, "Accelerated life test of high brightness light emitting diodes," *Device and Materials Reliability, IEEE Transactions on*, vol. 8, no. 2, pp. 304–311, June 2008.

[16] L.-R. Trevisanello, M. Meneghini, G. Mura, C. Sanna, S. Buso, G. Spiazzi, M. Vanzi, G. Meneghesso, and E. Zanoni, "Thermal stability analysis of high brightness LED during high temperature and electrical aging," in *Society of Photo-Optical Instrumentation Engineers (SPIE) Conference Series*, ser. Society of Photo-Optical Instrumentation Engineers (SPIE) Conference Series, vol. 6669, Sep. 2007.

[17] D. L. Barton, M. Osinski, P. Perlin, C. J. Helms, and N. H. Berg, "Life tests and failure mechanisms of GaN-AlGaN-InGaN light emitting diodes," in *Proc. IEEE-IRPS*, 1997.

[18] M. Burmen, F. Pernus, and B. Likar, "Accelerated estimation of spectral degradation of white gan-based leds," *Meas. Sc. and Tech.*, vol. 18, no. 1, pp. 230–238, 2007.

[19] J. Hu, L. Yang, and M. W. Shin, "Mechanism and thermal effect of delamination in light-emitting diode packages," *Microelectron. J.*, vol. 38, no. 2, pp. 157–163, 2007.

[20] M. Meneghini, L. Trevisanello, S. Podda, S. Buso, G. Spiazzi, G. Meneghesso, and E. Zanoni, "Stability and performance evaluation of high-brightness light-emitting diodes under DC and pulsed bias conditions," in *Society of Photo-Optical Instrumentation Engineers (SPIE) Conference Series*, ser. Society of Photo-Optical Instrumentation Engineers (SPIE) Conference Series, vol. 6337, Sep. 2006.

[21] J. Hu, L. Yang, and M. W. Shin, "Electrical, optical and thermal degradation of high power gan/ingan light-emitting diodes," *J. of Phys. D: Appl. Phys.*, vol. 41, no. 3, p. 035107, 2008.

[22] M. R. Krames, O. B. Shchekin, R. Mueller-Mach, G. Mueller, L. Zhou, G. Harbers, and M. G. Craford, "Status and future of high-power light-emitting diodes for solid-state lighting," *J. Display Technol.*, vol. 3, no. 2, pp. 160–175, 2007.

[23] M. Meneghini, "Analysis of the physical processes that limit the reliability of gan-based optoelectronic devices," Ph.D. dissertation, University of Padova, 2008.

[24] M. Fukuda, *"Optical Semiconductor Devices"*. New York: Wiley-Interscience, 1999.

[25] E. F. Schubert, *Light Emitting Diodes*. Cambridge University Press, 2003.

[26] S. Nakamura, S. Pearton, and G. Fasol, *The blue laser diode: the complete history*, 2nd ed. Springer, 1997.

[27] M. G. Craford, "High power LEDs for solid state lighting: Status, trends, and challenges," *J. of Light and Vis. Env.*, vol. 32, no. 2, pp. 58–62, 2008.

[28] O. Pursiainen, N. Linder, A. Jeager, and R. Oberschmid, "Identification of aging mechanism in the optical and electrical characteristics of light-emitting diodes," *Appl. Phys. Lett.*, vol. 79, no. 18, pp. 2895–2897, 2001.

[29] B. Hahn, "Recent advances in GaInN LEDs," in *Proceedings of 31st WOCSDICE, Venice, Italy*, 2007.

[30] V. Haerle, B. Hahn, S. Kaiser, A. Weimar, S. Bader, F. Eberhard, A. Plössl, and D. Eisert, "High brightness LEDs for general lighting applications using the new ThinGaN-Technology," *Phys. Stat. Sol. (a)*, vol. 201, no. 12, pp. 2736–2739, 2004.

[31] R. Mueller-Mach and G. O. Mueller, "White-light-emitting diodes for illumination," in *Society of Photo-Optical Instrumentation Engineers (SPIE) Conference Series*, ser. Society of Photo-Optical Instrumentation Engineers (SPIE) Conference Series, H. W. Yao, I. T. Ferguson, and E. F. Schubert, Eds., vol. 3938, Apr. 2000, pp. 30–41.

[32] R. Mueller-Mach, G. O. Mueller, M. R. Krames, and T. Trottier, "High-Power Phosphor-Converted Light-Emitting Diodes Based on III-Nitrides," *IEEE Journal on Selected Topics in Quantum Electronics*, vol. 8, no. 2, pp. 339–345, 2002.

[33] D. A. Steigerwald, J. C. Bhat, D. Collins, R. M. Fletcher, M. O. Holcomb, M. J. Ludowise, P. S. Martin, and S. L. Rudaz, "Illumination with solid state lighting technology," *IEEE J. on Sel. Top. in Quantum Electr.*, vol. 8, no. 2, pp. 310–320, 2002.

[34] D. S. C. P. T. Program, "Round 1 of product testing," U.S. Dept. of Energy, Tech. Rep., 2007.

[35] M. R. Krames, J. Bhat, D. Collins, N. F. Gardner, W. Go, C. H. Lowery, M. Ludowise, P. S. Martin, G. Mueller, R. Mueller-Mach, S. Rudaz, D. A. Steigerwald, S. A. Stockman, and J. J. Wierer, "High-power iii-nitride emitters for solid-state lighting," *Phys. Stat. Sol. (a)*, vol. 192, no. 2, pp. 237–245, 2002.

[36] S. Muthu, F. Schuurmans, and M. Pashley, "Red, green, and blue leds for white light illumination," *Selected Topics in Quantum Electronics, IEEE Journal of*, vol. 8, no. 2, pp. 333–338, Mar/Apr 2002.

[37] J. K. Park, M. A. Lim, C. H. Kim, H. D. Park, J. T. Park, and S. Y. Choi, "White light-emitting diodes of gan-based sr[sub 2]sio[sub 4]:eu and the luminescent properties," *Applied Physics Letters*, vol. 82, no. 5, pp. 683–685, 2003.

[38] J. K. Park, C. H. Kim, S. H. Park, H. D. Park, and S. Y. Choi, "Application of strontium silicate yellow phosphor for white light-emitting diodes," *Applied Physics Letters*, vol. 84, no. 10, pp. 1647–1649, 2004.

[39] J. S. Kim, P. E. Jeon, J. C. Choi, H. L. Park, S. I. Mho, and G. C. Kim, "Warm-white-light emitting diode utilizing a single-phase full-color ba[sub 3]mgsi[sub 2]o[sub 8]:eu[sup 2+], mn[sup 2+] phosphor," *Applied Physics Letters*, vol. 84, no. 15, pp. 2931–2933, 2004.

[40] R. J. Xie and N. Hirosaki, "Design, synthesis and luminescence of silicon-based nitride phosphors for white LEDs," in *Proc. of Display & solid state lighting Conference, Seoul, Korea*, 2008, pp. 182–183.

[41] C.-F. Huang, C.-F. Lu, T.-Y. Tang, J.-J. Huang, and C. C. Yang, "Phosphor-free white-light light-emitting diode of weakly carrier-density-dependent spectrum with prestrained growth of ingan/gan quantum wells," *Applied Physics Letters*, vol. 90, no. 15, p. 151122, 2007.

[42] I.-K. Park, J.-Y. Kim, M.-K. Kwon, C.-Y. Cho, J.-H. Lim, and S.-J. Park, "Phosphor-free white light-emitting diode with laterally distributed multiple quantum wells," *Applied Physics Letters*, vol. 92, no. 9, p. 091110, 2008.

[43] N. Narendran, Y. Gu, J. P. Freyssinier, H. Yu, and L. Deng, "Solid-state lighting: failure analysis of white LEDs," *J. of Crys. Growth*, vol. 268, pp. 449–456, 2004.

[44] S. Ishizaki, H. Kimura, and M. Sugimoto, "Lifetime estimation of high power LEDs," *J. Light & Vis. Env.*, vol. 31, no. 1, pp. 11–18, 2007.

[45] T. Yanagisawa, "Estimation of the degradation of InGaN/AlGaN blue light-emitting diodes," *Microel. Reliab.*, vol. 37, no. 8, pp. 1239–1241, 1997.

[46] P. N. Grillot, M. R. Krames, H. Zhao, and S. H. Teoh, "Sixty Thousand Hour Light Output Reliability of AlGaInP Light Emitting Diodes," *IEEE Transactions on Devices and Materials Reliability*, vol. 6, no. 4, pp. 564–574, 2006.

[47] G. Farkas, Q. Vader, A. Poppe, and G. Bognar, "Thermal investigation of high power optical devices by transient testing," *Components and Packaging Technologies, IEEE Transactions on*, vol. 28, no. 1, pp. 45–50, March 2005.

[48] P. Bagnoli, C. Casarosa, E. Dallago, and M. Nardoni, "Thermal resistance analysis by induced transient (trait) method for power electronic devices thermal characterization." *Power Electronics, IEEE Transactions on*, vol. 13, no. 6, pp. 1220–1228, Nov 1998.

[49] S. V., "Fine structure of heat flow path in semiconductor devices: A measurement and identification method," *Solid State Electronics*, vol. 31, pp. 1363–1368, Sep. 1988.

[50] ——, "A new evaluation method of thermal transient measurement results," *Microel. J.*, vol. 28, no. 3, pp. 277–292, March 1997.

[51] D. Blackburn, "Temperature measurements of semiconductor devices - a review," *Semiconductor Thermal Measurement and Management Symposium, 2004. Twentieth Annual IEEE*, pp. 70–80, Mar 2004.

[52] Y. Xi, J.-Q. Xi, T. Gessmann, J. M. Shah, J. K. Kim, E. F. Schubert, A. J. Fischer, M. H. Crawford, K. H. A. Bogart, and A. A. Allerman, "Junction and carrier temperature measurements in deep ultraviolet light emitting diodes using three different methods," *Appl. Phys. Lett.*, vol. 86, pp. 031 907–1–031 907–3, 2005.

[53] Y. Xi and E. F. Schubert, "Junction temperature measurement in GaN ultraviolet light emitting diodes using diode forward voltage method," *Appl. Phys. Lett.*, vol. 86, no. 12, pp. 2163–2165, 2004.

[54] Y. Gu and N. Narendran, "A non-contact method for determining junction temperature of phosphor-converted white LEDs," in *Proceedings of SPIE 5187*, 2004, pp. 107–114.

[55] L. Jayasinghe, Y. Gu, and N. Narendran, "Characterization of thermal resistance coefficient of high-power LEDs," in *Society of Photo-Optical Instrumentation Engineers (SPIE) Conference Series*, ser. Society of Photo-Optical Instrumentation Engineers (SPIE) Conference Series, vol. 6337, Sep. 2006.

[56] X. A. Cao, S. F. LeBoeuf, and T. E. Stecher, "Temperature-dependent electroluminescence of AlGaN-based UV LEDs," *IEEE Electron Device Letters*, vol. 27, no. 5, pp. 329–331, 2005.

[57] P. Vitta, P. Pobedinskas, and A. Zukauskas, "Phosphor thermometry in white light-emitting diodes," *Photonics Technology Letters, IEEE*, vol. 19, no. 6, pp. 399–401, March15, 2007.

[58] L. Yang, J. Hu, L. Kim, and M. W. Shin, "Variation of thermal resistance with input power in LEDs," *Physica Status Solidi C Current Topics*, vol. 3, pp. 2187–2190, Jun. 2006.

[59] L. Jayasinghe, T. Dong, and N. Narendran, "Is the thermal resistance coefficient of high-power LEDs constant?" in *Society of Photo-Optical Instrumentation Engineers (SPIE) Conference Series*, ser. Society of Photo-Optical Instrumentation Engineers (SPIE) Conference Series, vol. 6669, Sep. 2007.

[60] L. Kirkup, W. Kalceff, and G. McCredie, "System for measuring the junction temperature of a light emitting diode immersed in liquid nitrogen," *Review of Scientific Instruments*, vol. 77, no. 4, p. 046107, 2006.

[61] B. Fan, H. Wu, Y. Zhao, Y. Xian, B. Zhang, and G. Wang, "Thermal study of high-power nitride-based flip-chip light-emitting diodes," *Electron Devices, IEEE Transactions on*, vol. 55, no. 12, pp. 3375–3382, Dec. 2008.

[62] J. Piprek, *Semiconductor optoelectronic devices: introduction to physics and simulation*. Academic press, 2003.

[63] J. Bielecki, A. Jwania, F. El Khatib, and T. Poorman, "Thermal considerations for led components in an automotive lamp," *Semiconductor Thermal Measurement and Management Symposium, 2007. SEMI-THERM 2007. Twenty Third Annual IEEE*, pp. 37–43, March 2007.

[64] C.-C. Kao, H.-C. Kuo, H.-W. Huang, J.-T. Chu, Y.-C. Peng, Y.-L. Hsieh, C. Y. Luo, S.-C. Wang, C.-C. Yu, and C.-F. Lin, "Light-output enhancement in a nitride-based light-emitting diode with 22° undercut sidewalls," *IEEE Phot. Thecn. Lett.*, vol. 17, no. 1, pp. 19–21, 2005.

[65] A. Ameraseker and C. Duvvury, *ESD in Silicon Integrated Circuits*. Wiley InterScience, 2002, pp. 17–67.

[66] Lumileds, "Luxeon reliability," Philips Lumileds, Tech. Rep. RD25, 2006. [Online]. Available: http://www.lumileds.com/pdfs/RD25.pdf

[67] S. Levada, M. Meneghini, G. Meneghesso, and E. Zanoni, "Analysis of DC current accelerated life tests of GaN LEDs using a weibull-based statistical model," *Device and Materials Reliability, IEEE Transactions on*, vol. 5, no. 4, pp. 688–693, Dec. 2005.

[68] M. Meneghini, L. Trevisanello, U. Zehnder, T. Zahner, U. Strauss, G. Meneghesso, and E. Zanoni, "High-temperature degradation of GaN LEDs related to passivation," *IEEE Transactions on Electron Devices*, vol. 53, no. 12, pp. 2981–2987, 2006.

[69] M. Meneghini, L.-R. Trevisanello, G. Meneghesso, and E. Zanoni, "A review on the reliability of GaN-based LEDs," *Device and Materials Reliability, IEEE Transactions on*, vol. 8, no. 2, pp. 323–331, June 2008.

[70] A. Dehmel, J. Schulz-Harder, A. Roth, and I. Baumeister, "Direct copper bonded ceramic substrates for use with power leds," *Electronic Packaging Technology, 2007. ICEPT 2007. 8th International Conference on*, pp. 1–6, Aug. 2007.

[71] Z.-Q. Fang, D. C. Reynolds, and L. D. C, "Changes in electrical characteristics associated with degradation on InGaN blue light emitting diodes," *J. of Elect. Mat.*, pp. 448–451, 2000.

[72] X. A. Cao, P. M. Sandvik, S. F. LeBoeuf, and S. D. Arthur, "Defect generation in InGaN/GaN light-emitting diodes under forward and reverse electrical stresses," *Microel. Reliab.*, vol. 43, pp. 1987–1991, 2003.

[73] Y. Bilenko, A. Lunev, X. Hu, J. Deng, T. M. Katona, J. Zhang, R. Gaska, M. S. Shur, W. Sun, V. Adivarahan, M. Shatalov, and A.Khan, "10 milliwatt pulse operation of 265 nm AlGaN Light Emitting Diodes," *Jpn. J. Appl. Phys.*, vol. 44, no. 2, p. L98, 2005.

[74] J. Zhang, Y. Bilenko, X. Hu, A. Lunev, A. Sattu, J. Deng, M. Shatalov, W. Sun, J. Yang, and R. Gaska, "AlGaN Based Deep UV LEDs with emission at 230-270 nm," in *ICNS-2007, Las Vegas NV*, 2007.

[75] K. X. Chen, Y. A. Xi, F. W. Mont, J. K. Kim, E. F. Schubert, W. Liu, X. Li, and J. A. Smart, "Recombination dynamics in ultraviolet light-emitting diodes with Si-doped AlGaN/AlGaN multiple quantum well active regions," *Jpn. J. Appl. Phys.*, vol. 101, pp. 113 102–1–5, 2007.

[76] S. Sawyer, S. Rumyantsev, and M. Shur, "Degradation of AlGaN-based ultraviolet light emitting diodes," *Sol.-State Electr.*, vol. 52, no. 6, pp. 968–972, 2008.

[77] J. P. Zhang, X. Hu, Y. Bilenko, J. Deng, A. Lunev, M. S. Shur, R. Gaska, M. Shatalov, J. W. Yang, and M. A. Khan, "Algan-based 280 nm light-emitting diodes with continuous-wave power exceeding 1 mw at 25 ma," *Appl. Phys. Lett.*, vol. 85, no. 23, pp. 5532–5534, 2004.

[78] X. Cao and S. LeBoeuf, "Current and temperature dependent characteristics of deep-ultraviolet light-emitting diodes," *Electron Devices, IEEE Transactions on*, vol. 54, no. 12, pp. 3414–3417, Dec. 2007.

[79] C. R. Moon, B. D. Choe, S. D. Kwon, H. K. Shin, and H. J. Lim, "Electron distribution and capacitance-voltage characteristics of n-doped quantum wells," *J. Appl. Phys.*, vol. 84, no. 5, pp. 2673–2683, 1998.

[80] C. R. Moon and H. J. Lim, "Influence of quantum well structural parameters on capacitance-voltage characteristics," *Appl. Phys. Lett.*, vol. 74, no. 20, pp. 2987–2989, 1999.

[81] A. Y. Polyakow, N. B. Smirnov, A. V. Govorkov, J. Kim, B. Luo, R. Mehandru, F. Ren, K. P. Lee, S. J. Pearton, A. V. Osinsky, and P. E. Norris, "Enhanced tunneling in GaN/InGaN multi-quantum well heterojunction diodes after short-term injection annealing," *J. of Appl. Phys.*, vol. 91, no. 8, pp. 5203–5207, 2002.

[82] E. Elsayed, *Handbook of Reliability Engineering*. Springer, 2003, ch. 22, pp. 415–428.